Dynamic analysis of a bridge structure exposed to high-speed railway traffic

Master thesis

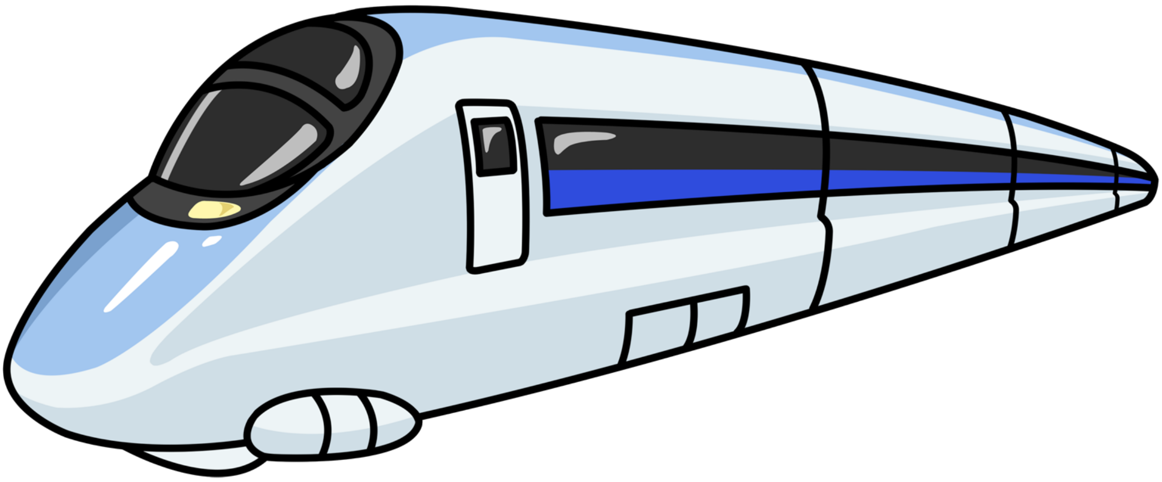

Master of Science in Structural and Civil Engineering

Paulius Bucinskas

Liuba Agapii

Jonas Sneideris

Aalborg University

School of Civil Engineering and Science

2015

School of Engineering and Science
Fredrik Bajers Vej 5, P. O. Box 159
DK–9100 Aalborg, Denmark
Tel.: (45)99409940
E-mail:aau@aau.dk
http://www.ses.aau.dk

Title: Dynamic analysis of a bridge structure exposed to high-speed railway traffic

Theme: Master thesis

Project period: September 1st, 2014 - June 5th, 2015

Project group: BK 10

Participants:

Paulius Bucinskas

Liuba Agapii

Jonas Sneideris

Supervisor: Lars Vabbersgaard Andersen

Existing copies: 5
Pages: 79
Appendices: 80 pages
Attached: 1 USB flash drive

Abstract:

Dynamic behaviour of railway bridges became a topic of great importance due to development of high-speed railways in various countries. With increasing speeds the dynamic loads increase drastically and become harder to predict, thus more complex computational models are needed to proper evaluate the behaviour of the structure. Firstly, a simply supported beam subjected to a moving constant force is analysed, using analytical and finite element methods. Later a vehicle is implemented in the model in different ways: as a moving mass, single-degree-of-freedom system and multi-degree-of-freedom system. Next step is taken by introducing three-dimensional model, created using three-dimensional beam elements. The most advanced computational model, which includes the subsoil and a vehicle models, is described in the paper "Numerical modelling of dynamic response of high-speed railway bridges considering vehicle–structure and structure–soil–structure interaction". The tests performed to validate the computational models on a small-scale experimental model are presented in the paper "Experimental validation of a numerical model for three-dimensional railway bridge analysis by comparison with a small–scale model". The experimental tests show that a proper modelling of the vehicle–track system and implementation of subsoil are crucial for analysis of the structural dynamic behaviour. The proposed computational model, offers a simplified solution for preliminary calculations, but accounts for the most significant contributions to vibrations and deformations of the bridge–subsoil system.

Prologue

This document includes master thesis, titled “Dynamic analysis of a bridge structure exposed to high-speed railway traffic” written by Paulius Bucinskas, Liuba Agapii and Jonas Sneideris. The complete work is split into three parts. First of all, the knowledge base and the theory behind are presented in the report “Dynamic analysis of a bridge structure exposed to high-speed railway traffic”. The most advanced computational model, created to investigate dynamic behaviour of the structure including the subsoil and the vehicle, is described in the paper “Numerical modelling of dynamic response of high-speed railway bridges considering vehicle–structure and structure–soil–structure interaction” presented in the Appendix A. To validate the computational model, experimental tests on a small–scale model are performed and presented in the paper “Experimental validation of a numerical model for three-dimensional railway bridge analysis by comparison with a small–scale model” given in Appendix B. Additionally, Appendix C, “Numerical code”, describing the code used for the computational model, and Appendix D, “Experimental testing of a small–scale bridge model”, where more detailed explanation of the testing procedure and the construction solutions of the model are presented, are given.

The authors would like to show gratitude to Lars Vabbersgaard Andersen for guidance and assistance during the course of the project.

Summary

In this document dynamic response of a multi-span railway bridge exposed to a high-speed railway traffic is investigated.

Firstly, the most simple case of a simply supported two-dimensional beam traversed by a constant force is analysed. This is modelled by using both an analytical approach and the finite element method. The basic model provides a steppingstone for further more advanced models involving different phenomena. The finite element method is used for all further calculations of the structure. Further, a vehicle is implemented in a number of different ways: as a moving mass, as a single-degree-of-freedom system and as a multi-degree-of-freedom system. Each of these different models predicts the effects from the moving vehicle with different precision. Finally, a multi-degree-of-freedom vehicle is chosen for further analysis, based on the comparison of the results.

The next step is modelling the system in three-dimensions. For it, two-noded beam elements with six degrees-of-freedom at each node, are introduced and described, as well as the transformation between local and global coordinate systems. These simple three-dimensional models are then improved by introducing multi-layered deck structure, vehicle and underlying soil body. To properly evaluate the effects from the vehicle caused by vertical track irregularities, a non-linear wheel–rail interaction force is introduced. The soil body is modelled utilizing a semi-analytical approach, based on Green's function solution in frequency wave-number domain. The obtained soil impedance matrix is then added to the structure at connecting nodes. Since non-linear vehicle solution is obtained in time domain and bridge–soil structure is solved in frequency domain, an iteration procedure is introduced to solve both parts simultaneously. The presented results show the effects, from different soil parameters and different vehicle modelling approaches, on the dynamic structure behaviour.

Further, the developed computational model is validated using small–scale experimental tests. Experimental multi-span bridge model, with surface footings is constructed. The underlying soil is substituted by layers of mattress foam. Bridge structure is excited by a travelling electric vehicle, with four wheel sets, on a plastic railway track. A number of accelerometers are placed in strategic positions, to analyse the structure response. Frequency response functions of the small–scale structure are compared to those from the computational model, as well as accelerations in frequency domain. The obtained results show a reasonable agreement between the two models.

Contents

Chapter 1

Introduction

The interest in dynamic behaviour of railway bridges has increased in recent years due to development of high-speed railways in various countries. An example of this is the long-term plan for transportation in Denmark, part of which is the so-called “1 Hour Model”. The aim is to decrease the travel time between the four major cities of Denmark to one hour, thereby decreasing the total travel time between Copenhagen and Aalborg from approximately four and a half hours to three hours. The new high-speed line, which will be able to handle train traffic speeds up to 250km/h, between Copenhagen and Ringsted is already under construction and is expected to open in 2018. After realization of Copenhagen–Odense–Aarhus–Aalborg connections, further expand of the high-speed railway network to Esbjerg is considered. The concept plan for the 1 Hour Model is illustrated in Figure 1.1.

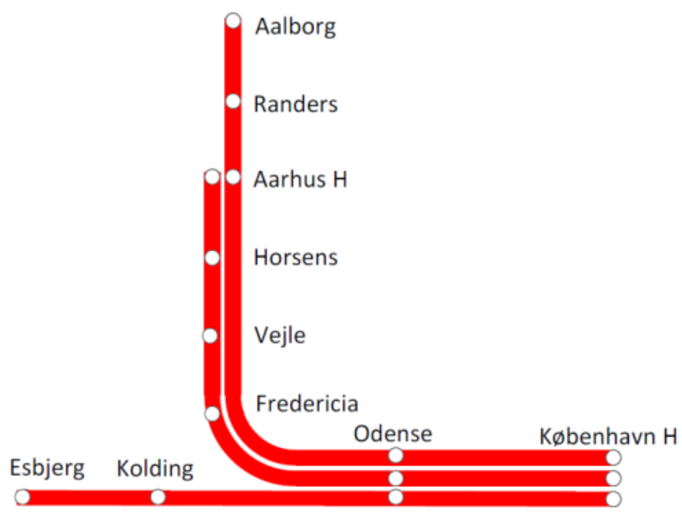

Figure 1.1: Concept 1 Hour Model plan of high-speed railway connections between the major cities in Denmark, [1]

Realization of the project includes construction of several new high-speed railway lines, upgrade of the existing lines, construction of a new bridge across the Fjord of Vejle and electrification of the intercity railway network.

High-speed rail is emerging in Europe as an increasingly popular and efficient means of transport. The first lines were built in the 1980s and 1990s which reduced the travel time on intranational corridors. During the years several countries, like France, Spain, Italy, Germany, Austria, Sweden, Belgium, the Netherlands, Russia and the United Kingdom have built an extensive high-speed railway networks and established cross-border connections. More European countries are expected to be connected to the high-speed railway network in the incoming years since Europe invests heavily in the infrastructure across the continent. One of the largest contract designer and manufacturer of high-speed trains in Europe is TGV, France. A high-speed railway line raised on pylons in France with a traversing TGV high-speed train is shown in Figure 1.2.

Figure 1.2: High-speed railway line in France with a passing TGV high-speed train, [2]

The railway lines are complex structures where a lot of different phenomena have to be taken into account during the design process. It becomes even more complicated when the lines are built on the bridge structure and are exposed to high-speed train traffic, which is the case considered in the thesis. More particularly, the dynamic structural behaviour is investigated for a high-speed railway bridge exposed to traffic speeds up to 250km/h. For high speeds various factors such as a vehicle traversing the bridge, track irregularities or underlying soil properties might become crucial, thus it is important to investigate the effects caused by the mentioned factors.

The most simple approach to model the traversing vehicle is to apply moving constant forces on the bridge structure. However, such rough way of modelling vehicle might not be able to recreate the dynamics of suspensions used in present days trains and therefore the response of the structure might be underestimated. In Figure 1.3 an example of a high-speed train suspension is shown.

Figure 1.3: Suspension of a high-speed train, [3]

Another important factor to investigate for the high-speed railway might be the irregularities of the track or wheel flats, since they might cause significant excitation of the structure, especially with increasing speeds. Also the mentioned track or wheel defects can affect the comfort (vibrations felt in the train carriage during the travel) or even the safety (possibility for the train do derail). An extreme example of track irregularities is shown in Figure 1.4.

Figure 1.4: Railway track irregularities, [4]

To model a bridge structure, pylons fixed to a rigid surface, might be an inadequate approach, except the case when it is build straight on bedrock. However, usually it is not the case and therefore the effects from the subsoil on the dynamic structural behaviour should be analysed, especially when the subsoil is soft. In Figure 1.5 an example of a railway bridge built on soft subsoil is shown.

Figure 1.5: Railway bridge built on soft soil, [5]

The dynamic loads increase significantly with increasing train speeds and become hard to predict. Thus, more complex numerical models are required for proper evaluation of the structural behaviour. One aim of the thesis is to create a computational model which encompasses a bridge structure, a passing vehicle model, the effects from track irregularities and the subsoil. Another aim of the thesis is validation of the created computational model which is done by performing tests a small–scale experimental model.

Chapter 2
Simply supported beam with moving force

In this chapter, an analytical solution for a simply supported two-dimensional (2-D) beam traversed by a constant moving force is given in Section 2.1 and the finite element formulation (FEM) of the same problem is given in Section 2.2. In the last mentioned section, the formulation of a finite 2-D beam element is introduced. Further, solution techniques are presented introducing full equation of motion in Subsection 2.2.1, damping in Subsection 2.2.2, time domain solution and time integrations in Subsection 2.2.3, frequency-domain solution in Subsection 2.2.4 and modal analysis in Subsection 2.2.5. Lastly, in Section 2.3 a comparison between deflections of the models described theoretically in previous sections is presented.

2.1 Analytical solution in two dimensions

The present section is based on Fryba [6]. A classical solution for problems involving vibrations of structures subjected to a moving load is applied, in order to determine a bridge response to a passing train analytically. Therefore, the railway bridge exposed to a passing train is defined as a simply supported beam, traversed by a constant force moving at uniform speed.

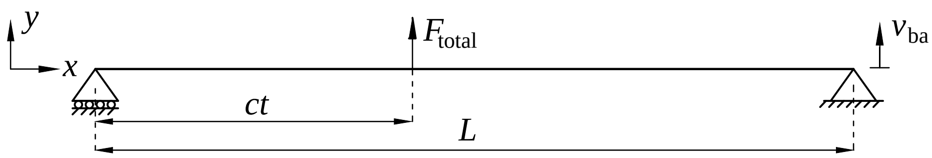

Figure 2.1: Simply supported beam subjected to a moving force F_{total}

The analytical solution is based on following assumptions:

- The beam is considered as a Bernoulli-Euler beam which is described by partial differential Equation 2.1;
- The beam has a constant cross-section and constant mass per unit length;
- The mass of the beam is much bigger than the mass of the moving load which means that only gravitational effects of the load are considered. Thus, the load is expressed by $F_{\text{total}} = -M_{\text{total}} \cdot g$, where M_{total} is a mass of the train and g is the gravitational acceleration;
- The load moves from left to the right with a constant speed;

- Damping is proportional to the velocity of vibration (viscous damping);
- At both ends of the beam deflections and bending moments are equal to zero (defined by boundary conditions, Equation 2.2);
- At the instant of force arrival $t = 0$, the beam is at rest which means that deflection and velocity are equal to zero (defined by initial conditions, Equation 2.3);
- It is a 2-D problem.

The partial differential equation of motion is as follows:

$$E_\mathrm{b} I_{\mathrm{b},z} \frac{\partial v_\mathrm{ba}^4(x,t)}{\partial x^4} + \rho_\mathrm{b} A_\mathrm{b} \frac{\partial v_\mathrm{ba}^2(x,t)}{\partial t^2} + 2\rho_\mathrm{b} A_\mathrm{b} \omega_\mathrm{b} \frac{\partial v_\mathrm{ba}(x,t)}{\partial t} = \delta(x-ct) F_\mathrm{total}, \tag{2.1}$$

where

x	length coordinate with the origin at the left-hand end of the beam,
t	time coordinate with the origin at the instant of the force arriving upon the beam,
$v_\mathrm{ba}(x,t)$	beam deflection at point x and time t, measured from equilibrium position when the beam is loaded by self-weight,
E_b	Young's modulus of the beam,
$I_{\mathrm{b},z}$	moment of inertia of the beam, constant through the length of the beam,
ρ_b	mass density,
A_b	cross-sectional area ,
ω_b	circular frequency of damping of the beam,
F_total	concentrated force of constant magnitude,
c	constant speed of the moving load,
$\delta(x-ct)$	the Dirac delta function, shifted to the right side from origin by ct.

The Dirac delta function can be defined as

$$\delta(x) = \begin{cases} +\infty, & x = 0, \\ 0, & x \neq 0. \end{cases}$$

Beam physical properties such as stiffness, mass and damping are represented by first, second and third terms, respectively, on the left-hand side of differential Equation 2.1. Right-hand side defines an external force acting on the beam. The boundary conditions are:

$$v_\mathrm{ba}(0,t) = 0, \qquad v_\mathrm{ba}(L,t) = 0,$$

$$\left.\frac{\partial^2 v_\mathrm{ba}(x,t)}{\partial x^2}\right|_{x=0} = 0, \qquad \left.\frac{\partial^2 v_\mathrm{ba}(x,t)}{\partial x^2}\right|_{x=L} = 0, \tag{2.2}$$

where L is the beam length. The initial conditions are:

$$v_\mathrm{ba}(x,0) = 0, \qquad \left.\frac{\partial v_\mathrm{ba}(x,t)}{\partial t}\right|_{t=0} = 0, \quad x \in [0; L]. \tag{2.3}$$

Deflection of the beam is determined using:

$$v_{\mathrm{ba}}(x,t) = v_{\mathrm{ba},0}\sum_{j=1}^{\infty}\frac{1}{j^2[j^2(j^2-\alpha^2)^2+4\alpha^2\beta^2]}\Bigg[j^2(j^2-\alpha^2)\sin(j\omega t)$$
$$-\frac{j\alpha[j^2(j^2-\alpha^2)-2\beta^2]}{(j^4-\beta^2)^{1/2}}e^{-\omega_{\mathrm{b}}t}\sin(\omega'_{(j)}t-2j\alpha\beta)(cos(j\omega t)-e^{-\omega_{\mathrm{b}}t}cos(\omega'_{(j)}t)\Bigg]\sin(\frac{j\pi x}{l}), \tag{2.4}$$

which includes j modes of vibration. The effects of speed and damping are involved in the solution. Also $t \leq T_{\mathrm{v}}$ which means that solution is valid as long as force acts on the beam, T_{v} is the time needed for the vehicle to cross the bridge. The deflection denoted as $v_{\mathrm{ba},0}$ is the static deflection in the middle of the same beam from a force F_{total}:

$$v_{\mathrm{ba},0} = \frac{F_{\mathrm{total}}L^3}{48E_{\mathrm{b}}I_{\mathrm{b},z}}.$$

Dimensionless parameters α and β denote the effects of speed and damping, respectively:

$$\alpha = \frac{cL}{\pi}\left(\frac{\rho_{\mathrm{b}}A_{\mathrm{b}}}{E_{\mathrm{b}}I_{\mathrm{b},z}}\right)^{1/2}, \tag{2.5}$$

$$\beta = \frac{\omega_{\mathrm{b}}}{\omega_{(1)}}. \tag{2.6}$$

The circular frequency of damping of the beam ω_{b}:

$$\omega_{\mathrm{b}} = \xi_{\mathrm{b}}f_{(1)}, \tag{2.7}$$

where ξ_{b} is the logarithmic decrement of damping of the beam, expressed as:

$$\xi_{\mathrm{b}} = \frac{2\pi\zeta_{\mathrm{b}}}{\sqrt{1-\zeta_{\mathrm{b}}^2}}, \tag{2.8}$$

parameter ζ_{b} is the damping ratio. The circular frequency $\omega_{(j)}$ and the corresponding natural frequency $f_{(j)}$ of the j mode of vibration of a simply supported beam are defined by:

$$\omega_{(j)} = \sqrt{\frac{j^4\pi^4E_{\mathrm{b}}I_{\mathrm{b},z}}{L^4\rho_{\mathrm{b}}A_{\mathrm{b}}}}, \tag{2.9}$$

$$f_{(j)} = \frac{\omega_{(j)}}{2\pi}. \tag{2.10}$$

The circular frequency ω is expressed as:

$$\omega = \frac{\pi c}{L}, \tag{2.11}$$

while the circular frequency of a damped beam $\omega'_{(j)}$ with light damping ($\zeta_{\mathrm{b}} \ll 1$) is equal to

$$\omega'_{(j)} = \sqrt{\omega^2_{(j)} - \omega^2_{\mathrm{b}}}. \tag{2.12}$$

Using the methodology presented in this section, the structural response to a moving load is determined analytically. Deflection of the bridge can be found at any length coordinate x for a vehicle traverse time T_{v} defined in a preferable accuracy using proper time step t. Obtained results depend on many parameters such as train speed, bridge length and cross-section, damping ratio and etc. Therefore, parameters sensitivity analysis is performed regarding the different parameters and results are presented in Subsection 2.3.2.

2.2 Finite element method in two dimensions

The finite element method is one of the most popular and convenient techniques for numerical solution for field problems. Mathematically, the field problem is described by differential equations or integral expressions. Either description may be used to formulate finite elements which can be visualized as small pieces of a structure. The elements are connected at the nodes. Therefore, a ”*net*”, i.e. a particular arrangement of all elements used to describe a finite structure, is called a mesh. Since each finite element is described by algebraic equations, the whole field will be represented as a system of those equations. Latter equations are used to find unknowns at the nodes or at any point between nodes invoking interpolation. Using obtained quantities, a spatial variation of unknowns within the element can be determined. Since the whole structure is approximated element by element, a final solution for a field is obtained at the end, cf. e.g Cook [7].

Firstly, a railway bridge is modelled as a simply supported beam, as in Section 2.1, where analytical solution for a structure is introduced. However, for a numerical solution, bridge is discretized into a number of 2-D beam elements. Thus, a brief FEM formulation for mentioned elements is introduced in present section.

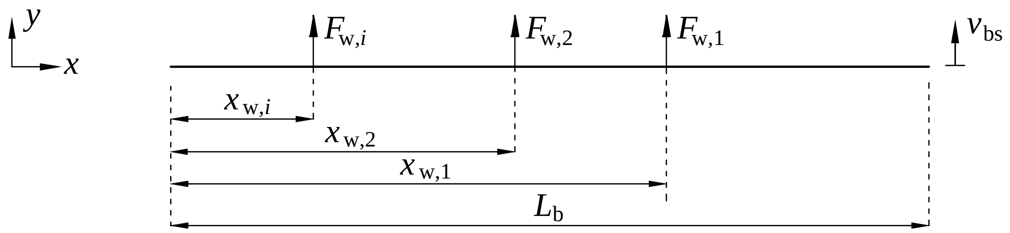

Figure 2.2: Beam with multiple concentrated forces travelling across it

A single 2-D beam element is considered, where the longitudinal axis is parallel with the x-axis direction, a shown in Figure 2.2. It is assumed that it has a constant cross-section and constant mass per unit length. The element has a node at each end and two degrees of freedom (dof) at each node, lateral deflections $v_{\mathrm{bs},1}$, $v_{\mathrm{bs},2}$ and rotations $\psi_{\mathrm{bs},1}$, $\psi_{\mathrm{bs},2}$.

The 2-D beam element is described using Euler-Bernoulli beam theory, i.e. assuming absence of transverse shear deformations and only including the effects of bending. Thus, the equation of motion, i.e. the strong form of a governing partial differential equation, for a beam is expressed by:

$$E_{\mathrm{b}} I_{\mathrm{b},z} \frac{\partial^4 v_{\mathrm{bs}}(x,t)}{\partial x^4} + \rho_{\mathrm{b}} A_{\mathrm{b}} \frac{\partial^2 v_{\mathrm{bs}}(x,t)}{\partial t^2} = \sum_{i=1}^{N_{\mathrm{w}}} \delta(x - x_{\mathrm{w},i}(t)) F_{\mathrm{w},i} \quad + \quad \text{boundary conditions}, \tag{2.13}$$

where the beam is described by: Young's modulus E_{b}, moment of inertia of the beam cross-sectional area around the z-axis $I_{\mathrm{b},z}$, mass density ρ_{b}, cross-sectional area A_{b}, transverse deflection of the beam $v_{\mathrm{bs}}(x,t)$ and a number N_{w} of concentrated forces $F_{\mathrm{w},i}$ applied at distances $x_{\mathrm{w},i}$ to the right from the 1st node. The length of the beam element is L_{b}. Boundary conditions can be either nodal forces or forced nodal displacements.

Equation 2.13 is transformed into a so-called weak form using standard Galerkin approach. The following steps are applied:

- discretization and interpolation of displacement field, $v_{\mathrm{bs}}(x,t)$;
- premultiplication of a strong form by weight functions;
- integration by parts over the element length.

After application of these steps the weak form is obtained:

$$\begin{aligned} &\int_0^{L_{\mathrm{b}}} \delta v_{\mathrm{bs}}(x,t) \rho_{\mathrm{b}} A_{\mathrm{b}} \frac{\partial^2 v_{\mathrm{bs}}(x,t)}{\partial t^2} \mathrm{d}x + \int_0^{L_{\mathrm{b}}} \frac{\partial^2 \delta v_{\mathrm{bs}}(x,t)}{\partial x^2} E_{\mathrm{b}} I_{\mathrm{b},z} \frac{\partial^2 v_{\mathrm{bs}}(x,t)}{\partial x^2} \mathrm{d}x \\ &= \sum_{i=1}^{N_{\mathrm{w}}} \int_0^{L_{\mathrm{b}}} \delta v_{\mathrm{bs}}(x,t) \delta(x - x_{\mathrm{w},i}(t)) F_{\mathrm{w},i} \mathrm{d}x - \Big[\delta v_{\mathrm{bs}}(x,t) Q_{\mathrm{bs},y}(x,t) \Big]_0^{L_{\mathrm{b}}} + \Big[\frac{\partial \delta v_{\mathrm{bs}}(x,t)}{\partial x} M_{\mathrm{bs},z}(x,t) \Big]_0^{L_{\mathrm{b}}}, \end{aligned} \tag{2.14}$$

where first member on the left-hand side is mass of the beam and the second one is bending stiffness. The right-hand side of Equation 2.14 gives external forces.

In order to discretize displacements field and to obtain these quantities at any spatial coordinate x at an instant time t, an interpolation between two element nodes has to be included. Interpolation is handled by using weight and shape functions. Therefore, physical displacement at coordinate x and time t can be written by following expression

$$v_{\mathrm{bs}}(x,t) = \{\check{\Phi}(x)\}\{\mathbf{d}_{\mathrm{BS}}(t)\}, \tag{2.15}$$

where $\{\mathbf{d}_{\mathrm{BS}}(t)\}$ denotes the discretized displacement at each dof of the element, see Equation 2.19, and $\{\check{\Phi}(x)\}$ is a shape function vector, defined by Equation 2.18. Moreover, virtual field (or variation field) can be expressed by:

$$\delta v_{\mathrm{bs}}(x,t) = \{\delta\, \mathbf{d}_{\mathrm{BS}}(t)\}^T \{\check{\Psi}(x)\}^T, \tag{2.16}$$

where $\{\delta \mathbf{d}_{\mathrm{BS}}(t)\}$ are arbitrary nodal values of the virtual field and $\{\check{\Psi}(x)\}$ are the weight functions. The Galerkin approach implies that the shape functions are identical to the weight functions

$$\{\check{\Phi}(x)\} = \{\check{\Psi}(x)\}, \tag{2.17}$$

and therefore, the physical and virtual displacement fields can be described using the same shape functions for a beam element. Four shape functions are obtained regarding each degree of freedom. Those are expressed by the following vector:

$$\{\check{\Phi}(x)\}^T = \begin{Bmatrix} 1 - \frac{3x^2}{L_{\mathrm{b}}^2} + \frac{2x^3}{L_{\mathrm{b}}^3} \\ x - \frac{2x^2}{L_{\mathrm{b}}} + \frac{x^3}{L_{\mathrm{b}}^2} \\ \frac{3x^2}{L_{\mathrm{b}}^2} - \frac{2x^3}{L_{\mathrm{b}}^3} \\ -\frac{x^2}{L_{\mathrm{b}}} + \frac{x^3}{L_{\mathrm{b}}^2} \end{Bmatrix} . \tag{2.18}$$

The nodal displacements of a 2-D beam element are defined by the following vector:

$$\{\mathbf{d}_{\mathrm{BS}}(t)\} = \begin{Bmatrix} v_{\mathrm{bs},1}(t) \\ \psi_{\mathrm{bs},1}(t) \\ v_{\mathrm{bs},2}(t) \\ \psi_{\mathrm{bs},2}(t) \end{Bmatrix} \begin{matrix} \text{transverse displacement at the first node;} \\ \text{rotation at the first node;} \\ \text{transverse displacement at the second node;} \\ \text{rotation at the second node.} \end{matrix} \tag{2.19}$$

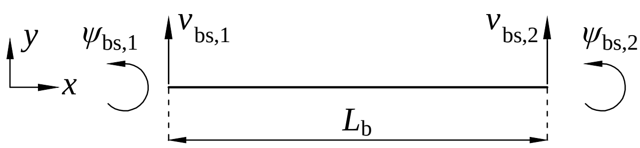

Figure 2.3: Nodal degrees of freedom for a 2-D beam element

Finally, by inserting Equation 2.15 and Equation 2.16 into Equation 2.14 the weak form becomes able to describe the time series of displacements. Thus, a solution for the finite beam element as well as for a numerical model which includes whole bridge structure affected by passing train can be obtained. The finite element form of the equation of motion for a beam element can be written as:

$$[\mathbf{M}_{\mathrm{BS}}]\{\ddot{\mathbf{d}}_{\mathrm{BS}}(t)\}+[\mathbf{K}_{\mathrm{BS}}]\{\mathbf{d}_{\mathrm{BS}}(t)\}=\{\mathbf{f}_{\mathrm{BS}}(t)\}, \tag{2.20}$$

where $\{\ddot{\mathbf{d}}_{\mathrm{BS}}(t)\}=\mathrm{d}^2\{\mathbf{d}_{\mathrm{BS}}(t)\}/\mathrm{d}t^2$ is acceleration, and $[\mathbf{M}_{\mathrm{BS}}]$ denotes the consistent element mass matrix:

$$[\mathbf{M}_{\mathrm{BS}}]=\int_0^{L_\mathrm{b}}\{\check{\Phi}(x)\}^T\rho_\mathrm{b}A_\mathrm{b}\{\check{\Phi}(x)\}\mathrm{d}x=\frac{\rho_\mathrm{b}A_\mathrm{b}L_\mathrm{b}}{420}\begin{bmatrix}156 & 22L_\mathrm{b} & 54 & -13L_\mathrm{b}\\ & 4L_\mathrm{b}^2 & 13L_\mathrm{b} & -3L_\mathrm{b}^2\\ \mathit{Symm} & & 156 & -22L_\mathrm{b}\\ & & & 4L_\mathrm{b}^2\end{bmatrix}. \tag{2.21}$$

$[\mathbf{K}_{\mathrm{BS}}]$, the element stiffness matrix, is described as:

$$[\mathbf{K}_{\mathrm{BS}}]=\int_0^{L_\mathrm{b}}\frac{\mathrm{d}^2\{\check{\Phi}(x)\}^T}{\mathrm{d}x^2}E_\mathrm{b}I_{\mathrm{b},z}\frac{\mathrm{d}^2\{\check{\Phi}(x)\}}{\mathrm{d}x^2}\mathrm{d}x=\begin{bmatrix}\frac{12E_\mathrm{b}I_{\mathrm{b},z}}{L_\mathrm{b}^3} & \frac{6E_\mathrm{b}I_{\mathrm{b},z}}{L_\mathrm{b}^2} & -\frac{12E_\mathrm{b}I_{\mathrm{b},z}}{L_\mathrm{b}^3} & \frac{6E_\mathrm{b}I_{\mathrm{b},z}}{L_\mathrm{b}^2}\\ & \frac{4E_\mathrm{b}I_{\mathrm{b},z}}{L_\mathrm{b}} & -\frac{6E_\mathrm{b}I_{\mathrm{b},z}}{L_\mathrm{b}^2} & \frac{2E_\mathrm{b}I_{\mathrm{b},z}}{L_\mathrm{b}}\\ \mathit{Symm} & & \frac{12E_\mathrm{b}I_{\mathrm{b},z}}{L_\mathrm{b}^3} & -\frac{6E_\mathrm{b}I_{\mathrm{b},z}}{L_\mathrm{b}^2}\\ & & & \frac{4E_\mathrm{b}I_{\mathrm{b},z}}{L_\mathrm{b}}\end{bmatrix}. \tag{2.22}$$

The load vector is $\{\mathbf{f}_{\mathrm{BS}}(t)\}=\{\mathbf{f}_{\mathrm{BS,b}}(t)\}+\{\mathbf{f}_{\mathrm{BS,c}}(t)\}$, where $\{\mathbf{f}_{\mathrm{BS,b}}(t)\}$ is the boundary load vector, while $\{\mathbf{f}_{\mathrm{BS,c}}(t)\}$ is the consistent nodal loads:

$$\{\mathbf{f}_{\mathrm{BS,b}}(t)\}=-\Big[\{\check{\Phi}(x)\}^T Q_{\mathrm{bs},y}(x,t)\Big]_0^{L_\mathrm{b}}+\left[\frac{\mathrm{d}\{\check{\Phi}(x)\}^T}{\mathrm{d}x}M_{\mathrm{bs},z}(x,t)\right]_0^{L_\mathrm{b}}, \tag{2.23}$$

$$\{\mathbf{f}_{\mathrm{BS,c}}(t)\}=\sum_{i=1}^{N_\mathrm{w}}\int_0^{L_\mathrm{b}}\{\check{\Phi}(x)\}^T\delta(x-x_{\mathrm{w},i}(t))F_{\mathrm{w},i}\mathrm{d}x=\sum_{i=1}^{N_\mathrm{w}}\{\check{\Phi}(x_{\mathrm{w},i})\}^T F_{\mathrm{w},i}. \tag{2.24}$$

Another approach to distribute mass over the beam element is to use a lumped mass matrix:

$$[\mathbf{M}_{\mathrm{BS,l}}]=\rho_\mathrm{b}A_\mathrm{b}L_\mathrm{b}\begin{bmatrix}\frac{1}{2} & 0 & 0 & 0\\ & \frac{1}{24}L_\mathrm{b}^2 & 0 & 0\\ \mathit{Symm} & & \frac{1}{2} & 0\\ & & & \frac{1}{24}L_\mathrm{b}^2\end{bmatrix}. \tag{2.25}$$

The nodal load vector $\{\mathbf{f}_{\mathrm{BS}}(t)\}$ associated with nodal degrees of freedom $v_{\mathrm{bs},1}$, $v_{\mathrm{bs},2}$ and $\psi_{\mathrm{bs},1}$,

$\psi_{\mathrm{bs},2}$ is as follows:

$$\{\mathbf{f}_{\mathrm{BS}}(t)\} = \begin{Bmatrix} q_{\mathrm{bs},1}(t) \\ m_{\mathrm{bs},1}(t) \\ q_{\mathrm{bs},2}(t) \\ m_{\mathrm{bs},2}(t) \end{Bmatrix} .$$

The nodal loads are illustrated in Figure 2.4.

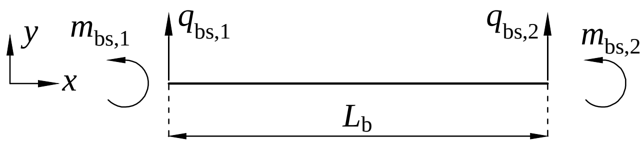

Figure 2.4: Beam element with four degrees of freedom

2.2.1 Full equation of motion

The full structure is defined by a number of finite elements as it was mentioned at the introduction of the present chapter. In Section 2.2, the 2-D beam element stiffness matrix $[\mathbf{K}_{\mathrm{BS}}]$, consistent mass matrix $[\mathbf{M}_{\mathrm{BS}}]$ and load vector $\{\mathbf{f}_{\mathrm{BS}}(t)\}$ have been defined. To create a numerical model for a full structure, the element matrices have to be assembled into a global system of equations. Thus, a global stiffness matrix $[\mathbf{K}]$, global mass matrix $[\mathbf{M}]$ and load vector $\{\mathbf{f}(t)\}$ are obtained. These system matrices and vectors describe the whole structure. Therefore, the full system can be described by the following expression:

$$[\mathbf{M}]\{\ddot{\mathbf{d}}(t)\} + [\mathbf{K}]\{\mathbf{d}(t)\} = \{\mathbf{f}(t)\}, \tag{2.26}$$

where $\{\ddot{\mathbf{d}}(t)\}$ and $\{\mathbf{d}(t)\}$ are the discretized full systems accelerations and displacements, respectively. Assuming that there is a number N_{dof} degrees of freedom, the system matrices $[\mathbf{M}]$, $[\mathbf{K}]$ have the dimensions $N_{\mathrm{dof}} \times N_{\mathrm{dof}}$, while the vectors $\{\ddot{\mathbf{d}}(t)\}$, $\{\mathbf{d}(t)\}$ and $\{\mathbf{f}(t)\}$ have the dimensions $N_{\mathrm{dof}} \times 1$.

Seeking to obtain more accurate and realistic response of the structure, viscous damping is introduced in the numerical model. The full equation of motion in the finite element formulation is then defined

$$\begin{aligned} &[\mathbf{M}]\{\ddot{\mathbf{d}}(t)\} + [\mathbf{C}]\{\dot{\mathbf{d}}(t)\} + [\mathbf{K}]\{\mathbf{d}(t)\} = \{\mathbf{f}(t)\}, \\ &\quad \{\mathbf{d}(0)\} = \{\mathbf{d}_0\} \quad \{\dot{\mathbf{d}}(0)\} = \{\dot{\mathbf{d}}_0\}, \end{aligned} \tag{2.27}$$

where $\{\mathbf{d}_0\}$ and $\{\dot{\mathbf{d}}(0)\}$ are initial conditions for displacement and velocity, respectively. $[\mathbf{C}]$ is the global damping matrix, which shows dependence on velocity $\{\dot{\mathbf{d}}(t)\}$.

2.2.2 Rayleigh damping

Rayleigh damping is introduced in terms of damping matrix which is a linear combination of the mass and stiffness matrices

$$[\mathbf{C}] = \alpha_{\mathrm{R}}[\mathbf{M}] + \beta_{\mathrm{R}}[\mathbf{K}], \tag{2.28}$$

where α_{R} and β_{R} represent Rayleigh damping coefficients. They can be approximated if damping ratios $\zeta_{(1)}$ and $\zeta_{(2)}$ for any two eigenmodes of the structure are known:

$$\alpha_{\mathrm{R}} = 2\omega_{(1)}\omega_{(2)}\frac{\left(\zeta_{(1)}\omega_{(2)} - \zeta_{(2)}\omega_{(1)}\right)}{\omega_{(2)}^2 - \omega_{(1)}^2}, \tag{2.29}$$

$$\beta_{\mathrm{R}} = 2\frac{\left(\zeta_{(2)}\omega_{(2)} - \zeta_{(1)}\omega_{(1)}\right)}{\omega_{(2)}^2 - \omega_{(1)}^2}, \tag{2.30}$$

where $\omega_{(1)}$ and $\omega_{(2)}$ are the two modes circular eigenfrequencies. Lower modes are mostly damped by a member $\alpha_{\mathrm{R}}[\mathbf{M}]$, while higher modes are more influenced by $\beta_{\mathrm{R}}[\mathbf{K}]$, cf. Cook [7].

2.2.3 Time domain solution and time integrations

Time domain solution is based on time discretization, introducing a time step Δt. General displacements, i.e. lateral displacements and rotations for a beam element, velocities and external forces which are discretized in space by using Equation 2.27 are further decomposed in time. This procedure can be done using explicit or implicit integration schemes. For explicit schemes only values of displacements, velocities and external loads at time step t^j are required, for the computation of the similar of these quantities at the next time step t^{j+1}. In implicit schemes, displacements, velocities and external loads at time t^{j+1} are dependent upon each other, which requires solution of system of equations. Furthermore, time integrations can be direct or indirect. Direct time integration is used when equation of motion Equation 2.27 is solved in its original form, while indirect integration requires transformation of Equation 2.27 into its state-space equivalent, as described in Andersen [8]. Using indirect time integration, original ordinary second-order differential equations are transformed into first-order differential equations. Firstly, the state vector is defined as $\{\mathbf{D}_{\mathrm{int}}(t)\} = \{d(t) \quad \dot{d}(t)\}^T$ and $\{\dot{\mathbf{D}}_{\mathrm{int}}(t)\} = \mathrm{d}\{\mathbf{D}_{\mathrm{int}}(t)\}/\mathrm{d}t$. Thus, Equation 2.27 for N_{dof} system is defined as:

$$\{\dot{\mathbf{D}}_{\mathrm{int}}(t)\} = [\mathbf{A}_{\mathrm{int}}]\{\mathbf{D}_{\mathrm{int}}(t)\} + \{\mathbf{F}_{\mathrm{int}}(t)\}, \tag{2.31}$$

where

$$[\mathbf{A}_{\mathrm{int}}] = \begin{bmatrix} [\mathbf{0}]_{N_{\mathrm{dof}}\times N_{\mathrm{dof}}} & [\mathbf{I}]_{N_{\mathrm{dof}}\times N_{\mathrm{dof}}} \\ -[\mathbf{M}]^{-1}[\mathbf{K}] & -[\mathbf{M}]^{-1}[\mathbf{C}] \end{bmatrix}, \tag{2.32}$$

$$\{\mathbf{F}_{\mathrm{int}}(t)\} = \begin{Bmatrix} \{\mathbf{0}\}_{N_{\mathrm{dof}}\times 1} \\ [\mathbf{M}]^{-1}\{\mathbf{f}(t)\} \end{Bmatrix}. \tag{2.33}$$

Runge-Kutta fourth-order time integration algorithm

One of the time integrations used in a numerical model of the bridge structure and a passing train is Runge-Kutta fourth-order algorithm. It calculates vectorial quantities for each time step t^j:

$$\{\mathbf{k}_{\mathrm{int},1}\} = \Delta t\{\dot{\mathbf{D}}_{\mathrm{int}}(t^j, D^j_{\mathrm{int}})\}, \tag{2.34a}$$
$$\{\mathbf{k}_{\mathrm{int},2}\} = \Delta t\{\dot{\mathbf{D}}_{\mathrm{int}}(t^j + 0.5\Delta t, D^j_{\mathrm{int}} + 0.5k_{\mathrm{int},1})\}, \tag{2.34b}$$
$$\{\mathbf{k}_{\mathrm{int},3}\} = \Delta t\{\dot{\mathbf{D}}_{\mathrm{int}}(t^j + 0.5\Delta t, D^j_{\mathrm{int}} + 0.5k_{\mathrm{int},2})\}, \tag{2.34c}$$
$$\{\mathbf{k}_{\mathrm{int},4}\} = \Delta t\{\dot{\mathbf{D}}_{\mathrm{int}}(t^{j+1}, D^j_{\mathrm{int}} + k_{\mathrm{int},3})\}, \tag{2.34d}$$

where $\{\mathbf{D}^j_{\mathrm{int}}\} = \{\mathbf{D}_{\mathrm{int}}(t^j)\}$. The generalized displacement vector $\{\mathbf{D}_{\mathrm{int}}(t^{j+1})\}$ for time step t^{j+1} can be found by:

$$\{\mathbf{D}_{\mathrm{int}}(t^{j+1})\} = \{\mathbf{D}_{\mathrm{int}}(t^j)\} + \frac{1}{6}\Big(\{\mathbf{k}_{\mathrm{int},1}\} + 2\{\mathbf{k}_{\mathrm{int},2}\} + 2\{\mathbf{k}_{\mathrm{int},3}\} + \{\mathbf{k}_{\mathrm{int},4}\}\Big). \tag{2.35}$$

This indirect, explicit time integration scheme provides accurate and reliable results until it works. The problem is that Runge-Kutta algorithm is just conditionally stable which means that it requires small time step to obtain stable solution. Moreover, system matrices conversion is highly demanding of array storage space. Due to these reasons a lot of computational power and time is required to obtain a solution.

Newmark second-order time integration algorithm

The other time integration used in the numerical model is Newmark second-order algorithm, which is direct, implicit time integration scheme. To obtain the displacements $\{\mathbf{d}^{j+1}_{\mathrm{BS}}\}$, velocities

$\{\dot{\mathbf{d}}_{\mathrm{BS}}^{j+1}\}$ and accelerations $\{\ddot{\mathbf{d}}_{\mathrm{BS}}^{j+1}\}$ at time step t^{j+1} the algorithm is:

$$\{\ddot{\mathbf{d}}_{\mathrm{BS}}^{j+1}\} = \{\ddot{\mathbf{d}}_{\mathrm{BS}}^{j}\} + [\hat{\mathbf{M}}]^{-1}(\{\mathbf{f}^{j+1}\} - [\mathbf{M}]\{\ddot{\mathbf{d}}_{\mathrm{BS}}^{j}\} - [\mathbf{C}]\{\dot{\mathbf{d}}_{\mathrm{BS},*}^{j+1}\} - [\mathbf{K}]\{\dot{\mathbf{d}}_{\mathrm{BS},*}^{j+1}\}), \tag{2.36a}$$

$$\{\dot{\mathbf{d}}_{\mathrm{BS}}^{j+1}\} = \{\dot{\mathbf{d}}_{\mathrm{BS},*}^{j+1}\} + \gamma(\{\ddot{\mathbf{d}}_{\mathrm{BS}}^{j+1}\} - \{\ddot{\mathbf{d}}_{\mathrm{BS}}^{j}\})\Delta t, \tag{2.36b}$$

$$\{\mathbf{d}_{\mathrm{BS}}^{j+1}\} = \{\mathbf{d}_{\mathrm{BS},*}^{j+1}\} + \beta(\{\ddot{\mathbf{d}}_{\mathrm{BS}}^{j+1}\} - \{\ddot{\mathbf{d}}_{\mathrm{BS}}^{j}\})\Delta t^2, \tag{2.36c}$$

where $[\hat{\mathbf{M}}] = [\mathbf{M}] + \gamma[\mathbf{C}]\Delta t + \beta[\mathbf{K}]\Delta t^2$, $\{\dot{\mathbf{d}}_{\mathrm{BS},*}^{j+1}\}$ is the predicted value of the velocity vector and $\{\mathbf{d}_{\mathrm{BS},*}^{j+1}\}$ is the predicted value of the displacement vector for time step $j+1$, expressed by

$$\{\dot{\mathbf{d}}_{\mathrm{BS},*}^{j+1}\} = \{\dot{\mathbf{d}}_{\mathrm{BS}}^{j}\} + \{\ddot{\mathbf{d}}_{\mathrm{BS}}^{j}\}\Delta t, \tag{2.37a}$$

$$\{\mathbf{d}_{\mathrm{BS},*}^{j+1}\} = \{\mathbf{d}_{\mathrm{BS}}^{j}\} + \{\dot{\mathbf{d}}_{\mathrm{BS}}^{j}\}\Delta t + \frac{1}{2}\{\ddot{\mathbf{d}}_{\mathrm{BS}}^{j}\}\Delta t^2, \tag{2.37b}$$

further, β and γ are weights. Using $\beta = 1/4$ and $\gamma = 1/2$ the approximation is made, which states that acceleration is constant during the whole time and is equal to the mean value of two accelerations in neighbouring time steps. Using these values, the Newmark algorithm is unconditionally stable. Since no system matrix transformation is necessary, the Newmark method performs a time domain solution faster and more efficient respect to computer memory.

Finally, the same numerical model is solved in time domain using two different, above described integration schemes. The results obtained from both models show acceptable accuracy, cf. Subsection 2.3.3.

2.2.4 Frequency domain solution

Generally, Fourier transformation is used to transform time series of displacements, loads. etc. from time domain to frequency domain:

$$\mathbf{F}(x,\omega) = \int_{-\infty}^{\infty} \mathbf{f}(x,t)e^{-\mathrm{i}\omega t}\mathrm{d}t, \tag{2.38}$$

where i is the imaginary unit $\mathrm{i} = \sqrt{-1}$, $\mathbf{F}(x,\omega)$ denotes a function in frequency domain, $\mathbf{f}(x,t)$ is a function in time domain and ω is circular frequency. Consequently, inverse Fourier transformation is expressed as:

$$\mathbf{f}(x,t) = \frac{1}{2\pi}\int_{-\infty}^{\infty} \mathbf{F}(x,\omega)e^{\mathrm{i}\omega t}\mathrm{d}\omega. \tag{2.39}$$

Discrete Fourier transformation and discrete inverse Fourier transformation are performed using Fast Fourier Transformation (FFT) and Inverse Fast Fourier Transformation (IFFT) algorithms.

In order to obtain frequency domain solution, equivalent equation of motion for a frequency domain is solved for each of the circular frequencies:

$$[\mathbf{Z}^j]\{\mathbf{D}^j\} = \{\mathbf{F}^j\}; \qquad [\mathbf{Z}^j] = -(\omega^j)^2[\mathbf{M}] + i\omega^j[\mathbf{C}] + [\mathbf{K}], \tag{2.40}$$

where $[\mathbf{Z}^j]$ is dynamic stiffness matrix for the circular frequency $\omega^j = 2\pi(j-1)/T$, where $j = 1, 2, ..., J$ and T denotes total time used in solution. $[\mathbf{M}]$, $[\mathbf{C}]$ and $[\mathbf{K}]$ represent global mass, damping and stiffness matrices used in original FEM equation of motion Equation 2.27. $\{\mathbf{D}^j\}$ and $\{\mathbf{F}^j\}$ are the Fourier transforms of the discrete time series of the generalized displacement and the external load vectors, respectively.

2.2.5 Modal analysis

Modal analysis is a helpful tool dealing with multi-degree-of-freedom (MDOF) systems because it allows to analyse structural modes separately. Therefore, just the most contributing modes can be added in the solution, while less important modes can be excluded. Due to that, a lot of computational power and time can be saved. Usually the most important ones are just the first few modes. A modal analysis can be described in three steps:

- Reduction of MDOF system to a number of single-degree-of-freedom (SDOF) systems;
- Full FEM equations of motion in modal coordinates are solved for each SDOF system;
- Solution for MDOF is achieved adding all obtained solutions for SDOF systems.

A system must be linear in order to analyse it by modal analysis. Also eigenmodes must be independent of each other.
Solving the eigenvalue problem is a part of modal analysis. Thus, a brief introduction to it is given, before equations of motion in modal coordinates and modal matrices are defined.

Algebraic equation for a general eigenvalue problem is written by following expression:

$$([\mathbf{K}] - \lambda_{(j)}[\mathbf{M}])\{\breve{\Phi}_{(j)}\} = \mathbf{0}, \qquad \lambda_{(j)} = \omega_{(j)}^2, j = 1, 2, ..., J, \tag{2.41}$$

where $\omega_{(j)}$ is circular frequency, $\lambda_{(j)}$ is an eigenvalue and $\breve{\Phi}_{(j)}$ is an eigenmode. For every $\lambda_{(j)}$ there is one solution $\breve{\Phi}_{(j)}$, in terms of "direction". However, the length of eigenvector is not uniquely defined. Usually it is scaled to provide a modal mass of 1. Derivation of eigenvalue problem algebraic equation and solutions to it, is given at Cook [7].

Now, when general eigenvalue problem is defined, FEM equation of motion for modal analysis can be written:

$$[\mathbf{S}]^T[\mathbf{M}][\mathbf{S}]\{\ddot{\mathbf{q}}(t)\} + [\mathbf{S}]^T[\mathbf{C}][\mathbf{S}]\{\dot{\mathbf{q}}(t)\} + [\mathbf{S}]^T[\mathbf{K}][\mathbf{S}]\{\mathbf{q}(t)\} = [\mathbf{S}]^T\{\mathbf{f}(t)\}, \tag{2.42}$$

where $[\mathbf{S}]$ is the matrix storing the eigenvectors in columns. For a solution containing eigenmodes from one to J, the matrix $[\mathbf{S}]$ can be expressed as:

$$[\mathbf{S}] = \left[\{\breve{\Phi}_{(1)}\} \quad \{\breve{\Phi}_{(2)}\} \quad \cdots \quad \{\breve{\Phi}_{(J)}\}\right], \tag{2.43}$$

$\{\mathbf{q}(t)\}$ is a vector with the modal coordinates, cf. Nielsen [9]. Equation 2.42 is obtained from general FEM equation of motion Equation 2.27 substituting $\{\mathbf{d}_{\mathrm{BS}}(t)\}$ by $[\mathbf{S}]\{\mathbf{q}(t)\}$ and pre-multiplying every member by $[\mathbf{S}]^T$.

The MDOF system is solved using equations of motion in modal coordinates applied for a number of SDOF systems:

$$[\mathbf{M}_{\mathrm{m}}]\{\ddot{\mathbf{q}}(t)\} + [\mathbf{C}_{\mathrm{m}}]\{\dot{\mathbf{q}}(t)\} + [\mathbf{K}_{\mathrm{m}}]\{\mathbf{q}(t)\} = \{\mathbf{f}_{\mathrm{m}}(t)\}. \tag{2.44}$$

The modal matrices are defined as:

- $[\mathbf{M}_{\mathrm{m}}] = [\mathbf{S}]^T[\mathbf{M}][\mathbf{S}]$ is a modal mass matrix;
- $[\mathbf{C}_{\mathrm{m}}] = [\mathbf{S}]^T[\mathbf{C}][\mathbf{S}]$ is a modal damping matrix;
- $[\mathbf{K}_{\mathrm{m}}] = [\mathbf{S}]^T[\mathbf{K}][\mathbf{S}]$ is a modal stiffness matrix;
- $\{\mathbf{f}_{\mathrm{m}}(t)\} = [\mathbf{S}]^T\{\mathbf{f}(t)\}$ is a modal force vector.

$[\mathbf{M}_{\mathrm{m}}] = [\mathbf{S}]^T[\mathbf{M}][\mathbf{S}]$ and $[\mathbf{K}_{\mathrm{m}}] = [\mathbf{S}]^T[\mathbf{M}][\mathbf{S}]$ are diagonal matrices and so is $[\mathbf{C}_{\mathrm{m}}] = [\mathbf{S}]^T[\mathbf{M}][\mathbf{S}]$ when Rayleigh damping is employed.

2.3 Comparison between analytical and finite element models

In this section, a comparison between the deflections of a simply supported beam, considered in the analytical solution and in the numerical model, is presented. Also specifications of each model are given and exact parameters used in calculations are introduced. The bridge model is described in Subsection 2.3.1, while parameter sensitivity analysis is done regarding deflection dependency on varying locomotive speed and bridge length, in Subsection 2.3.2. Further, deflections obtained using analytical approach as well as the two numerical models, with different time integration schemes, are compared in Subsection 2.3.3.

2.3.1 Model of bridge and passing train

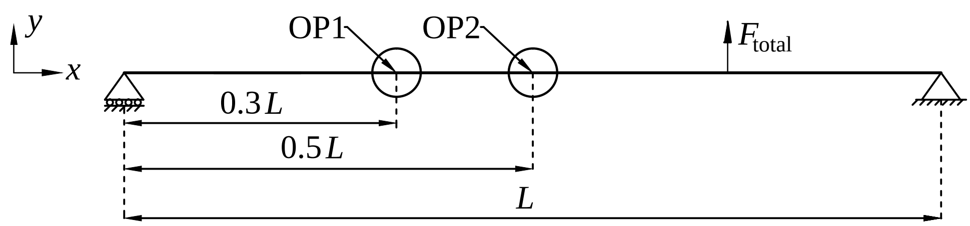

Figure 2.5: Simplified model of a bridge with a passing locomotive

A railway bridge structure is considered as a simply supported beam. The traversing locomotive is modelled just as a moving concentrated load equal to $F_{\mathrm{total}} = -M_{\mathrm{total}} \cdot g$ (where M_{total} is a mass of the vehicle) in the analytical solution and in the most basic numerical models based on FEM. Bridge model remains the same in all 2-D models. The most simple case of a bridge and a passing locomotive is illustrated in Figure 2.5 Geometrical dimensions of the bridge, material parameters and mass of the vehicle are given in Table 2.1.

Length of the bridge	L	28.4	m
Moment of inertia	$I_{\mathrm{b},z}$	4.08	m^4
Young's modulus	E_{b}	34	GPa
Mass density	ρ_{b}	2400	$\mathrm{kg/m}^3$
Damping ratio	ζ_{b}	0.01	–
Mass of the vehicle	M_{total}	69320	kg

Table 2.1: Properties of the model

The deflections of the bridge are extracted in observation points OP1 and OP2, shown in Figure 2.5. These exact points are chosen to investigate the effects of different mode shapes, i.e. at the length $0.5L$ deflection due to the first mode excitation is maximum but for the 2nd mode excitation is equal to zero. Thus, displacements of the bridge obtained at the mid-span are equal to zero for a number of mode shapes at OP2 position. To analyse the effects of these mode excitation, another observation point OP1 is introduced at length $0.3L$. First five mode shapes of the bridge are presented in Figure 2.6, where the coordinate x is normalized by the bridge length L.

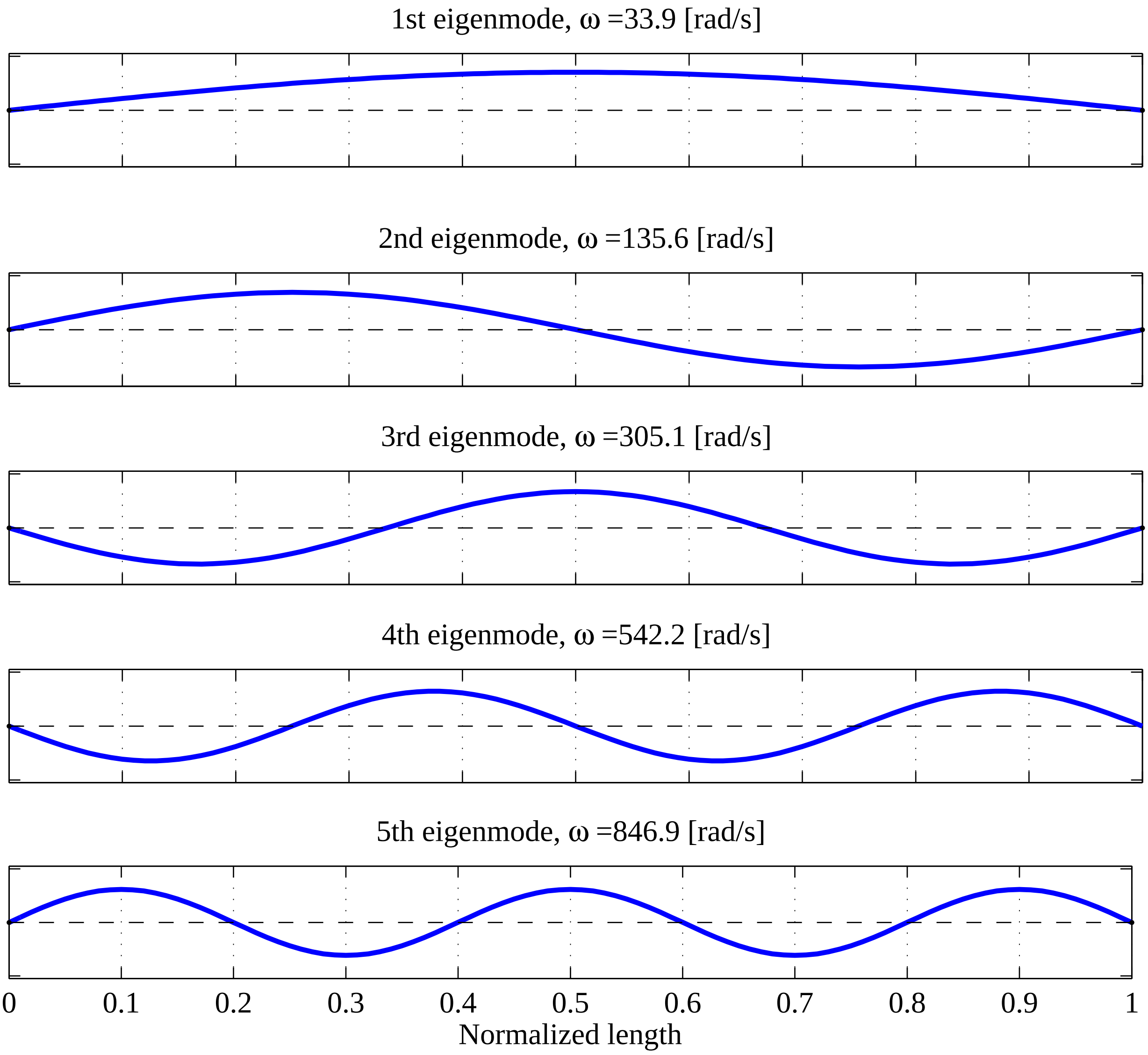

Figure 2.6: First five mode shapes of considered bridge

2.3.2 Parameter sensitivity analyses

A small study is done analysing bridge deflection variations due to changing bridge length and vehicle speed. The cross-section of the bridge, reinforced concrete parameters and the mass of the vehicle remain constant. Parameter sensitivity analyses are done using the basic analytical and two numerical models (one with Runge-Kutta fourth-order time integration and another one with Newmark second-order time integration scheme). The specifications of these models are given at Subsection 2.3.3.

Firstly, the bridge length is considered constant, equal to 28.4m and just the vehicle speed is changing from 10m/s (36km/h) to 100m/s (360km/h), cf. Figure 2.7.

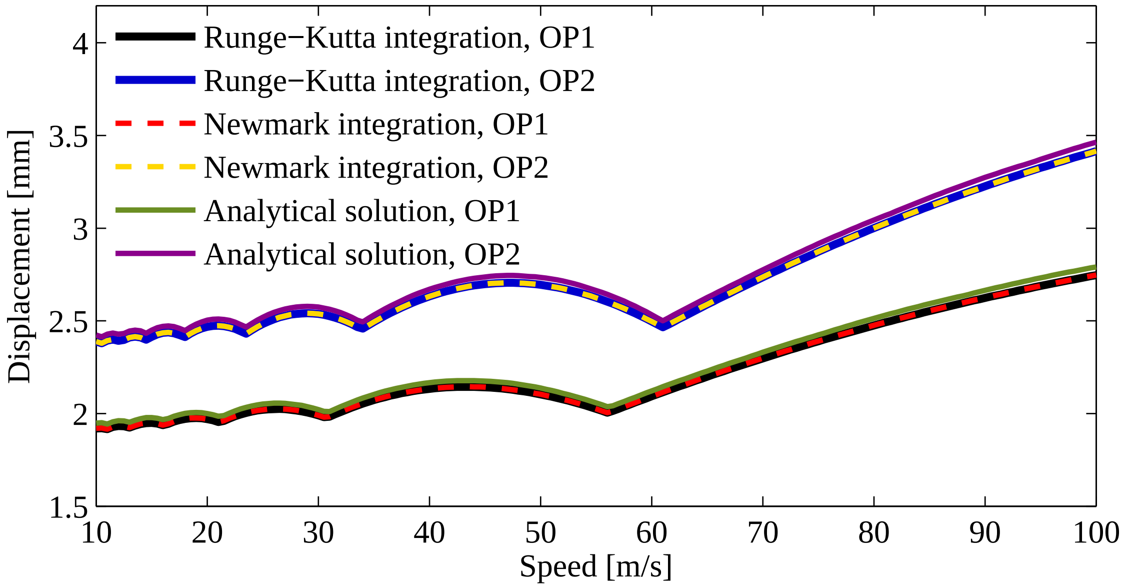

Figure 2.7: Bridge displacements at OP1 and OP2 positions due to varying locomotive speed

According to Figure 2.7, deflection of the bridge shows general tendency to increase with a higher vehicle speed. As it was expected bigger displacements are observed at OP2 position ($0.5L$). The graph shows that at certain speeds, the displacement reaches peaks with a local maximum value and later decreases to a local minimum value, e.g. at OP2 for a train speed of 29m/s the deflection is maximum 2.54mm (for both numerical models). The deflection decreases to 2.46mm at a speed of 34m/s. A bridge behaviour like this can be observed from a starting speed of 10m/s until the speed of 61m/s for OP2 and 56m/s for OP1. This phenomenon can be explained by the fact that at certain critical speeds different eigenmodes are excited, which affects the bridge deflection by increasing or decreasing it.

Figure 2.7 shows that two numerical models which use Runge-Kutta and Newmark time integration schemes provide virtually the same results, while analytical solution gives somewhat bigger values for bridge deflection. However, the difference between numerical and analytical solutions is up to 1.4% of the maximum absolute bridge deflection. The difference might be caused by different damping approaches used within the analytical and numerical models. It is considered that the numerical models and the analytical solution provide almost the same results.

In further analysis, two different vehicle speeds, 47m/s and 69m/s are considered. Both speeds provide very similar maximum absolute bridge deflection. However, the behaviour of the bridge is considerably different. The speed of 47m/s is chosen because it provides the local maximum deflection between speeds 34m/s and 61m/s, while 69m/s is the maximum vehicle speed considered. Thus, results are inspected for both speeds.

Secondly, the sensitivity analysis is performed keeping the vehicle speed constant (69m/s) and changing the length of the bridge from 15m to 70m, cf. Figure 2.8.

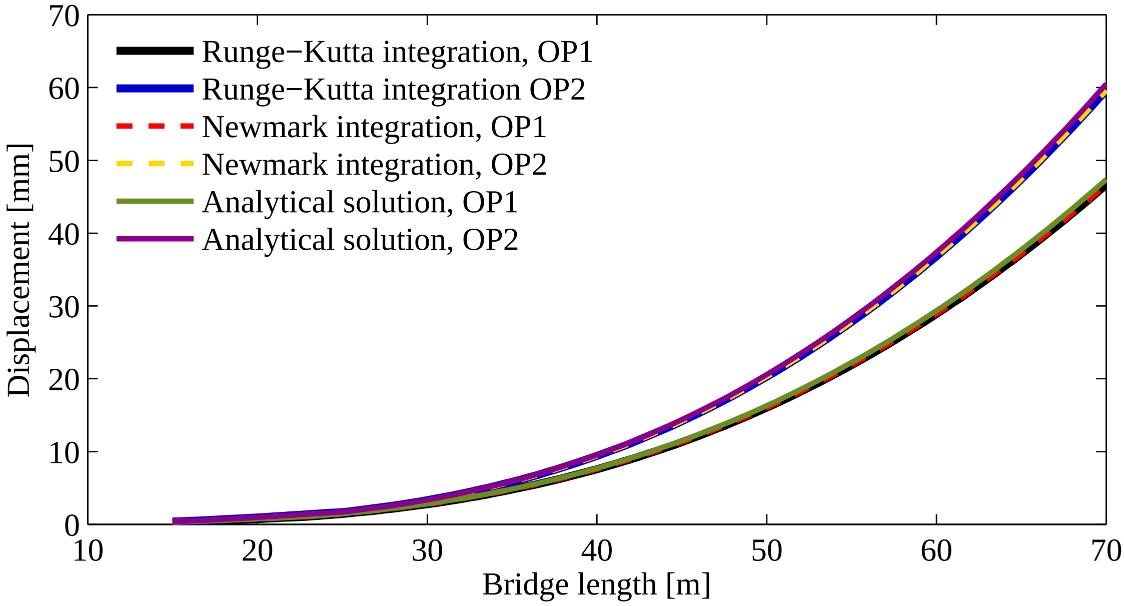

Figure 2.8: Bridge displacements at OP1 and OP2 positions according to varying bridge length

Figure 2.8 shows that the displacement is increasing with increasing bridge length, without any fluctuations. Also the deflections at position OP2 are bigger than those at OP1. Two numerical models provide the same results, while analytical model shows a small difference, up to 1.5% of a maximum absolute bridge deflection.

Regarding the bridge length, the maximum deflection seems to be increasing with increasing bridge length. Thus, only one length is analysed further in this chapter. A length of 28.4m is chosen because it is the length of an actual bridge from which the parameters like I_b, E_b, ζ_b etc. are taken.

It is important to point out that bridge length, cross-section and damping ratio, general mass of the vehicle, also reinforced concrete material parameters such as Young's modulus and mass density remain constant in the 2-D models described further on. The exact values are given in Subsection 2.3.1.

2.3.3 Analytical solution and basic numerical models

In this section, three models are compared between each other: analytical (Section 2.1), numerical using Newmark second-order time integration scheme (Subsection 2.2.3) and numerical using fourth-order Runge-Kutta time integration algorithm (Subsection 2.2.3). The vehicle is implemented as point load in all three models, cf. Figure 2.5. A brief specification of each model is given before presenting the results.

Analytical solution

The analytical solution provides reliable results just for first few eigenmodes of the bridge structure. Since mass proportional damping is used in the analytical solution, higher modes have too little damping which causes non-physical high frequency vibrations. Thus, just the first five modes are included in the analytical solution.

Runge-Kutta time integration

Numerical model, which uses Runge-Kutta fourth-order time integration algorithm provides accurate results. However, it does not work with consistent mass matrix, cf Equation 2.21. Thus, a lumped mass matrix, cf. Equation 2.25 has to be used. The drawbacks of this integration scheme are: doubling the sizes of FEM matrices and an extremely small time step is required to ensure stability of the solution, therefore computational time increases significantly. To decrease computational time, modal analysis is used, where just the first fives eigenmodes are included.

Newmark time integration

Numerical model, which uses Newmark second-order time integration scheme works way faster than the one with Runge-Kutta time integration, because it does not double the sizes of FEM matrices used. Also a bigger time step can be used, keeping satisfactory accuracy of the results. Since the model works fast, full solution is applied instead of a modal analysis, including all eigenmodes of the bridge structure. Furthermore, numerical model with Newmark time integration algorithm is unconditionally stable applying weights $\beta = 1/4$ and $\gamma = 1/2$ (cf. Subsection 2.2.3) when Runge-Kutta is just conditionally stable.

Bridge deflections obtained using these three models are presented in Figure 2.9 and Figure 2.10.

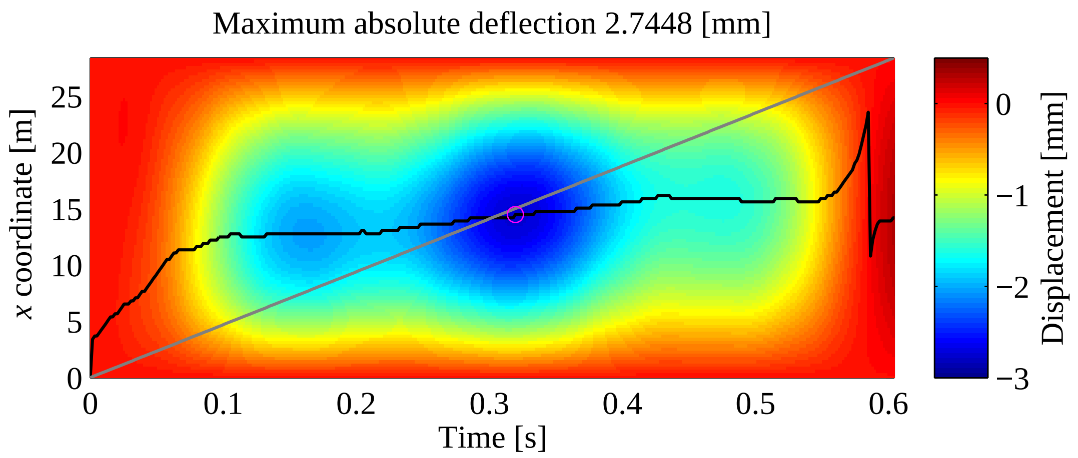

(a)

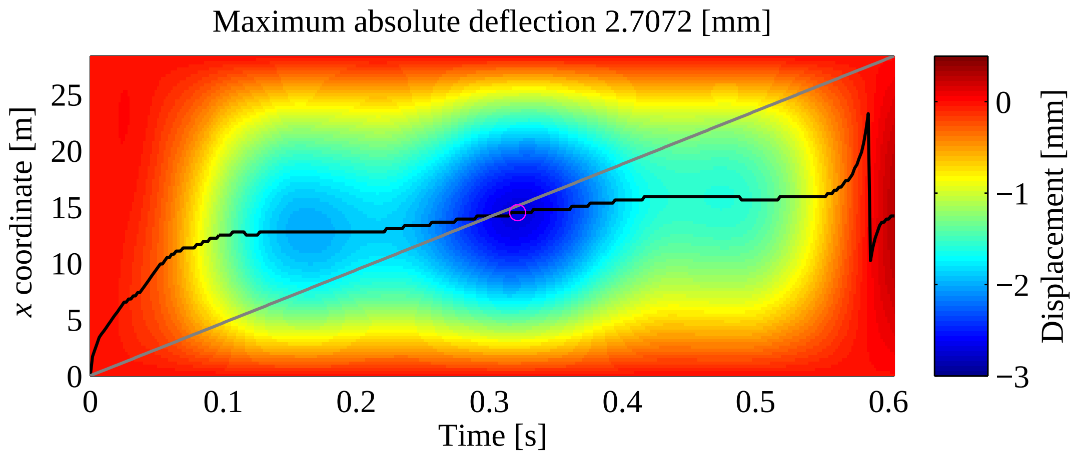

(b)

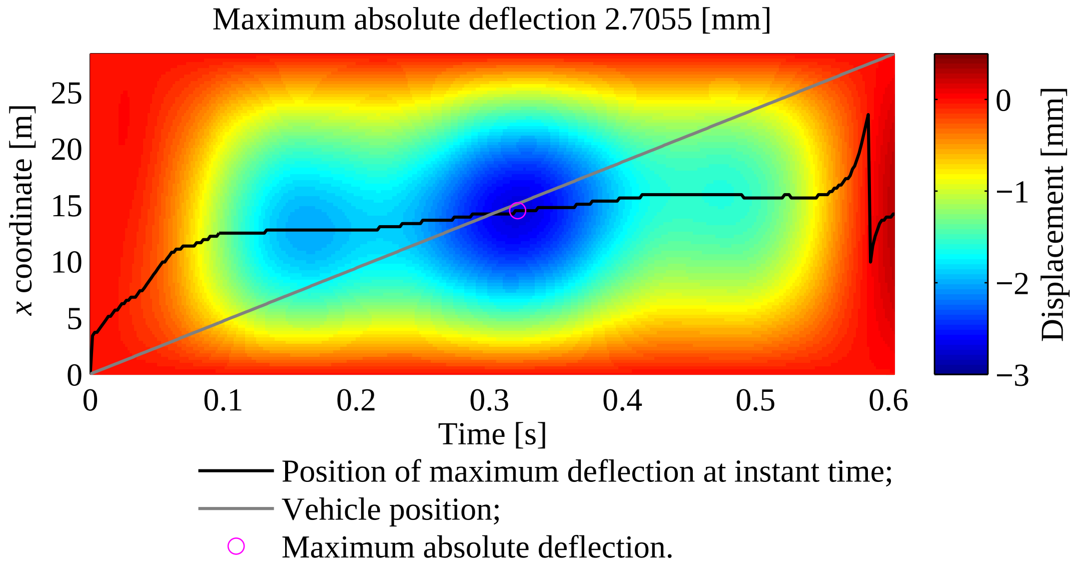

(c)

Figure 2.9: Bridge deflections at speed 47m/s. a) Analytical solution; b) Numerical model using Newmark second-order time integration scheme; c) Numerical model using Runge-Kutta fourth-order time integration algorithm

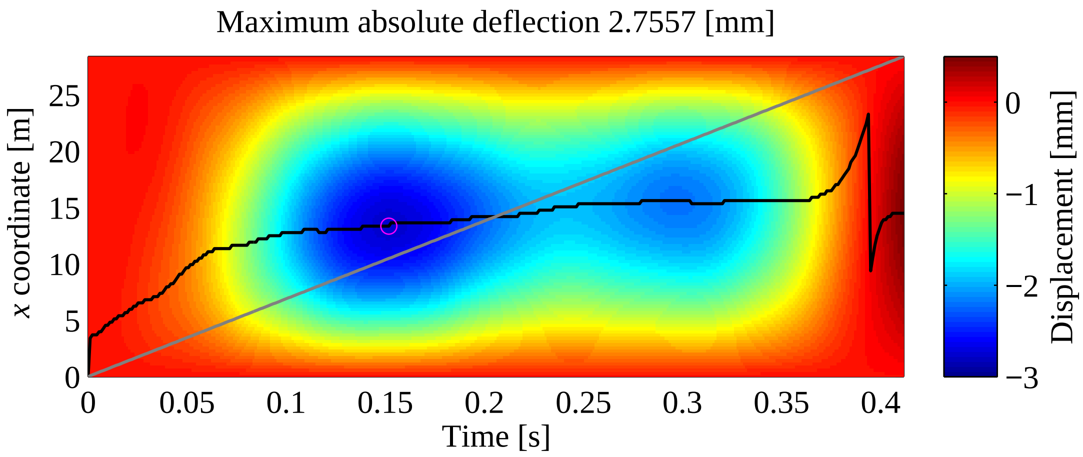

(a)

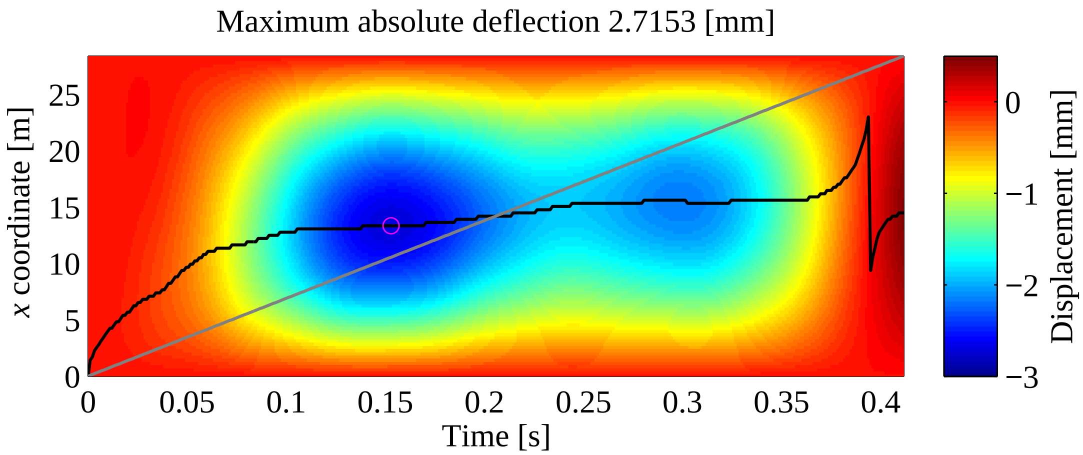

(b)

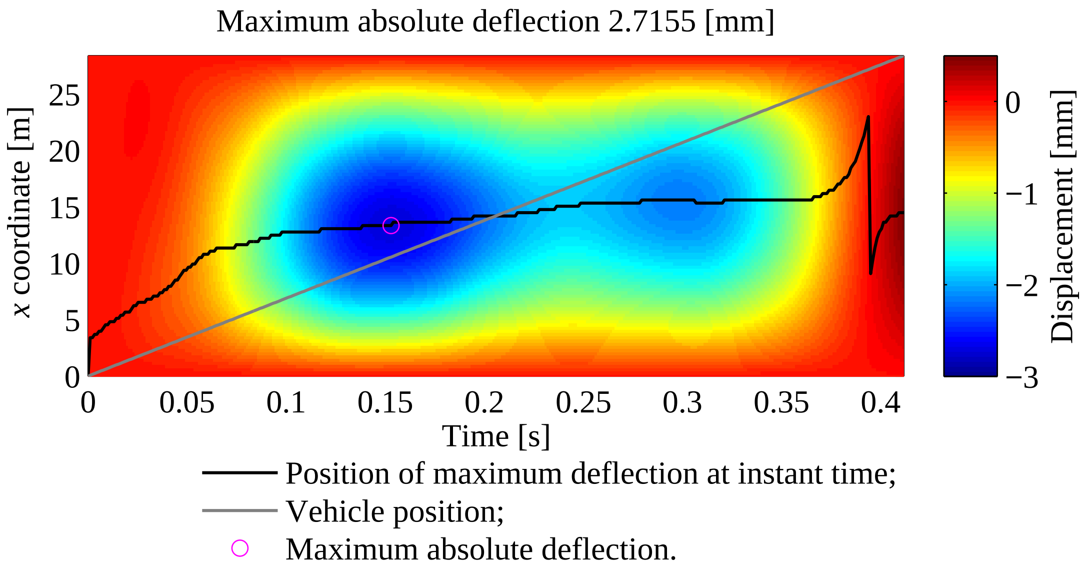

(c)

Figure 2.10: Bridge deflections at speed 69m/s. a) Analytical solution; b) Numerical model using Newmark second-order time integration scheme; c) Numerical model using Runge-Kutta fourth-order time integration algorithm

Firstly, it can be seen that three models compared in this section provide almost identical results, both in terms of maximum displacements and overall bridge behaviour. For example, the maximum difference of displacement between the analytical solution and numerical, the model with Runge-Kutta time integration scheme, at a locomotive speed of 47m/s is 0.0393mm. It is just 1.4% of the maximum absolute deflection.

Secondly, the values of maximum absolute displacements between two analysed speeds are very similar. However, the position and time, where these displacements are obtained on the bridge, are different. Figure 2.9 shows that at a vehicle speed of 47m/s the maximum absolute deflection is obtained when the load is at the middle of the bridge, while Figure 2.10 shows it approximately at $1/3$ of the bridge length at a vehicle speed 69m/s. It can be concluded that the bridge behaviour becomes more similar to a case of static loading with a decreasing train speed. However, at high locomotive speeds it shows different behaviour.

Generally, the analytical solution and the numerical solution, based on FEM, perform very similarly. However, the numerical solution is by far a more versatile way to analyse a finite structure. It is also a more convenient way to model the geometry of the structure itself, i.e. introduce different supports for the bridge, apply more than one active force at a time etc. Thus, further models of a bridge and a passing locomotive are solved numerically.

It is decided to use Newmark time integration algorithm in further models because of its unconditional stability and calculations speed. Runge-Kutta time integration provides virtually the same results but it has drawbacks, namely slow computation speed and conditional stability.

Chapter 3

Moving vehicle models on a two-dimensional beam element

In the previous chapter the influence from the train to the bridge was modelled only as a constant moving force. This, however, is not a good assumption, as the added mass from the train will have an effect on the behaviour of the bridge. Thus, various vehicle models are analysed in this chapter. In Section 3.1 a solution for a moving mass on a beam element is given, while in Section 3.2 a moving single-degree-of-freedom system is analysed. Finally, in Section 3.3 a solution for a moving multi-degree-of-freedom system is given. The comparison between these models is presented in Section 3.4.

3.1 Moving mass vehicle

To address the problem of the moving force the beam element equations derived in Section 2.2 are modified to include multiple added masses. The problem is illustrated in Figure 3.1. As it can be seen at distances $x_{\mathrm{w},i}$ there are point masses $M_{\mathrm{bm},i}$ and a number N_{w} of forces $F_{\mathrm{w},i}$ moving at speed c.

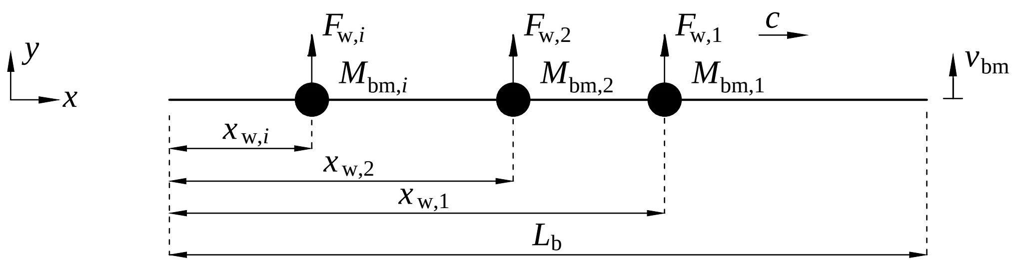

Figure 3.1: Beam element with point masses

The equation of motion for a system illustrated previously can be written as:

$$\rho_{\mathrm{b}} A_{\mathrm{b}} \frac{\partial^2 v_{\mathrm{bm}}(x,t)}{\partial t^2} + E_{\mathrm{b}} I_{\mathrm{b},z} \frac{\partial^4 v_{\mathrm{bm}}(x,t)}{\partial x^4} + \sum_{i=1}^{N_{\mathrm{w}}} \delta(x - x_{\mathrm{w},i}(t)) M_{\mathrm{bm},i} \frac{\partial^2 v_{\mathrm{bm}}(x,t)}{\partial t^2} = \sum_{i=1}^{N_{\mathrm{w}}} \delta(x - x_{\mathrm{w},i}(t)) F_{\mathrm{w},i}. \quad (3.1)$$

The weak form of differential Equation 3.1 is:

$$\begin{aligned}
&\int_0^{L_\mathrm{b}} \delta v_\mathrm{bm}(x,t)\rho_\mathrm{b}A_\mathrm{b}\frac{\partial^2 v_\mathrm{bm}(x,t)}{\partial t^2}\mathrm{d}x + \int_0^{L_\mathrm{b}} \frac{\partial^2 \delta v_\mathrm{bm}(x,t)}{\partial x^2}E_\mathrm{b}I_{\mathrm{b},z}\frac{\partial^2 v_\mathrm{bm}(x,t)}{\partial x^2}\mathrm{d}x \\
&+\sum_{i=1}^{N_\mathrm{w}}\int_0^{L_\mathrm{b}} \delta v_\mathrm{bm}(x,t)\,\delta(x-x_{\mathrm{w},i}(t))\,M_{\mathrm{bm},i}\,\frac{\partial^2 v_\mathrm{bm}(x,t)}{\partial t^2}\mathrm{d}x = \Bigg[\delta v_\mathrm{bm}(x,t)Q_{\mathrm{bm},y}(x,t)\Bigg]_0^{L_\mathrm{b}} \\
&+\Bigg[\frac{\partial\,\delta v_\mathrm{bm}(x,t)}{\partial x}M_{\mathrm{bm},z}(x,t)\Bigg]_0^{L_\mathrm{b}} + \sum_{i=1}^{N_\mathrm{w}}\int_0^{L_\mathrm{b}} \delta v_\mathrm{bm}(x,t)\,\delta(x-x_{\mathrm{w},i}(t))F_{\mathrm{w},i}\mathrm{d}x.
\end{aligned} \tag{3.2}$$

In finite element formulation, Equation 3.2 is written as:

$$[\mathbf{M}_\mathrm{BM}]\{\ddot{\mathbf{d}}_\mathrm{BM}(t)\} + [\mathbf{C}_\mathrm{BM}]\{\dot{\mathbf{d}}_\mathrm{BM}(t)\} + [\mathbf{K}_\mathrm{BM}]\{\mathbf{d}_\mathrm{BM}(t)\} = \{\mathbf{f}_\mathrm{BM}(t)\}, \tag{3.3}$$

where $[\mathbf{K}_\mathrm{BM}]$ and $[\mathbf{C}_\mathrm{BM}]$ are stiffness and damping mass matrices, respectively, and $\{\mathbf{f}_\mathrm{BM}\}$ is force vector.

$$[\mathbf{K}_\mathrm{BM}] = [\mathbf{K}_\mathrm{BS}], \tag{3.4a}$$
$$[\mathbf{C}_\mathrm{BM}] = [\mathbf{C}_\mathrm{BS}], \tag{3.4b}$$
$$\{\mathbf{f}_\mathrm{BM}\} = \{\mathbf{f}_\mathrm{BS}\}, \tag{3.4c}$$

where $[\mathbf{K}_\mathrm{BS}]$, $[\mathbf{C}_\mathrm{BS}]$ and $\{\mathbf{f}_\mathrm{BS}\}$ are defined in Section 2.2. The mass matrix $[\mathbf{M}_\mathrm{BM}(t)]$ can be described as a sum of two components:

$$[\mathbf{M}_\mathrm{BM}(t)] = [\mathbf{M}_\mathrm{BS}] + [\mathbf{M}_{\mathrm{BM},0}(t)], \tag{3.5}$$

where $[\mathbf{M}_\mathrm{BS}]$ is the consistent element mass matrix, cf. Equation 2.21 and $[\mathbf{M}_{\mathrm{BM},0}]$, is the influence from added masses $M_{\mathrm{bm},i}$. Assuming that $v_\mathrm{bm}(x,t) = \{\check{\Phi}(x)\}\{\mathbf{d}_\mathrm{BM}(t)\}$ and $\delta v_\mathrm{bm}(x,t) = \{\delta\,\mathbf{d}_\mathrm{BM}(t)\}^T\{\check{\Phi}(x)\}^T$ it can be expressed as:

$$[\mathbf{M}_{\mathrm{BM},0}(t)] = \sum_{i=1}^{N_\mathrm{w}}\{\check{\Phi}(x_{\mathrm{w},i}(t))\}^T M_{\mathrm{bm},i}\{\check{\Phi}(x_{\mathrm{w},i}(t))\}$$

$$= \sum_{i=1}^{N_\mathrm{w}} M_{\mathrm{bm},i}\begin{bmatrix}
\left(1-\frac{3x_{\mathrm{w},i}^2}{L_\mathrm{b}^2}+\frac{2x_{\mathrm{w},i}^3}{L_\mathrm{b}^3}\right)^2 & \left(1-\frac{3x_{\mathrm{w},i}^2}{L_\mathrm{b}}+\frac{2x_{\mathrm{w},i}^3}{L_\mathrm{b}^3}\right)\left(x-\frac{2x_{\mathrm{w},i}^2}{L_\mathrm{b}}+\frac{x_{\mathrm{w},i}^3}{L_\mathrm{b}^2}\right) & \left(1-\frac{3x_{\mathrm{w},i}^2}{L_\mathrm{b}^2}+\frac{2x_{\mathrm{w},i}^3}{L_\mathrm{b}^3}\right)\left(\frac{3x_{\mathrm{w},i}^2}{L_\mathrm{b}^2}-\frac{2x_{\mathrm{w},i}^3}{L_\mathrm{b}^3}\right) & \left(1-\frac{3x_{\mathrm{w},i}^2}{L_\mathrm{b}^2}+\frac{2x_{\mathrm{w},i}^3}{L_\mathrm{b}^3}\right)\left(-\frac{x_{\mathrm{w},i}^2}{L_\mathrm{b}}+\frac{x_{\mathrm{w},i}^3}{L_\mathrm{b}^2}\right) \\
 & \left(x-\frac{2x_{\mathrm{w},i}^2}{L_\mathrm{b}}+\frac{x_{\mathrm{w},i}^3}{L_\mathrm{b}^2}\right)^2 & \left(x-\frac{2x_{\mathrm{w},i}^2}{L_\mathrm{b}}+\frac{x_{\mathrm{w},i}^3}{L_\mathrm{b}^2}\right)\left(\frac{3x_{\mathrm{w},i}^2}{L_\mathrm{b}^2}-\frac{2x_{\mathrm{w},i}^3}{L_\mathrm{b}^3}\right) & \left(x-\frac{2x_{\mathrm{w},i}^2}{L_\mathrm{b}}+\frac{x_{\mathrm{w},i}^3}{L_\mathrm{b}^2}\right)\left(-\frac{x_{\mathrm{w},i}^2}{L_\mathrm{b}}+\frac{x_{\mathrm{w},i}^3}{L_\mathrm{b}^2}\right) \\
 \mathit{Symm} & & \left(\frac{3x_{\mathrm{w},i}^2}{L_\mathrm{b}^2}-\frac{2x_{\mathrm{w},i}^3}{L_\mathrm{b}^3}\right)^2 & \left(\frac{3x_{\mathrm{w},i}^2}{L_\mathrm{b}^2}-\frac{2x_{\mathrm{w},i}^3}{L_\mathrm{b}^3}\right)\left(-\frac{x_{\mathrm{w},i}^2}{L_\mathrm{b}}+\frac{x_{\mathrm{w},i}^3}{L_\mathrm{b}^2}\right) \\
 & & & \left(-\frac{x_{\mathrm{w},i}^2}{L_\mathrm{b}}+\frac{x_{\mathrm{w},i}^3}{L_\mathrm{b}^2}\right)^2
\end{bmatrix}$$

(3.6)

where $x_{\mathrm{w},i} = x_{\mathrm{w},i}(t)$. Thus, the mass matrix $[\mathbf{M}_{\mathrm{BM}}(t)]$ becomes time dependent. Applying the influence of the train mass on a bridge the dynamic behaviour can be modelled more precisely.

3.2 Single-degree-of-freedom vehicle

One way of modelling the effects from a moving train to a bridge is by modelling the train as a number of SDOF vehicles. The *i*th SDOF vehicle can be described by mass $M_{\mathrm{h},i}$, spring stiffness $K_{\mathrm{h},i}$ and viscous damping $C_{\mathrm{h},i}$. Also using this model it is possible to include the effects of an uneven track. The track profile is modelled as a stationary stochastic process and is described in Appendix A. The vertical displacement of the SDOF vehicle is denoted $v_{\mathrm{h},i} = v_{\mathrm{h},i}(t)$, while the displacement of the beam is $v_{\mathrm{bh}} = v_{\mathrm{bh}}(x,t)$. The beam surface has the irregularities denoted by $r = r(x)$.

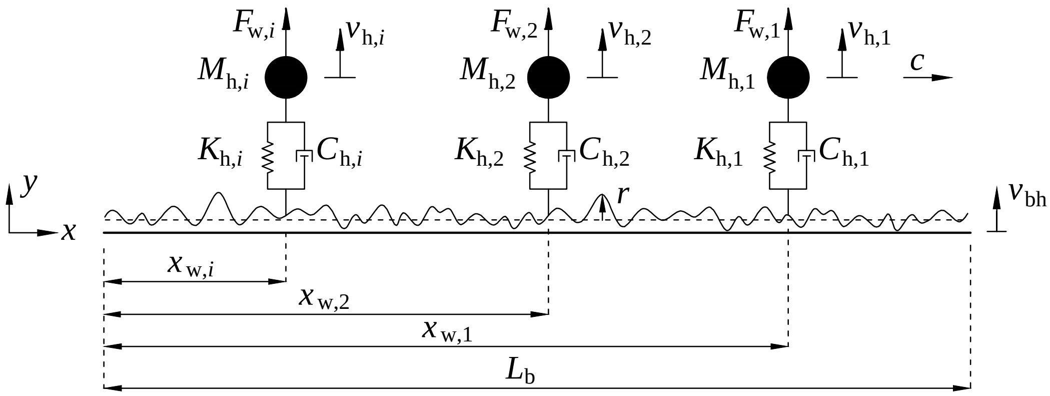

Figure 3.2: SDOF system moving along a Euler-Bernoulli beam element

The governing equation of motion for the beam is as follows:

$$\rho_{\mathrm{b}} A_{\mathrm{b}} \frac{\partial^2 v_{\mathrm{bh}}(x,t)}{\partial t^2} + E_{\mathrm{b}} I_{\mathrm{b},z} \frac{\partial^4 v_{\mathrm{bh}}(x,t)}{\partial x^4} + \sum_{i=1}^{N_{\mathrm{w}}} \delta(x - x_{\mathrm{w},i}(t)) K_{\mathrm{h},i} \big(v_{\mathrm{bh},i}(x,t) + r(x) - v_{\mathrm{h},i}(t) \big)$$
$$+ \sum_{i=1}^{N_{\mathrm{w}}} \delta(x - x_{\mathrm{w},i}(t)) C_{\mathrm{h},i} \left(\frac{\partial v_{\mathrm{bh}}(x,t)}{\partial t} + c \frac{\mathrm{d}r(x)}{\mathrm{d}x} - \frac{\mathrm{d}v_{\mathrm{h},i}(t)}{\mathrm{d}t} \right) = 0. \quad (3.7)$$

For the *i*th SDOF vehicle the equation of motion is described as:

$$M_{\mathrm{h},i} \frac{\mathrm{d}^2 v_{\mathrm{h},i}(t)}{\mathrm{d}t^2} + K_{\mathrm{h},i} \big(- v_{\mathrm{bh}}(x,t) - r(x) + v_{\mathrm{h},i}(t) \big)$$
$$+ C_{\mathrm{h},i} \left(- \frac{\partial v_{\mathrm{bh}}(x,t)}{\partial t} - c \frac{\mathrm{d}r(x)}{\mathrm{d}x} + \frac{\mathrm{d}v_{\mathrm{h},i}(t)}{\mathrm{d}t} \right) = F_{\mathrm{w},i}. \quad (3.8)$$

Rearranging and transforming these equations the following is obtained:

$$
\begin{aligned}
&\int_0^{L_\mathrm{b}} \delta v_\mathrm{bh}(x,t)\rho_\mathrm{b}A_\mathrm{b}\frac{\partial^2 v_\mathrm{bh}(x,t)}{\partial t^2}\mathrm{d}x + \int_0^{L_\mathrm{b}} \frac{\partial^2 \delta v_\mathrm{bh}(x,t)}{\partial x^2}E_\mathrm{b}I_{\mathrm{b},z}\frac{\partial^2 v_\mathrm{bh}(x,t)}{\partial x^2}\mathrm{d}x \\
&+\sum_{i=1}^{N_\mathrm{w}}\int_0^{L_\mathrm{b}} \delta v_\mathrm{bh}(x,t)\,\delta(x-x_{\mathrm{w},i}(t))K_{\mathrm{h},i}\big(v_\mathrm{bh}(x,t)-v_{\mathrm{h},i}(t)\big)\mathrm{d}x \\
&+\sum_{i=1}^{N_\mathrm{w}}\int_0^{L_\mathrm{b}} \delta v_\mathrm{bh}(x,t)\,\delta(x-x_{\mathrm{w},i}(t))\,C_{\mathrm{h},i}\left(\frac{\partial v_\mathrm{bh}(x,t)}{\partial t}-\frac{\mathrm{d}v_{\mathrm{h},i}(t)}{\mathrm{d}t}\right)\mathrm{d}x \\
&=\Big[\delta v_\mathrm{bh}(x,t)Q_{\mathrm{bh},y}(x,t)\Big]_0^{L_\mathrm{b}}+\left[\frac{\partial \delta v_\mathrm{bh}(x,t)}{\partial x}M_{\mathrm{bh},z}(x,t)\right]_0^{L_\mathrm{b}} \\
&-\sum_{i=1}^{N_\mathrm{w}}\int_0^{L_\mathrm{b}} \delta v_\mathrm{bh}(x,t)\delta(x-x_{\mathrm{w},i}(t))K_{\mathrm{h},i}r(x)\mathrm{d}x-\sum_{i=1}^{N_\mathrm{w}}\int_0^{L_\mathrm{b}} \delta v_\mathrm{bh}(x,t)\delta(x-x_{\mathrm{w},i}(t))\,c\,C_{\mathrm{h},i}\frac{\mathrm{d}r(x)}{\mathrm{d}x}\mathrm{d}x,
\end{aligned}
\tag{3.9}
$$

$$
\begin{aligned}
M_{\mathrm{h},i}\frac{\mathrm{d}^2 v_{\mathrm{h},i}(t)}{\mathrm{d}t^2}+K_{\mathrm{h},i}\big(-v_\mathrm{bh}(x,t)+v_{\mathrm{h},i}(t)\big)+C_{\mathrm{h},i}\left(\frac{\partial v_\mathrm{bh}(x,t)}{\partial t}+\frac{\mathrm{d}v_{\mathrm{h},i}(t)}{\mathrm{d}t}\right)& \\
=F_{\mathrm{w},i}+K_{\mathrm{h},i}r(x)+c\,C_{\mathrm{h},i}\frac{\mathrm{d}r(x)}{\mathrm{d}x}&.
\end{aligned}
\tag{3.10}
$$

Assuming that $v_\mathrm{bh}(x,t)=\{\check{\Phi}(x)\}\{\mathbf{d}_\mathrm{BH}(t)\}$ and $\delta v_\mathrm{bh}(x,t)=\{\delta\,\mathbf{d}_\mathrm{BH}(t)\}^T\{\check{\Phi}(x)\}^T$ the equations are expressed in finite element formulation:

$$
[\mathbf{M}_\mathrm{H}]\{\ddot{\mathbf{d}}_\mathrm{H}(t)\}+[\mathbf{C}_\mathrm{H}]\{\dot{\mathbf{d}}_\mathrm{H}(t)\}+[\mathbf{K}_\mathrm{H}]\{\mathbf{d}_\mathrm{H}(t)\}=\{\mathbf{f}_\mathrm{H}(t)\},
\tag{3.11}
$$

where $\{\mathbf{d}_\mathrm{H}(t)\}$ is the nodal displacement vector:

$$
\{\mathbf{d}_\mathrm{H}(t)\}=\left\{\begin{matrix}\{\mathbf{d}_\mathrm{BH}(t)\}\\ v_{\mathrm{h},1}(t)\\ v_{\mathrm{h},2}(t)\\ \vdots\\ v_{\mathrm{h},N_\mathrm{w}}(t)\end{matrix}\right\}=\left\{\begin{matrix}v_{\mathrm{bh},1}(t)\\ \psi_{\mathrm{bh},1}(t)\\ v_{\mathrm{bh},2}(t)\\ \psi_{\mathrm{bh},2}(t)\\ v_{\mathrm{h},1}(t)\\ v_{\mathrm{h},2}(t)\\ \vdots\\ v_{\mathrm{h},N_\mathrm{w}}(t)\end{matrix}\right\}\begin{matrix}\text{transverse displacement at the first node;}\\ \text{rotation at the first node;}\\ \text{transverse displacement at the second node;}\\ \text{rotation at the second node;}\\ \text{transverse displacement of mass } M_{\mathrm{h},1};\\ \text{transverse displacement of mass } M_{\mathrm{h},2};\\ \\ \text{transverse displacement of mass } M_{\mathrm{h},N_\mathrm{w}}.\end{matrix}
\tag{3.12}
$$

For a beam with N_w SDOF vehicles the stiffness matrix $[\mathbf{K}_\mathrm{H}]$ is expressed as:

$$[\mathbf{K}_\mathrm{H}] = \begin{bmatrix} [\mathbf{K}_{11}] & [\mathbf{K}_{12}] & [\mathbf{K}_{13}] & \cdots & [\mathbf{K}_{1N_\mathrm{w}}] \\ [\mathbf{K}_{21}] & K_{\mathrm{h},1} & \mathbf{0} & \cdots & \mathbf{0} \\ [\mathbf{K}_{31}] & \mathbf{0} & K_{\mathrm{h},2} & \cdots & \mathbf{0} \\ \vdots & \vdots & \vdots & \ddots & \vdots \\ [\mathbf{K}_{N_\mathrm{w}1}] & \mathbf{0} & \mathbf{0} & \cdots & K_{\mathrm{h},N_\mathrm{w}} \end{bmatrix}, \tag{3.13}$$

where the term $[\mathbf{K}_{11}]$ describes the stiffness for four degrees of freedom of a beam ($v_{\mathrm{bh},1}$, $\psi_{\mathrm{bh},1}$, $v_{\mathrm{bh},2}$, $\psi_{\mathrm{bh},2}$), while $K_{\mathrm{h},i}$ is the stiffness associated with the degree of freedom $v_{\mathrm{h},i}$ of the ith vehicle. Terms $[\mathbf{K}_{1i}]$ and $[\mathbf{K}_{i1}]$ describe the coupling between the beam and ith SDOF vehicle.

The stiffness associated with the degrees of freedom of the beam is also influenced by the stiffness of the SDOF vehicles and is expressed as:

$$[\mathbf{K}_{11}] = \int_0^{L_\mathrm{b}} \frac{\mathrm{d}^2\{\check{\Phi}(x)\}^T}{\mathrm{d}x^2} E_\mathrm{b} I_{\mathrm{b},z} \frac{\mathrm{d}^2\{\check{\Phi}(x)\}}{\mathrm{d}x^2}\mathrm{d}x + \sum_{i=1}^{N_\mathrm{w}} \{\check{\Phi}(x_{\mathrm{w},i})\}^T K_{\mathrm{h},i} \{\check{\Phi}(x_{\mathrm{w},i})\} = [\mathbf{K}_\mathrm{BS}]$$

$$+\sum_{i=1}^{N_\mathrm{w}} K_{\mathrm{h},i} \begin{bmatrix} \left(1-\frac{3x_{\mathrm{w},i}^2}{L_\mathrm{b}^2}+\frac{2x_{\mathrm{w},i}^3}{L_\mathrm{b}^3}\right)^2 & \left(1-\frac{3x_{\mathrm{w},i}^2}{L_\mathrm{b}}+\frac{2x_{\mathrm{w},i}^3}{L_\mathrm{b}^3}\right)\left(x-\frac{2x_{\mathrm{w},i}^2}{L_\mathrm{b}}+\frac{x_{\mathrm{w},i}^3}{L_\mathrm{b}^2}\right) & \left(1-\frac{3x_{\mathrm{w},i}^2}{L_\mathrm{b}^2}+\frac{2x_{\mathrm{w},i}^3}{L_\mathrm{b}^3}\right)\left(\frac{3x_{\mathrm{w},i}^2}{L_\mathrm{b}^2}-\frac{2x_{\mathrm{w},i}^3}{L_\mathrm{b}^3}\right) & \left(1-\frac{3x_{\mathrm{w},i}^2}{L_\mathrm{b}^2}+\frac{2x_{\mathrm{w},i}^3}{L_\mathrm{b}^3}\right)\left(-\frac{x_{\mathrm{w},i}^2}{L_\mathrm{b}}+\frac{x_{\mathrm{w},i}^3}{L_\mathrm{b}^2}\right) \\ & \left(x-\frac{2x_{\mathrm{w},i}^2}{L_\mathrm{b}}+\frac{x_{\mathrm{w},i}^3}{L_\mathrm{b}^2}\right)^2 & \left(x-\frac{2x_{\mathrm{w},i}^2}{L_\mathrm{b}}+\frac{x_{\mathrm{w},i}^3}{L_\mathrm{b}^2}\right)\left(\frac{3x_{\mathrm{w},i}^2}{L_\mathrm{b}^2}-\frac{2x_{\mathrm{w},i}^3}{L_\mathrm{b}^3}\right) & \left(x-\frac{2x_{\mathrm{w},i}^2}{L_\mathrm{b}}+\frac{x_{\mathrm{w},i}^3}{L_\mathrm{b}^2}\right)\left(-\frac{x_{\mathrm{w},i}^2}{L_\mathrm{b}}+\frac{x_{\mathrm{w},i}^3}{L_\mathrm{b}^2}\right) \\ \mathit{Symm} & & \left(\frac{3x_{\mathrm{w},i}^2}{L_\mathrm{b}^2}-\frac{2x_{\mathrm{w},i}^3}{L_\mathrm{b}^3}\right)^2 & \left(\frac{3x_{\mathrm{w},i}^2}{L_\mathrm{b}^2}-\frac{2x_{\mathrm{w},i}^3}{L_\mathrm{b}^3}\right)\left(-\frac{x_{\mathrm{w},i}^2}{L_\mathrm{b}}+\frac{x_{\mathrm{w},i}^3}{L_\mathrm{b}^2}\right) \\ & & & \left(-\frac{x_{\mathrm{w},i}^2}{L_\mathrm{b}}+\frac{x_{\mathrm{w},i}^3}{L_\mathrm{b}^2}\right)^2 \end{bmatrix} \tag{3.14}$$

The coupling terms for the ith SDOF vehicle are defined as:

$$[\mathbf{K}_{1i}] = [\mathbf{K}_{i1}]^T = -K_{\mathrm{h},i}\{\check{\Phi}(x_{\mathrm{w},i})\}^T = -K_{\mathrm{h},i} \begin{bmatrix} 1-\frac{3x_{\mathrm{w},i}^2}{L_\mathrm{b}^2}+\frac{2x_{\mathrm{w},i}^3}{L_\mathrm{b}^3} \\ x-\frac{2x_{\mathrm{w},i}^2}{L_\mathrm{b}}+\frac{x_{\mathrm{w},i}^3}{L_\mathrm{b}^2} \\ \frac{3x_{\mathrm{w},i}^2}{L_\mathrm{b}^2}-\frac{2x_{\mathrm{w},i}^3}{L_\mathrm{b}^3} \\ -\frac{x_{\mathrm{w},i}^2}{L_\mathrm{b}}+\frac{x_{\mathrm{w},i}^3}{L_\mathrm{b}^2} \end{bmatrix}. \tag{3.15}$$

The damping matrix $[\mathbf{C}_\mathrm{H}]$ is constructed in the same way as the stiffness matrix:

$$[\mathbf{C}_\mathrm{H}] = \begin{bmatrix} [\mathbf{C}_{11}] & [\mathbf{C}_{12}] & [\mathbf{C}_{13}] & \cdots & [\mathbf{C}_{1N_\mathrm{w}}] \\ [\mathbf{C}_{21}] & C_{\mathrm{h},1} & \mathbf{0} & \cdots & \mathbf{0} \\ [\mathbf{C}_{31}] & \mathbf{0} & C_{\mathrm{h},2} & \cdots & \mathbf{0} \\ \vdots & \vdots & \vdots & \ddots & \vdots \\ [\mathbf{C}_{N_\mathrm{w}1}] & \mathbf{0} & \mathbf{0} & \cdots & C_{\mathrm{h},N_\mathrm{w}} \end{bmatrix}, \tag{3.16}$$

where member $[\mathbf{C}_{11}]$ accounts for the damping of the beam as well as added damping from the SDOF vehicles, while $C_{\mathrm{h},i}$ is the damping associated with degree of freedom $v_{\mathrm{h},i}$ of the ith vehicle. Terms $[\mathbf{C}_{1i}]$ and $[\mathbf{C}_{i1}]$ describe the coupling between the beam and SDOF vehicle.

$$\begin{aligned} [\mathbf{C}_{11}] &= \alpha_\mathrm{R}[\mathbf{M}_\mathrm{BS}] + \beta_\mathrm{R}[\mathbf{K}_\mathrm{BS}] + \sum_{i=1}^{N_\mathrm{w}} \{\check{\Phi}(x_{\mathrm{w},i})\}^T C_{\mathrm{h},i} \{\check{\Phi}(x_{\mathrm{w},i})\} = \alpha_\mathrm{R}[\mathbf{M}_\mathrm{BS}] + \beta_\mathrm{R}[\mathbf{K}_\mathrm{BS}] \\ &+ \sum_{i=1}^{N_\mathrm{w}} C_{\mathrm{h},i} \begin{bmatrix} \left(1-\frac{3x_{\mathrm{w},i}^2}{L_\mathrm{b}^2}+\frac{2x_{\mathrm{w},i}^3}{L_\mathrm{b}^3}\right)^2 & \left(1-\frac{3x_{\mathrm{w},i}^2}{L_\mathrm{b}}+\frac{2x_{\mathrm{w},i}^3}{L_\mathrm{b}^3}\right)\left(x-\frac{2x_{\mathrm{w},i}^2}{L_\mathrm{b}}+\frac{x_{\mathrm{w},i}^3}{L_\mathrm{b}^2}\right) & \left(1-\frac{3x_{\mathrm{w},i}^2}{L_\mathrm{b}^2}+\frac{2x_{\mathrm{w},i}^3}{L_\mathrm{b}^3}\right)\left(\frac{3x_{\mathrm{w},i}^2}{L_\mathrm{b}^2}-\frac{2x_{\mathrm{w},i}^3}{L_\mathrm{b}^3}\right) & \left(1-\frac{3x_{\mathrm{w},i}^2}{L_\mathrm{b}^2}+\frac{2x_{\mathrm{w},i}^3}{L_\mathrm{b}^3}\right)\left(-\frac{x_{\mathrm{w},i}^2}{L_\mathrm{b}}+\frac{x_{\mathrm{w},i}^3}{L_\mathrm{b}^2}\right) \\ & \left(x-\frac{2x_{\mathrm{w},i}^2}{L_\mathrm{b}}+\frac{x_{\mathrm{w},i}^3}{L_\mathrm{b}^2}\right)^2 & \left(x-\frac{2x_{\mathrm{w},i}^2}{L_\mathrm{b}}+\frac{x_{\mathrm{w},i}^3}{L_\mathrm{b}^2}\right)\left(\frac{3x_{\mathrm{w},i}^2}{L_\mathrm{b}^2}-\frac{2x_{\mathrm{w},i}^3}{L_\mathrm{b}^3}\right) & \left(x-\frac{2x_{\mathrm{w},i}^2}{L_\mathrm{b}}+\frac{x_{\mathrm{w},i}^3}{L_\mathrm{b}^2}\right)\left(-\frac{x_{\mathrm{w},i}^2}{L_\mathrm{b}}+\frac{x_{\mathrm{w},i}^3}{L_\mathrm{b}^2}\right) \\ \mathit{Symm} & & \left(\frac{3x_{\mathrm{w},i}^2}{L_\mathrm{b}^2}-\frac{2x_{\mathrm{w},i}^3}{L_\mathrm{b}^3}\right)^2 & \left(\frac{3x_{\mathrm{w},i}^2}{L_\mathrm{b}^2}-\frac{2x_{\mathrm{w},i}^3}{L_\mathrm{b}^3}\right)\left(-\frac{x_{\mathrm{w},i}^2}{L_\mathrm{b}}+\frac{x_{\mathrm{w},i}^3}{L_\mathrm{b}^2}\right) \\ & & & \left(-\frac{x_{\mathrm{w},i}^2}{L_\mathrm{b}}+\frac{x_{\mathrm{w},i}^3}{L_\mathrm{b}^2}\right)^2 \end{bmatrix} \end{aligned} \tag{3.17}$$

The coupling terms for the ith SDOF vehicle are defined as:

$$[\mathbf{C}_{1i}] = [\mathbf{C}_{i1}]^T = -C_{\mathrm{h},i}\{\check{\Phi}(x_{\mathrm{w},i})\}^T = -C_{\mathrm{h},i} \begin{bmatrix} 1-\frac{3x_{\mathrm{w},i}^2}{L_\mathrm{b}^2}+\frac{2x_{\mathrm{w},i}^3}{L_\mathrm{b}^3} \\ x-\frac{2x_{\mathrm{w},i}^2}{L_\mathrm{b}}+\frac{x_{\mathrm{w},i}^3}{L_\mathrm{b}^2} \\ \frac{3x_{\mathrm{w},i}^2}{L_\mathrm{b}^2}-\frac{2x_{\mathrm{w},i}^3}{L_\mathrm{b}^3} \\ -\frac{x_{\mathrm{w},i}^2}{L_\mathrm{b}}+\frac{x_{\mathrm{w},i}^3}{L_\mathrm{b}^2} \end{bmatrix}. \tag{3.18}$$

The mass matrix $[\mathbf{M}_{\mathrm{H}}]$ is defined as:

$$[\mathbf{M}_{\mathrm{H}}] = \begin{bmatrix} [\mathbf{M}_{11}] & \mathbf{0} & \mathbf{0} & \cdots & \mathbf{0} \\ \mathbf{0} & M_{\mathrm{h},1} & \mathbf{0} & \cdots & \mathbf{0} \\ \mathbf{0} & \mathbf{0} & M_{\mathrm{h},2} & \cdots & \mathbf{0} \\ \vdots & \vdots & \vdots & \ddots & \vdots \\ \mathbf{0} & \mathbf{0} & \mathbf{0} & \cdots & M_{\mathrm{h},N_{\mathrm{w}}} \end{bmatrix}, \tag{3.19}$$

where $[\mathbf{M}_{11}]$ is the consistent mass matrix of a beam as shown in Equation 2.21 and the mass of the ith vehicle is $M_{\mathrm{h},i}$.

Lastly, the force vector $\{\mathbf{f}_{\mathrm{H}}(t)\}$ is expressed as:

$$\{\mathbf{f}_{\mathrm{H}}(t)\} = \begin{Bmatrix} \{\mathbf{f}_{\mathrm{BH}}(t)\} \\ f_{\mathrm{h},1}(t) \\ f_{\mathrm{h},2}(t) \\ \vdots \\ f_{\mathrm{h},N_{\mathrm{w}}}(t) \end{Bmatrix}, \tag{3.20}$$

where $\{\mathbf{f}_{\mathrm{BH}}(t)\}$ is the forces acting on the beam, a combination of boundary load vector $\{\mathbf{f}_{\mathrm{BH,b}}(t)\}$ and track unevenness load vector $\{\mathbf{f}_{\mathrm{BH,u}}(t)\}$:

$$\begin{aligned} \{\mathbf{f}_{\mathrm{BH}}(t)\} = &-\left[\{\check{\Phi}(x)\}^T Q_{\mathrm{bh},y}(x,t)\right]_0^{L_{\mathrm{b}}} + \left[\frac{\mathrm{d}\{\check{\Phi}(x)\}^T}{\mathrm{d}x} M_{\mathrm{bh},z}(x,t)\right]_0^{L_{\mathrm{b}}} \\ &- \sum_{i=1}^{N_{\mathrm{w}}} \{\check{\Phi}(x)\}^T \left(K_{\mathrm{h},i}\, r(x) + c\, C_{\mathrm{h},i} \frac{\mathrm{d}r(x)}{\mathrm{d}x}\right) = \{\mathbf{f}_{\mathrm{BH,b}}(t)\} + \{\mathbf{f}_{\mathrm{BH,u}}(t)\}, \end{aligned} \tag{3.21}$$

$$\{\mathbf{f}_{\mathrm{BH,u}}(t)\} = -\sum_{i=1}^{N_{\mathrm{w}}} \left(K_{\mathrm{h},i}\, r(x) + c\, C_{\mathrm{h},i} \frac{\mathrm{d}r(x)}{\mathrm{d}x}\right) \begin{bmatrix} 1 - \frac{3x_{\mathrm{w},i}^2}{L_{\mathrm{b}}^2} + \frac{2x_{\mathrm{w},i}^3}{L_{\mathrm{b}}^3} \\ x - \frac{2x_{\mathrm{w},i}^2}{L_{\mathrm{b}}} + \frac{x_{\mathrm{w},i}^3}{L_{\mathrm{b}}^2} \\ \frac{3x_{\mathrm{w},i}^2}{L_{\mathrm{b}}^2} - \frac{2x_{\mathrm{w},i}^3}{L_{\mathrm{b}}^3} \\ -\frac{x_{\mathrm{w},i}^2}{L_{\mathrm{b}}} + \frac{x_{\mathrm{w},i}^3}{L_{\mathrm{b}}^2} \end{bmatrix}. \tag{3.22}$$

The force acting on the ith SDOF vehicle is a sum of external force $F_{\mathrm{w},i}$ as well as the effects from track unevenness:

$$f_{\mathrm{h},i}(t) = F_{\mathrm{w},i} + K_{\mathrm{h},i} r(x) + c\, C_{\mathrm{h},i} \frac{\mathrm{d}r(x)}{\mathrm{d}x}. \tag{3.23}$$

3.3 Multi-degree-of-freedom vehicle

In order to properly model the influence of a passing train to a bridge, a multi-degree-of-freedom model for a vehicle is introduced. The model has ten degrees of freedom, which models the car body, bogies, wheels and suspension system between these parts.

The vehicle is defined as a coupling system of a locomotive with two layers of springs and dampers, between which bogies are included. Wheels are coupled with the beam through springs and dashpots, the same principles apply as described in Section 3.2. The model for the analysis of dynamic response of the vehicle is shown in Figure 3.3. The vehicle model shown is based on Lei [10].

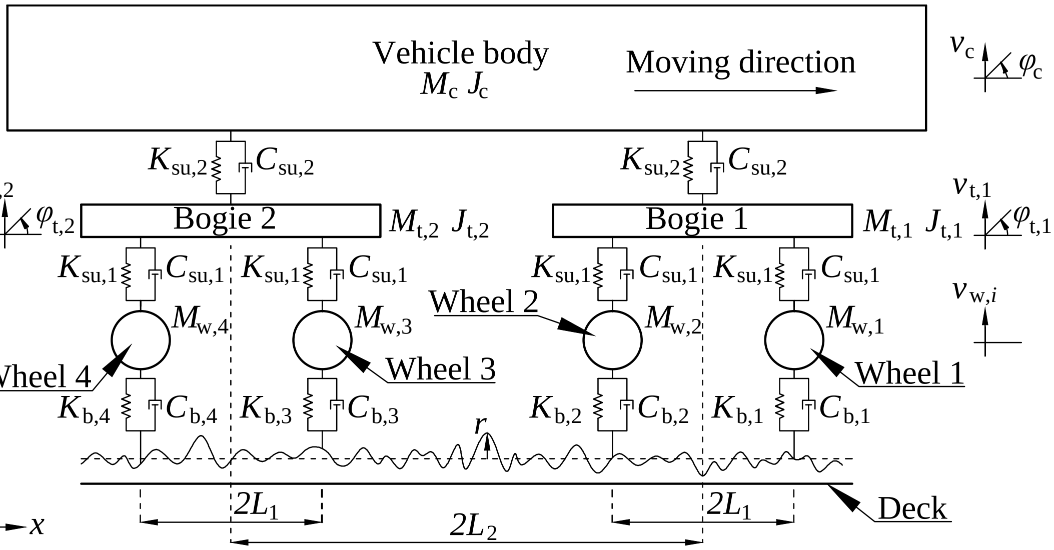

Figure 3.3: Multi-degree-of-freedom vehicle

The locomotive is considered as a rigid body with mass M_c and pitch moment of inertia J_c. It is connected with two bogies through spring–dashpot systems. Mass and pitch moments of inertia of the bogies are $M_{t,j}$ and $J_{t,j}$, respectively, where $j = 1,2$. Each bogie is connected to two wheels using similar spring–dashpot systems and the wheels are described by a wheel mass $M_{w,i}$, $i = 1,2,3,4$. The translations of the locomotive and bogies are defined by vertical displacements v_c and $v_{t,j}$, respectively, while pitch rotations are described by angles φ_c and $\varphi_{t,j}$. The vertical displacements of four wheels are denoted as $v_{w,i}$. The vehicle is described by ten equations of motion. Vertical displacement of the car body is affected by the secondary suspension system which has stiffness $K_{su,2}$ and damping $C_{su,2}$. Each wheel is loaded with one quarter of the total force $F_{total} = -M_{total} \cdot g$. Finite element formulation is as follows:

$$[\mathbf{M}_V]\{\ddot{\mathbf{d}}_V(t)\} + [\mathbf{C}_V]\{\dot{\mathbf{d}}_V(t)\} + [\mathbf{K}_V]\{\mathbf{d}_V(t)\} = \{\mathbf{f}_V(t)\}, \tag{3.24}$$

where the nodal displacement vector $\{\mathbf{d}_\mathrm{V}(t)\}$ is given as:

$$\{\mathbf{d}_\mathrm{V}(t)\} = \begin{Bmatrix} v_\mathrm{c}(t) \\ \varphi_\mathrm{c}(t) \\ v_{\mathrm{t},1}(t) \\ \varphi_{\mathrm{t},1}(t) \\ v_{\mathrm{t},2}(t) \\ \varphi_{\mathrm{t},2}(t) \\ v_{\mathrm{w},1}(t) \\ v_{\mathrm{w},2}(t) \\ v_{\mathrm{w},3}(t) \\ v_{\mathrm{w},4}(t) \end{Bmatrix} \begin{matrix} \text{transverse displacement of car body;} \\ \text{rotation of car body;} \\ \text{1st bogie transverse displacement;} \\ \text{1st bogie rotation;} \\ \text{2nd bogie transverse displacement;} \\ \text{2nd bogie rotation;} \\ \text{1st wheel transverse displacement;} \\ \text{2nd wheel transverse displacement;} \\ \text{3rd wheel transverse displacement;} \\ \text{4th wheel transverse displacement.} \end{matrix} \tag{3.25}$$

The stiffness matrix for the system $[\mathbf{K}_\mathrm{V}]$ is:

$$[\mathbf{K}_\mathrm{V}] = \begin{bmatrix} 2K_{\mathrm{su},2} & 0 & -K_{\mathrm{su},2} & 0 & -K_{\mathrm{su},2} & 0 & 0 & 0 & 0 & 0 \\ & 2L_2^2K_{\mathrm{su},2} & -L_2K_{\mathrm{su},2} & 0 & L_2K_{\mathrm{su},2} & 0 & 0 & 0 & 0 & 0 \\ & & 2K_{\mathrm{su},1}+K_{\mathrm{su},2} & 0 & 0 & 0 & -K_{\mathrm{su},1} & -K_{\mathrm{su},1} & 0 & 0 \\ & & & 2L_1^2K_{\mathrm{su},1} & 0 & 0 & -K_{\mathrm{su},1}L_1 & K_{\mathrm{su},1}L_1 & 0 & 0 \\ & & & & 2K_{\mathrm{su},1}+K_{\mathrm{su},2} & 0 & 0 & 0 & -K_{\mathrm{su},1} & -K_{\mathrm{su},1} \\ & & & & & 2L_1^2K_{\mathrm{su},1} & 0 & 0 & -K_{\mathrm{su},1}L_1 & K_{\mathrm{su},1}L_1 \\ & & & \mathit{Symm} & & & K_{\mathrm{su},1} & 0 & 0 & 0 \\ & & & & & & & K_{\mathrm{su},1} & 0 & 0 \\ & & & & & & & & K_{\mathrm{su},1} & 0 \\ & & & & & & & & & K_{\mathrm{su},1} \end{bmatrix} \tag{3.26}$$

while the damping matrix $[\mathbf{C}_\mathrm{V}]$ is:

$$
[\mathbf{C}_\mathrm{V}] = \begin{bmatrix}
2C_{\mathrm{su},2} & 0 & -C_{\mathrm{su},2} & 0 & -C_{\mathrm{su},2} & 0 & 0 & 0 & 0 & 0 \\
 & 2L_2^2C_{\mathrm{su},2} & -L_2C_{\mathrm{su},2} & 0 & L_2C_{\mathrm{su},2} & 0 & 0 & 0 & 0 & 0 \\
 & & 2C_{\mathrm{su},1}+C_{\mathrm{su},2} & 0 & 0 & 0 & -C_{\mathrm{su},1} & -C_{\mathrm{su},1} & 0 & 0 \\
 & & & 2L_1^2C_{\mathrm{su},1} & 0 & 0 & -C_{\mathrm{su},1}L_1 & C_{\mathrm{su},1}L_1 & 0 & 0 \\
 & & & & 2C_{\mathrm{su},1}+C_{\mathrm{su},2} & 0 & 0 & 0 & -C_{\mathrm{su},1} & -C_{\mathrm{su},1} \\
 & & & & & 2L_1^2C_{\mathrm{su},1} & 0 & 0 & -C_{\mathrm{su},1}L_1 & C_{\mathrm{su},1}L_1 \\
 & & & Symm & & & C_{\mathrm{su},1} & 0 & 0 & 0 \\
 & & & & & & & C_{\mathrm{su},1} & 0 & 0 \\
 & & & & & & & & C_{\mathrm{su},1} & 0 \\
 & & & & & & & & & C_{\mathrm{su},1}
\end{bmatrix} \tag{3.27}
$$

and the mass matrix $[\mathbf{M}_\mathrm{V}]$ is:

$$
[\mathbf{M}_\mathrm{V}] = diag\left[M_\mathrm{c} \quad J_\mathrm{c} \quad M_{\mathrm{t},1} \quad J_{\mathrm{t},1} \quad M_{\mathrm{t},2} \quad J_{\mathrm{t},2} \quad M_{\mathrm{w},1} \quad M_{\mathrm{w},2} \quad M_{\mathrm{w},3} \quad M_{\mathrm{w},4}.\right] \tag{3.28}
$$

3.4 Comparison of moving vehicle models

In this section the previously described vehicle models are compared. The bridge is still modelled as a simply supported beam with parameters described in Subsection 2.3.1. In Subsection 3.4.1 the results of moving mass model and SDOF vehicle model are presented. Later, in Subsection 3.4.2 multiple SDOF vehicles model is compared with MDOF vehicle model. After, multiple SDOF vehicles and MDOF vehicle models are compared between each other once again but this time including vertical railway track irregularities, in Subsection 3.4.3. Finally, an overall review of the results is given in Subsection 3.4.4.

3.4.1 Moving mass model and single-degree-of-freedom model

In this subsection, specifications of moving mass and SDOF vehicle models are introduced. The effects that these models have on the behaviour of the bridge are presented and compared.

Moving mass model

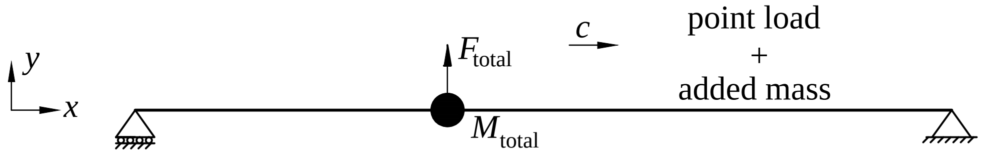

Figure 3.4: Moving mass model on a beam

In the moving mass model, a load acting on the bridge due to a vehicle is implemented as a single point load plus an added mass, cf. Figure 3.4. Added mass is taken as a point mass. The theory used is introduced in Section 3.1. Parameters for a moving mass model: vehicle mass $M_{\mathrm{bm}} = M_{\mathrm{total}} = 69200\mathrm{kg}$ and point load due to the vehicle $F_{\mathrm{w}} = F_{\mathrm{total}} = -680000\mathrm{N}$.

Single-degree-of-freedom model

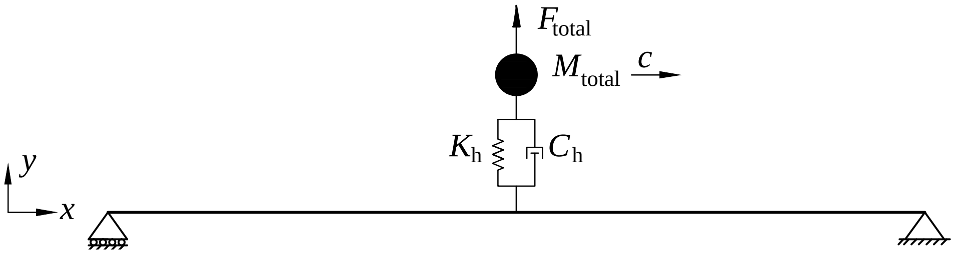

Figure 3.5: SDOF model on a beam

In this model a vehicle is implemented as an SDOF vehicle. The vehicle itself is modelled as a constant point load and an added mass. The difference from the previous model is that the coupling between bridge and a vehicle is introduced by a spring–dashpot system. A detailed illustration of the model presented in Figure 3.2 and the theory is given in Section 3.2. A simplified model is presented in Figure 3.5.

Parameters for an SDOF model are: circular eigenfrequency of the vehicle $\omega_{\mathrm{v}} = 4.4\mathrm{rad/s}$, damping ratio of the vehicle $\zeta_{\mathrm{v}} = 0.6$. Using these parameters the stiffness K_{h} and damping C_{h} of the SDOF vehicle are determined as:

$$K_{\mathrm{h}} = M_{\mathrm{h}}\,\omega_{\mathrm{v}}^2, \tag{3.29}$$

$$C_{\mathrm{h}} = 2\,\zeta_{\mathrm{v}}\,\sqrt{M_{\mathrm{h}}\,K_{\mathrm{h}}}. \tag{3.30}$$

The vehicle mass $M_{\mathrm{h}} = M_{\mathrm{total}}$ and a point load F_{w} due to the vehicle have the same magnitudes as in the moving mass model.

Deflections of the bridge, for both models at two different locomotive speeds of 47m/s and 69m/s, are presented in Figure 3.6 and Figure 3.7, respectively.

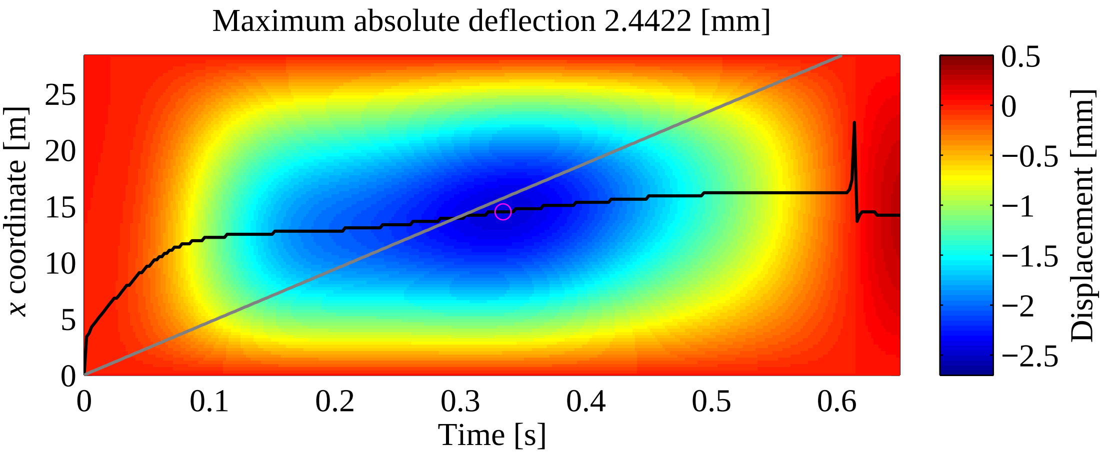

(a)

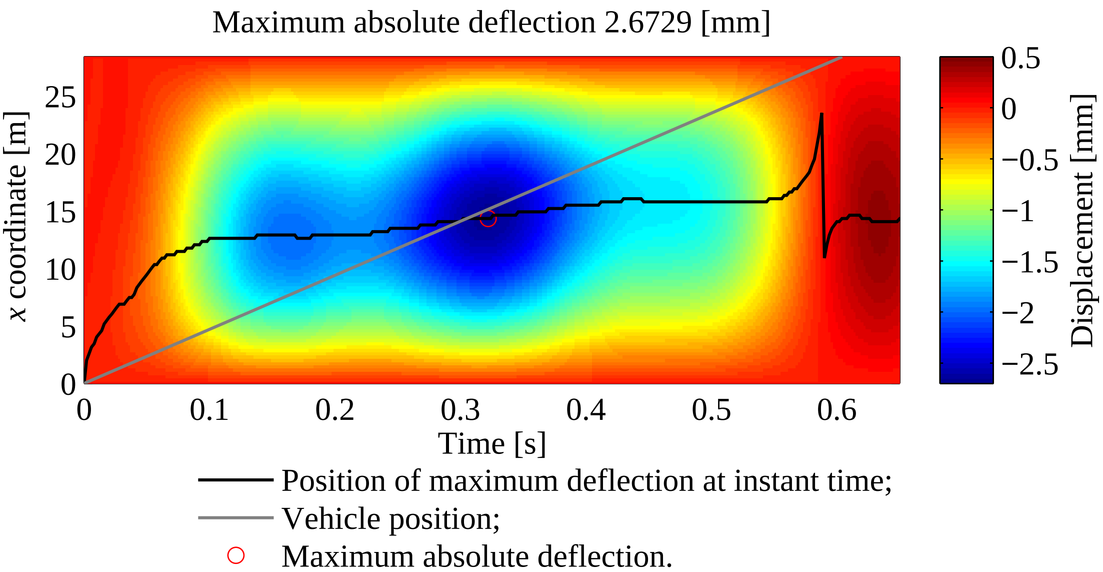

(b)

Figure 3.6: Deflection of a bridge at a vehicle speed of 47m/s. a) Moving mass model; b) Single-degree-of-freedom model

Regarding Figure 3.6, the behaviour of a bridge traversed by a vehicle varies significantly using these two models. In case of added point mass, the mass M_{total} dampens the bridge response and it mostly deflects in the first eigenmode. For SDOF vehicle model, the vibration of the mass M_{total} itself excites more eigenmodes of the bridge. Bigger maximum absolute deflection at a vehicle speed of 47m/s is observed for the SDOF vehicle model. The deflection difference between the two models is 8.63% of the maximum absolute deflection.

At a higher vehicle speed, 69m/s, the difference of the bridge deflection between two models decreases to 4% of the maximum absolute deflection, cf. Figure 3.7. Despite that, the overall behaviour is still considerably different.

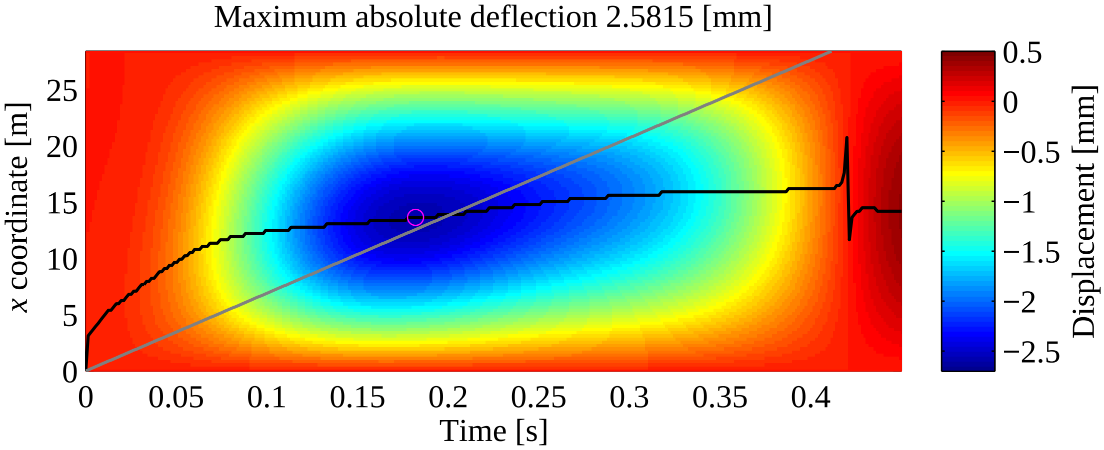

(a)

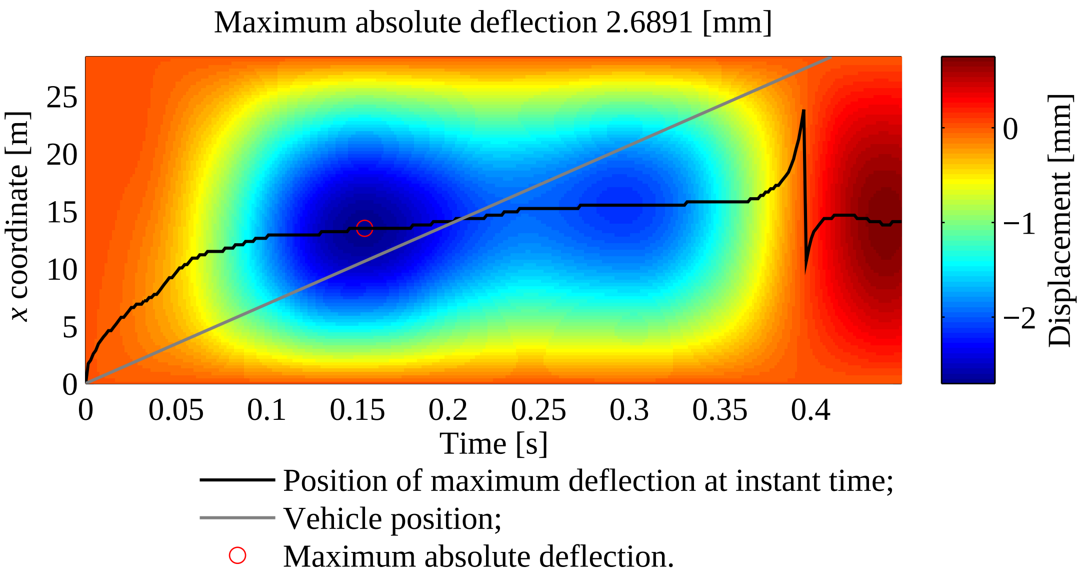

(b)

Figure 3.7: Deflection of a bridge at a vehicle speed of 69m/s. a) Moving mass model; b) Single-degree-of-freedom model

Comparing all four graphs it is noticeable that a moving mass model shows higher bridge deflection dependency on the vehicle speed than an SDOF model. Also the response of the bridge varies significantly between the two models. The SDOF vehicle model excites the bridge more, leaving the bridge to vibrate in the first eigenmode after the vehicle leaves, with a higher amplitude then with the added mass model. Compared to the three models shown in Subsection 2.3.3 it can be seen that masses added either by point mass or SDOF vehicle, dampens the response of the bridge, thus making the vibrations less intense.

3.4.2 Multiple SDOF vehicles model and MDOF vehicle model

The main idea of this chapter is to introduce a contact point for every wheel set of the locomotive. Thus, more reliable results can be obtained than by using just one contact point as it was done in previous models. In this section, differences of the bridge deflection are described when a vehicle is introduced as an multiple SDOF systems or a multi-degree-of-freedom system. Before introducing results, a short description of both models including exact parameters and graphic illustrations are given.

Multiple single-degree-of-freedom vehicles model

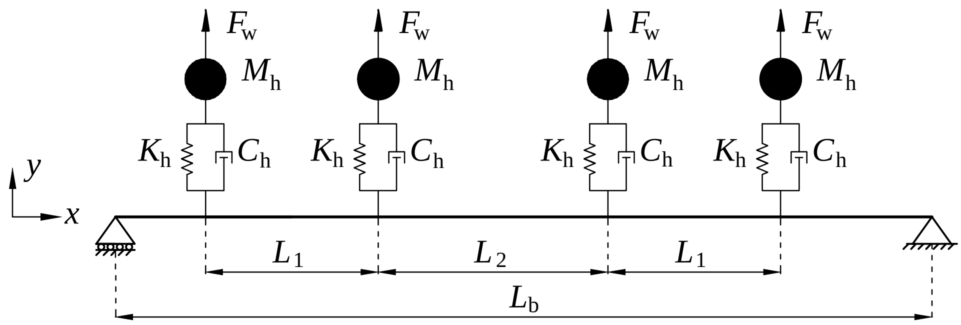

Figure 3.8: Multiple SDOF vehicles on a beam

The multiple SDOF vehicle model contains four separate, independent SDOF vehicles, cf. Figure 3.8. Each SDOF vehicle can have different mass and can be affected by different forces. In this case, every vehicle is assigned one quarter of the total mass $M_\mathrm{h} = \frac{1}{4}M_\mathrm{total}$ of the vehicle and a quarter of the total force $F_\mathrm{w} = \frac{1}{4}F_\mathrm{total}$. Theory for the SDOF system is given in Section 3.2. Parameters for an multiple SDOF vehicles model are given in Table 3.1.

Distance between wheels axes in a bogie	L_1	3	m
Distance between inner wheels axes of locomotive	L_2	11	m
Part of the locomotive mass applied for one SDOF system	M_h	17300	kg
Circular eigenfrequency of the vehicle	ω_v	4.4	rad/s
Damping ratio of the vehicle	ζ_v	0.6	-

Table 3.1: Parameters for multiple SDOF vehicles model

Multi-degree-of-freedom vehicle model

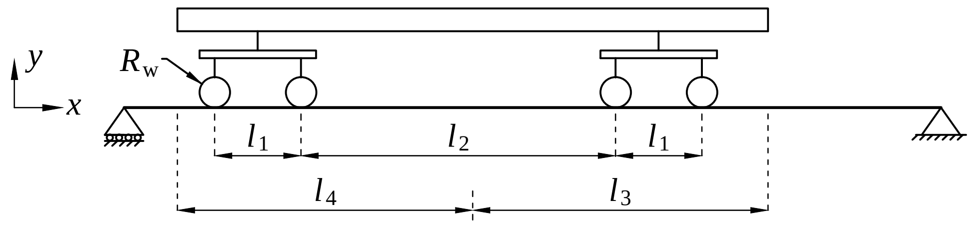

Figure 3.9: MDOF vehicle model on a beam

MDOF vehicle is modelled with two layers of a spring–dashpot systems, in which vertical and pitch motion for vehicle itself and bogies are involved. The vehicle model is based on a TGV locomotive (French high-speed train), cf. Lei [10]. Figure 3.3 illustrates in details a 10-degrees-of-freedom system, while a simplified model illustration is presented in Figure 3.9. Coupling the vehicle system and a railway track is done through spring–dashpot systems. Parameters for the MDOF vehicle model are listed in Table 3.2 and illustrated in Figure 3.3.

Distance between wheels axes in a bogie	l_1	3	m
Distance between inner wheels axes of locomotive	l_2	11	m
Distance from the centre axis to the front of a vehicle body	l_3	12.02	m
Distance from a centre axis to the end of a vehicle body	l_4	10.14	m
Mass of a car body	M_c	53500	kg
Pitch moment of inertia for car body	J_c	$2.24 \cdot 10^6$	m^4
Secondary suspension stiffness	$K_{su,2}$	1.31	MN/m
Secondary suspension damping	$C_{su,2}$	30	kN·s/m
Mass of bogie	M_t	3260	kg
Pitch moment of inertia for bogie	J_t	$2.45 \cdot 10^3$	m^4
Primary suspension stiffness	$K_{su,1}$	3.28	MN/m
Primary suspension damping	$C_{su,1}$	90	kN·s/m
Mass of wheel set	M_w	2000	kg
Radius of a wheel	R_w	0.458	m
Rigidity of a wheel	K_w	18	GN/m
Damping of a wheel	C_w	18	kN·s/m

Table 3.2: Parameters for MDOF vehicle model

Deflections of the bridge at two different vehicle speeds, 47m/s and 69m/s, for both, multiple SDOF vehicles and MDOF vehicle models, are presented in Figure 3.10 and Figure 3.11, respectively.

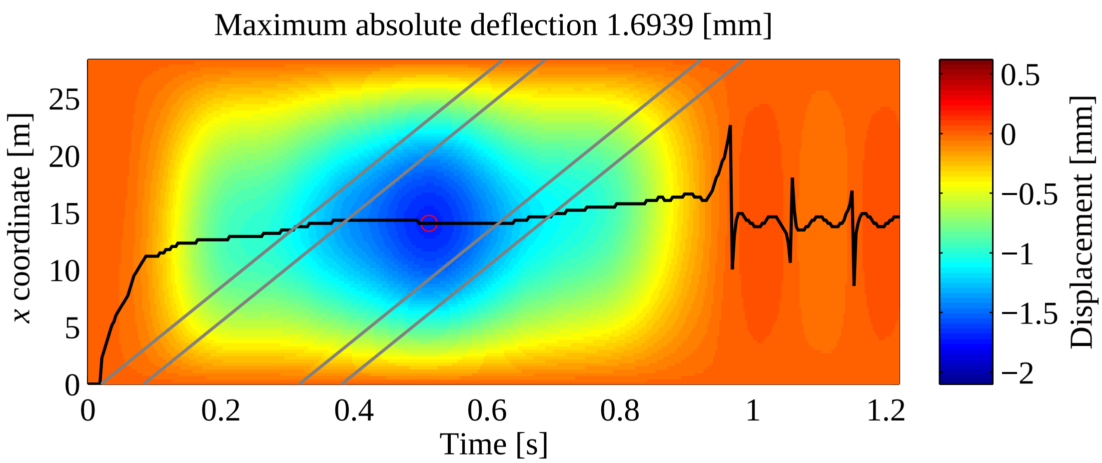

(a)

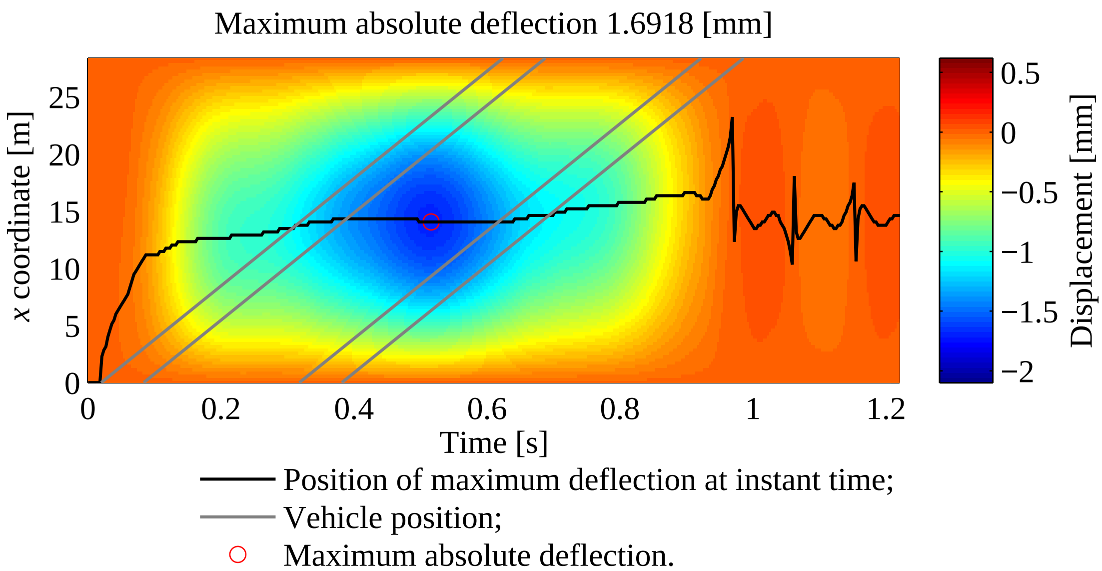

(b)

Figure 3.10: Deflection of a bridge at vehicle speed 47m/s. a) Multiple single-degree-of-freedom vehicles model; b) Multi-degree-of-freedom vehicle model

According to Figure 3.10 bigger deflection of the bridge is induced by multiple single-degree-of-freedom vehices model. However, maximum difference of the bridge deflection between multiple SDOF and MDOF models at a vehicle speed 47m/s is just 0.12% of the maximum absolute deflection. Thus, the difference is considered negligible. As it was expected the biggest deflection can be seen at the mid-span of the bridge.

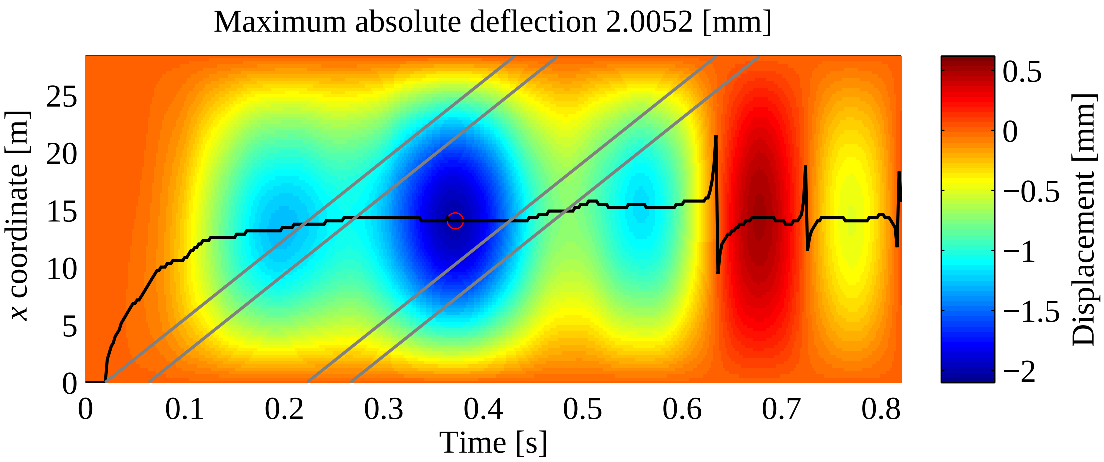

(a)

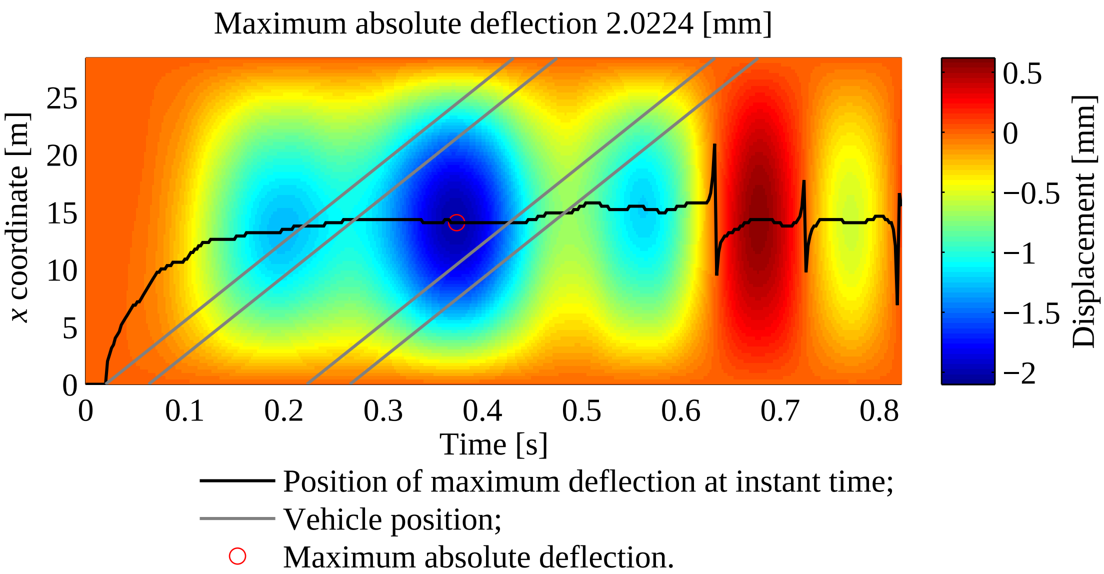

(b)

Figure 3.11: Deflection of a bridge at vehicle speed 69m/s. a) Multiple single-degree-of-freedom vehicles model; b) Multi-degree-of-freedom vehicle model

As it can be seen in Figure 3.11, at a vehicle speed 69m/s, bigger deflection of the bridge appears in the MDOF vehicle model this time. As in the previous case the difference is very small, just 0.85% of the maximum absolute bridge deflection. Therefore, it is again considered too small to show any significant differences between the two models.

In general, results provided by the two models described in this section are extremely similar. The general tendency of increasing bridge deflection due to increasing vehicle speed is noticed for both models. Compared to previous sections, where only one load was introduced, behaviour of the bridge and maximum absolute deflections are very different. Thus, the effects of force distribution between wheel sets should always be introduced.

3.4.3 Multiple SDOF vehicles and MDOF models including railway track irregularities

To model accurately the effects of a passing vehicle, track irregularities have to be introduced since they induce additional high frequency vibrations to the structure. In this section, two different profiles for vertical track unevenness are presented. Later, bridge deflections obtained using multiple SDOF vehicles and MDOF models are compared once again but this time including track irregularities. At the end, a small study of locomotive wheel acceleration due to railway track irregularities is given.

Railway track unevenness

The theory covering railway track unevenness is given in Appendix A. Two different vertical track profiles illustrating track unevenness are presented in Figure 3.12. These two different vertical track unevenness profiles, Profile A and Profile B, are used in this section further at bridge deflection comparison and wheel acceleration analysis.

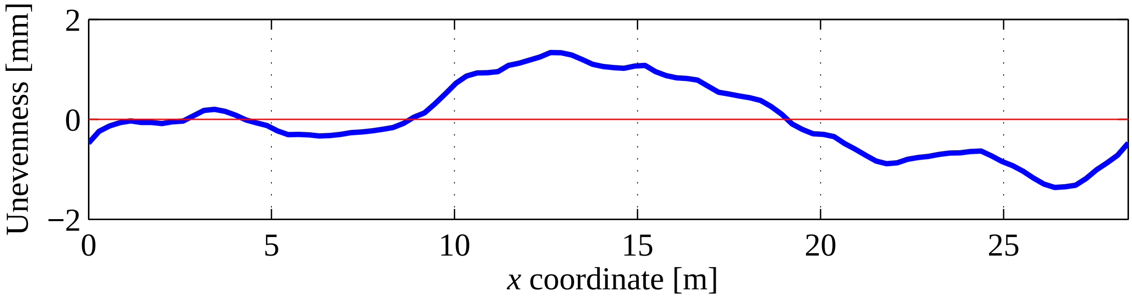

(a)

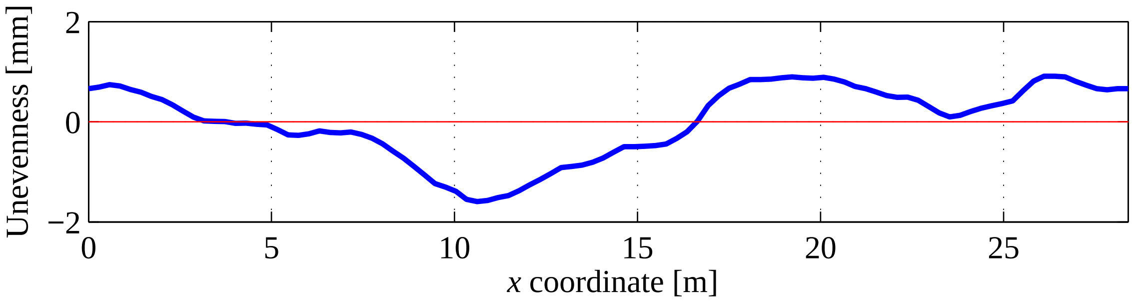

(b)

Figure 3.12: Vertical track unevenness: a) Profile A; b) Profile B

Bridge deflection comparison between multiple SDOF vehicles and MDOF models including track irregularities

Bridge deflections are determined using the same multiple SDOF vehicles and MDOF models as they are represented at Subsection 3.4.2. Track irregularities are implemented in both models. This time, bridge deflection is compared according to two different vertical track unevenness profiles at a constant vehicle speed 69m/s. A particular speed of 69m/s is chosen (not 47m/s) because higher speeds cause bigger forces induced by track unevenness.

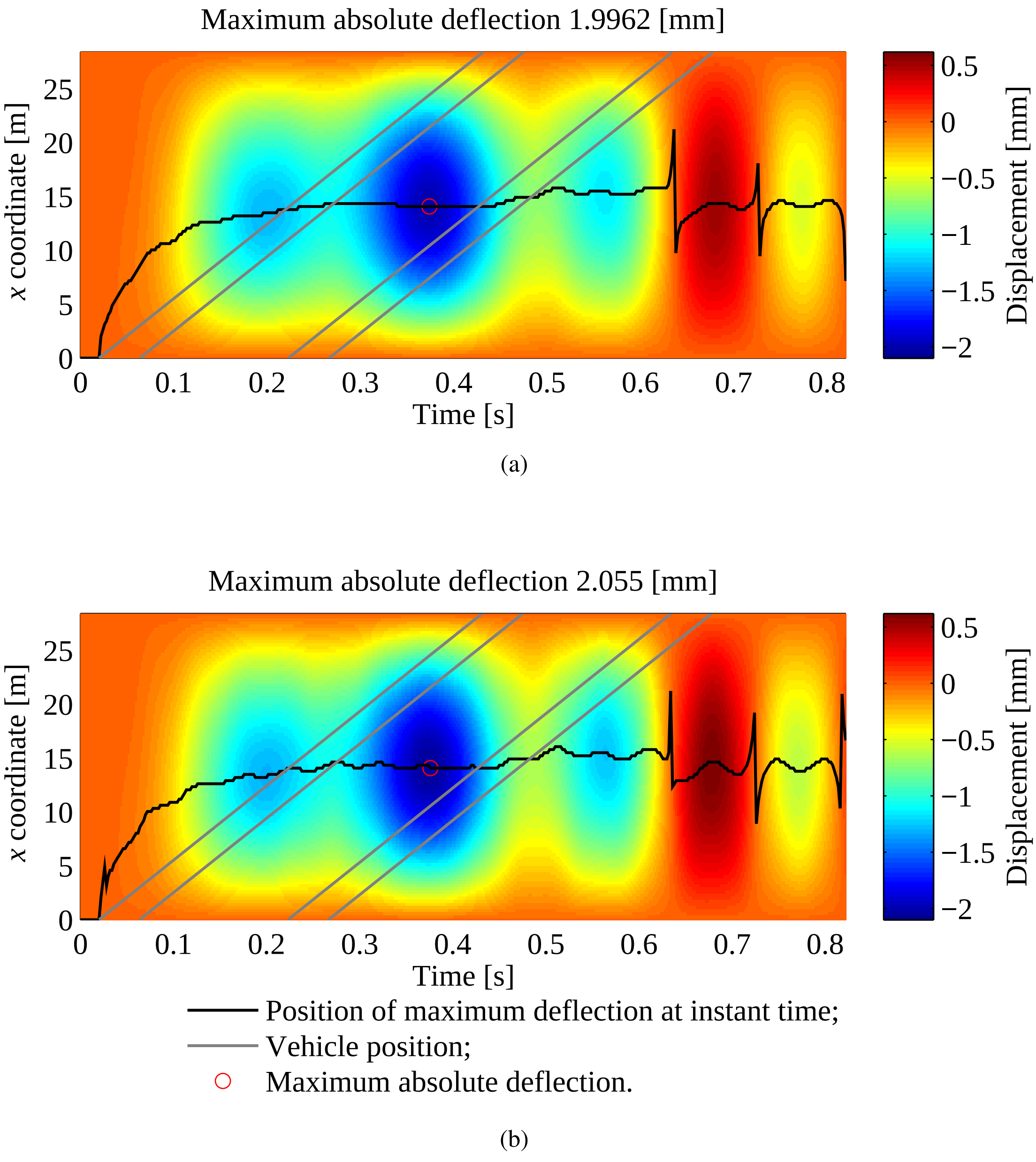

Figure 3.13: Deflection of a bridge at a vehicle speed 69m/s, vertical track unevenness Profile A. a) Multiple single-degree-of-freedom vehicles model; b) Multi-degree-of-freedom model

Regarding Figure 3.13, bigger bridge deflection is obtained for the MDOF model at a vehicle speed of 69m/s using unevenness Profile A. However, the difference of the bridge deflection obtained from the two models is small, 2.9% of the maximum absolute deflection.

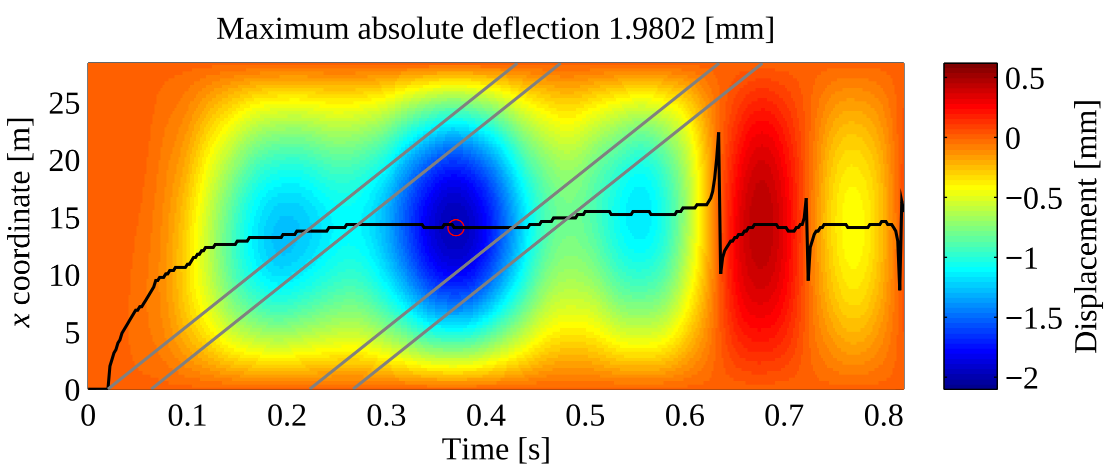

(a)

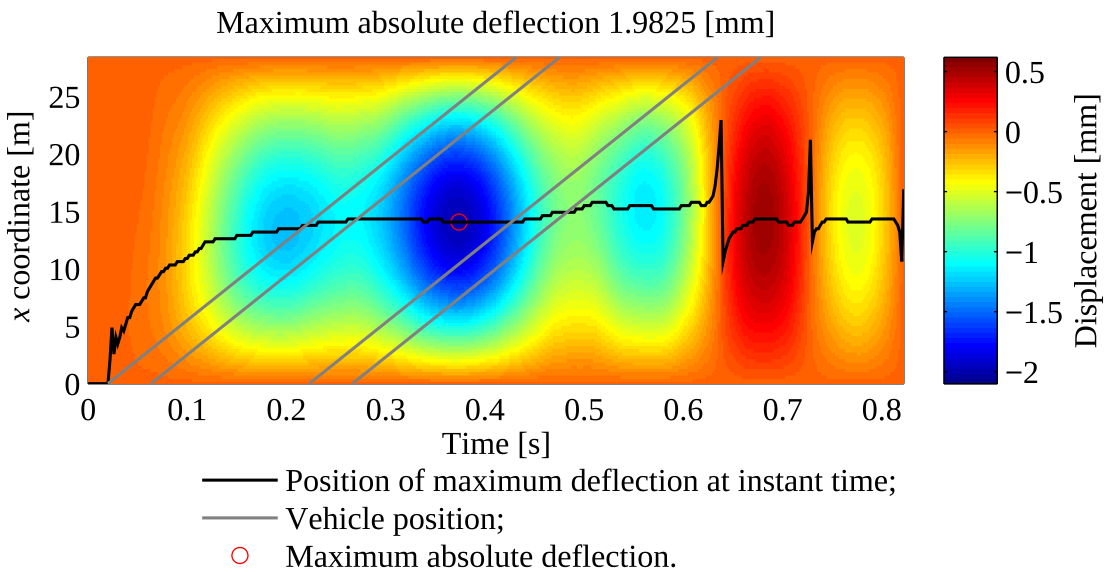

(b)

Figure 3.14: Deflection of a bridge at a vehicle speed 69m/s, vertical track unevenness Profile B. a) Multiple single-degree-of-freedom vehicles model; b) Multi-degree-of-freedom model

For Profile B, see Figure 3.14, bigger bridge deflection is obtained with the MDOF model. The difference is just 0.11% of the maximum absolute deflection between two models.

Comparing multiple SDOF vehicles model and MDOF vehicle model, it can be seen that track irregularities are more noticeable for the MDOF model. This is caused by accelerating the wheel set, which has relatively small mass and high stiffness thus, it induces significant forces in the system.

In general, it can be seen that while track unevenness does have some effect on the behaviour of the beam, the overall effect is not very high. Due to relatively big bridge mass compared to that of a wheel set, the high frequency vibrations of the wheels do not cause big beam displacements. Further, locomotive wheel set acceleration analysis is done.

Locomotive wheel acceleration due to vertical track unevenness

A small study regarding variation of the wheel accelerations due to vertical track irregularities is performed. For comparison three different cases are considered: track without irregularities, track with vertical unevenness defined by Profile A and track with vertical unevenness defined by Profile B. The results are determined using MDOF model at a vehicle speed 69m/s for all three cases.

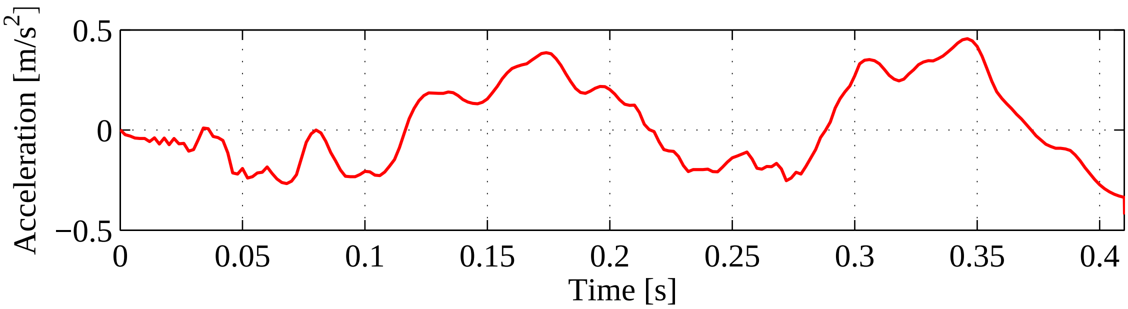

(a)

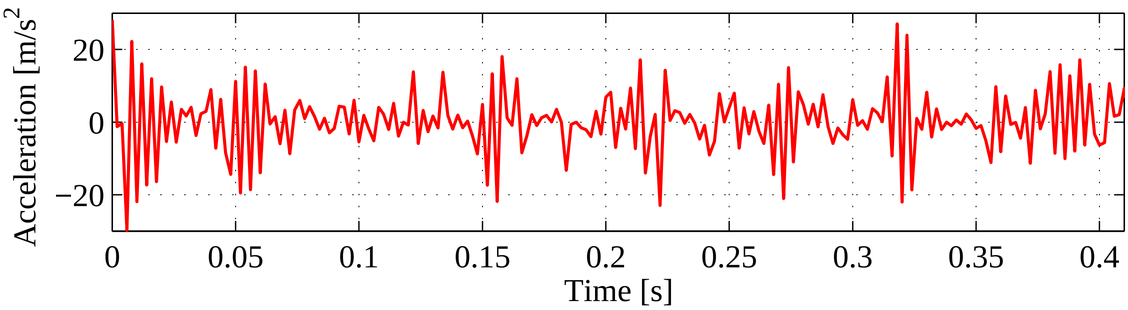

(b)

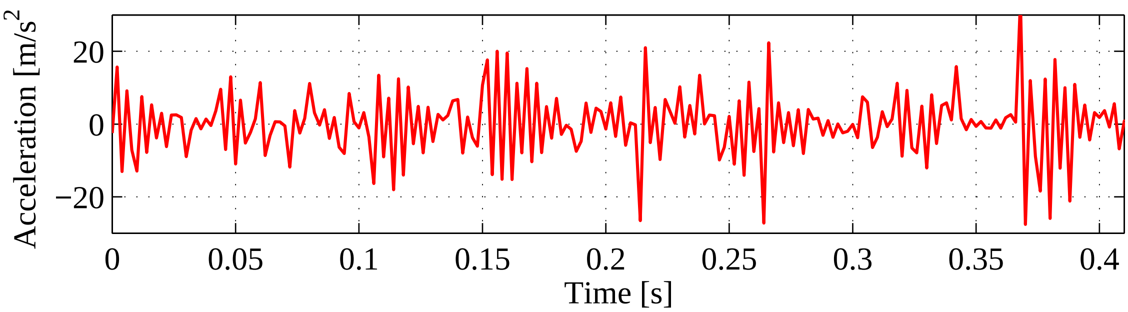

(c)

Figure 3.15: Acceleration of a locomotive wheel at speed 69m/s, regarding track irregularities. a) No vertical track unevenness added; b) Vertical track unevenness defined by Profile A; c) Vertical track unevenness defined by Profile B

In Figure 3.15, the maximum absolute locomotive wheel acceleration increases up to 60 times introducing track irregularities with Profile A and up to 68 times with Profile B. Thus, it is clear that vertical track unevenness has a significant influence on the behaviour of the vehicle. The forces caused by wheel accelerations are mostly noticeable in the bogies of the vehicle, while the effect on the bridge is small because of the relatively small mass of the wheel sets compared to the bridge itself.

Previously it was found out that bigger bridge deflection is determined using Profile A because it contains higher amplitude irregularities. However, higher wheel accelerations are obtained using Profile B. It is because at Profile B irregularities change more drastically, i.e. increases and decrease with steeper slopes, cf. Figure 3.12.

3.4.4 Review of the results

The effects of added mass from the locomotive itself are analysed. Introducing the mass as a point mass or through a spring–dashpot system, in SDOF vehicle model, shows a considerable difference in the obtained results. Since a real locomotive does not act only at one point, four contact points are introduced to have a more realistic model. This is done in two different ways, one by introducing four SDOF vehicles, second by introducing an MDOF vehicle which models the real locomotive suspension system. The obtained results from a multiple SDOF vehicles model and MDOF vehicle model are similar. However, a big difference can be seen comparing the results from single contact point and four contact points models. In the real world railway tracks have a certain degree of a vertical irregularities, which, in the thesis, are introduced for multiple SDOF vehicles and MDOF vehicle models. The track unevenness causes significant vibrations in the vehicle bogies but the effects on the bridge are small.

It can be concluded that MDOF vehicle model is the most realistic way to model the locomotive, as it accounts for train mass, multiple contact points and reflects the effects of track unevenness most accurate.

Chapter 4
Finite element method in three dimensions

The FEM in three dimensions is used to create the final computational model used in this thesis. Firstly, in this chapter, general formulation of three-dimensional beam element is introduced in Section 4.1, together with transformation between the local and the global coordinate systems in Subsection 4.1.1. Based on the three-dimensional beam element the more advanced computational model, including multiple phenomena is created. It is described in the paper "Numerical modelling of dynamic response of high-speed railway bridges considering vehicle–structure and structure–soil–structure interaction" presented in the Appendix A. Here, in section Section 4.2, only a brief introduction to the final computational model is given together with some results.

4.1 General formulation

For the three-dimensional (3-D) analysis, 3-D beam elements with six degrees of freedom (three translation components along the x, y, z-axis and three rotational components around these axes) at each node are used, as shown in Figure 4.1.

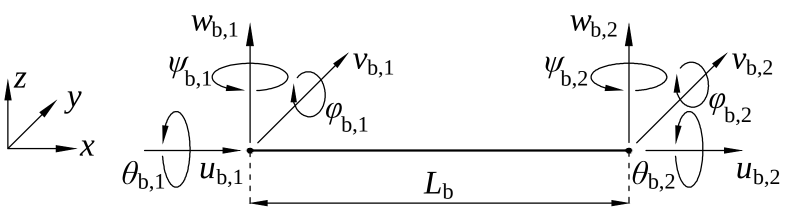

Figure 4.1: Beam element with six degrees of freedom at each node

The following assumptions are used for finite element matrix derivations:

- Small deformations (axial deformation, bending and twist can be decoupled and looked at separately);
- Euler-Bernoulli beam theory for bending (plane sections normal to the beam axis remain plane and normal to the beam axis during the deformation);
- Twist is considered free (Saint-Venant torsion).

For axial deformation in the x direction the partial differential equation is:

$$E_\mathrm{b}A_\mathrm{b}\frac{\partial^2 u_\mathrm{b}(x,t)}{\partial x^2} - \rho_\mathrm{b}A_\mathrm{b}\frac{\partial^2 u_\mathrm{b}(x,t)}{\partial t^2} = -q_x, \tag{4.1}$$

where q_x is the axial force. Bending in the x,z-plane is based on Euler-Bernoulli theory:

$$\rho_\mathrm{b}A_\mathrm{b}\frac{\partial^2 w_\mathrm{b}(x,t)}{\partial t^2} + E_\mathrm{b}I_{\mathrm{b},y}\frac{\partial^4 w_\mathrm{b}(x,t)}{\partial x^4} = q_z, \tag{4.2}$$

where q_z is the external force in z direction. Similarly, for bending in the x,y-plane:

$$\rho_\mathrm{b}A_\mathrm{b}\frac{\partial^2 v_\mathrm{b}(x,t)}{\partial t^2} + E_\mathrm{b}I_{\mathrm{b},z}\frac{\partial^4 v_\mathrm{b}(x,t)}{\partial x^4} = q_y, \tag{4.3}$$

where q_y is the external force in the y direction. Finally, torsion around the x-axis is governed by:

$$G_\mathrm{b}T_\mathrm{b}\frac{\partial^2 \theta_\mathrm{b}(x,t)}{\partial x^2} - \rho_\mathrm{b}I_{\mathrm{b},0}\frac{\partial^2 \theta_\mathrm{b}(x,t)}{\partial t^2} = -m_x, \tag{4.4}$$

where m_x is the external moment around the x-axis.

The finite element matrices are formed by combining the axial deformation (degrees of freedom $u_{\mathrm{b},1}$, $u_{\mathrm{b},2}$), the bending problem in the x,z-plane (degrees of freedom $w_{\mathrm{b},1}$, $\psi_{\mathrm{b},1}$, $w_{\mathrm{b},2}$, $\psi_{\mathrm{b},2}$), the bending problem in the x,y-plane (degrees of freedom $v_{\mathrm{b},1}$, $\varphi_{\mathrm{b},1}$, $v_{\mathrm{b},2}$, $\varphi_{\mathrm{b},2}$) and torsion around the x-axis ($\theta_{\mathrm{b},1}$, $\theta_{\mathrm{b},2}$). The finite element formulation is written as:

$$[\mathbf{M}_\mathrm{B}]\{\ddot{\mathbf{d}}_\mathrm{B}(t)\} + [\mathbf{C}_\mathrm{B}]\{\dot{\mathbf{d}}_\mathrm{B}(t)\} + [\mathbf{K}_\mathrm{B}]\{\mathbf{d}_\mathrm{B}(t)\} = \{\mathbf{f}_\mathrm{B}(t)\}, \tag{4.5}$$

where $\{\ddot{\mathbf{d}}_\mathrm{B}(t)\}$ and $\{\dot{\mathbf{d}}_\mathrm{B}(t)\}$ are the acceleration vector and the velocity vector, respectively.

The nodal displacement vector $\{\mathbf{d}_\mathrm{B}(t)\}$ is:

$$\{\mathbf{d}_\mathrm{B}(t)\} = \begin{Bmatrix} u_{\mathrm{b},1}(t) & \text{translation in the } x \text{ direction at 1st node;} \\ v_{\mathrm{b},1}(t) & \text{translation in the } y \text{ direction at 1st node;} \\ w_{\mathrm{b},1}(t) & \text{translation in the } z \text{ direction at 1st node;} \\ \theta_{\mathrm{b},1}(t) & \text{rotation around the } x\text{-axis at 1st node;} \\ \varphi_{\mathrm{b},1}(t) & \text{rotation around the } y\text{-axis at 1st node;} \\ \psi_{\mathrm{b},1}(t) & \text{rotation around the } z\text{-axis at 1st node;} \\ u_{\mathrm{b},2}(t) & \text{translation in the } x \text{ direction at 2nd node;} \\ v_{\mathrm{b},2}(t) & \text{translation in the } y \text{ direction at 2nd node;} \\ w_{\mathrm{b},2}(t) & \text{translation in the } z \text{ direction at 2nd node;} \\ \theta_{\mathrm{b},2}(t) & \text{rotation around the } x\text{-axis at 2nd node;} \\ \varphi_{\mathrm{b},2}(t) & \text{rotation around the } y\text{-axis at 2nd node;} \\ \psi_{\mathrm{b},2}(t) & \text{rotation around the } z\text{-axis at 2nd node.} \end{Bmatrix} \tag{4.6}$$

The governing equations for the structure are all discretized, using the standard Galerkin approach. For axial deformation linear shape functions are used:

$$\{\check{\Phi}_\mathrm{a}(x)\}^T = \begin{Bmatrix} 1-\frac{x}{L_\mathrm{b}} & \text{due to unit translation in the } x \text{ direction at 1st node;} \\ \frac{x}{L_\mathrm{b}} & \text{due to unit translation in the } x \text{ direction at 2nd node.} \end{Bmatrix} \tag{4.7}$$

For bending in the x,z-plane cubic shape functions are used:

$$\{\check{\Phi}_{\mathrm{b},z}(x)\}^T = \begin{Bmatrix} 1-\frac{3x^2}{L_\mathrm{b}^2}+\frac{2x^3}{L_\mathrm{b}^3} \\ x\Big(-1+\frac{2x}{L_\mathrm{b}}-\frac{x^2}{L_\mathrm{b}^2}\Big) \\ \frac{x^2}{L_\mathrm{b}^2}\Big(3-\frac{2x}{L_\mathrm{b}}\Big) \\ \frac{x^2}{L_\mathrm{b}}\Big(1-\frac{x}{L_\mathrm{b}}\Big) \end{Bmatrix} \begin{array}{l} \text{due to unit translation in the } z \text{ direction at 1st node;} \\ \text{due to unit rotation around the } y\text{-axis at 1st node;} \\ \text{due to unit translation in the } z \text{ direction at 2nd node;} \\ \text{due to unit rotation around the } y\text{-axis at 2nd node.} \end{array} \tag{4.8}$$

Similarly, for bending in the x,y-plane cubic shape functions are used:

$$\{\check{\Phi}_{\mathrm{b},y}(x)\}^T = \begin{Bmatrix} 1-\frac{3x^2}{L_\mathrm{b}^2}+\frac{2x^3}{L_\mathrm{b}^3} \\ -x\Big(-1+\frac{2x}{L_\mathrm{b}}-\frac{x^2}{L_\mathrm{b}^2}\Big) \\ \frac{x^2}{L_\mathrm{b}^2}\Big(3-\frac{2x}{L_\mathrm{b}}\Big) \\ -\frac{x^2}{L_\mathrm{b}}\Big(1-\frac{x}{L_\mathrm{b}}\Big) \end{Bmatrix} \begin{array}{l} \text{due to unit translation in the } y \text{ direction at 1st node;} \\ \text{due to unit rotation around the } z\text{-axis at 1st node;} \\ \text{due to unit translation in the } y \text{ direction at 2nd node;} \\ \text{due to unit rotation around the } z\text{-axis at 2nd node.} \end{array} \tag{4.9}$$

For torsion around the x-axis linear shape functions are used:

$$\{\check{\Phi}_\mathrm{t}(x)\}^T = \begin{Bmatrix} 1-\frac{x}{L_\mathrm{b}} \\ \frac{x}{L_\mathrm{b}} \end{Bmatrix} \begin{array}{l} \text{due to unit rotation around the } x\text{-axis at 1st node;} \\ \text{due to unit rotation around the } x\text{-axis at 2nd node.} \end{array} \tag{4.10}$$

Differentiating and integrating the shape functions shown above, the three-dimensional elastic stiffness matrix $[\mathbf{K}_\mathrm{B}]$ for a 3-D beam elements is obtained:

$$
[\mathbf{K}_\mathrm{B}] = \begin{bmatrix}
\frac{E_\mathrm{b}A_\mathrm{b}}{L_\mathrm{b}} & 0 & 0 & 0 & 0 & 0 & -\frac{E_\mathrm{b}A_\mathrm{b}}{L_\mathrm{b}} & 0 & 0 & 0 & 0 & 0 \\
 & \frac{12E_\mathrm{b}I_{\mathrm{b},z}}{L_\mathrm{b}^3} & 0 & 0 & 0 & \frac{6E_\mathrm{b}I_{\mathrm{b},z}}{L_\mathrm{b}^2} & 0 & -\frac{12E_\mathrm{b}I_{\mathrm{b},z}}{L_\mathrm{b}^3} & 0 & 0 & 0 & \frac{6E_\mathrm{b}I_{\mathrm{b},z}}{L_\mathrm{b}^2} \\
 & & \frac{12E_\mathrm{b}I_{\mathrm{b},y}}{L_\mathrm{b}^3} & 0 & -\frac{6E_\mathrm{b}I_{\mathrm{b},y}}{L_\mathrm{b}^2} & 0 & 0 & 0 & -\frac{12E_\mathrm{b}I_{\mathrm{b},y}}{L_\mathrm{b}^3} & 0 & -\frac{6E_\mathrm{b}I_{\mathrm{b},y}}{L_\mathrm{b}^2} & 0 \\
 & & & \frac{G_\mathrm{b}T_\mathrm{b}}{L_\mathrm{b}} & 0 & 0 & 0 & 0 & 0 & -\frac{G_\mathrm{b}T_\mathrm{b}}{L_\mathrm{b}} & 0 & 0 \\
 & & & & \frac{4E_\mathrm{b}I_{\mathrm{b},y}}{L_\mathrm{b}} & 0 & 0 & 0 & \frac{6E_\mathrm{b}I_{\mathrm{b},y}}{L_\mathrm{b}^2} & 0 & \frac{2E_\mathrm{b}I_{\mathrm{b},y}}{L_\mathrm{b}} & 0 \\
 & & & & & \frac{4E_\mathrm{b}I_{\mathrm{b},z}}{L_\mathrm{b}} & 0 & -\frac{6E_\mathrm{b}I_{\mathrm{b},z}}{L_\mathrm{b}^2} & 0 & 0 & 0 & \frac{2E_\mathrm{b}I_{\mathrm{b},z}}{L_\mathrm{b}} \\
 & & & & & & \frac{E_\mathrm{b}A_\mathrm{b}}{L_\mathrm{b}} & 0 & 0 & 0 & 0 & 0 \\
 & & & & & & & \frac{12E_\mathrm{b}I_{\mathrm{b},z}}{L_\mathrm{b}^3} & 0 & 0 & 0 & -\frac{6E_\mathrm{b}I_{\mathrm{b},z}}{L_\mathrm{b}^2} \\
 & & & \textit{Symm} & & & & & \frac{12E_\mathrm{b}I_{\mathrm{b},y}}{L_\mathrm{b}^3} & 0 & \frac{6E_\mathrm{b}I_{\mathrm{b},y}}{L_\mathrm{b}^2} & 0 \\
 & & & & & & & & & \frac{G_\mathrm{b}T_\mathrm{b}}{L_\mathrm{b}} & 0 & 0 \\
 & & & & & & & & & & \frac{4E_\mathrm{b}I_{\mathrm{b},y}}{L_\mathrm{b}} & 0 \\
 & & & & & & & & & & & \frac{4E_\mathrm{b}I_{\mathrm{b},z}}{L_\mathrm{b}}
\end{bmatrix} \tag{4.11}
$$

where the element is described by: element length L_b, cross-sectional area A_b, Young's modulus E_b, shear modulus G_b, cross-sectional moment of inertia with respect to the y-axis $I_{\mathrm{b},y}$, cross-sectional moment of inertia with respect to the z-axis $I_{\mathrm{b},z}$, torsional constant T_b.

The consistent mass matrix $[\mathbf{M}_\mathrm{B}]$ for a 3-D beam element is determined in the same manner as the stiffness matrix:

$$
[\mathbf{M}_\mathrm{B}] = \frac{\rho_\mathrm{b}A_\mathrm{b}L_\mathrm{b}}{420} \begin{bmatrix}
140 & 0 & 0 & 0 & 0 & 0 & 70 & 0 & 0 & 0 & 0 & 0 \\
 & 156 & 0 & 0 & 0 & 22L_\mathrm{b} & 0 & 54 & 0 & 0 & 0 & -13L_\mathrm{b} \\
 & & 156 & 0 & -22L_\mathrm{b} & 0 & 0 & 0 & 54 & 0 & 13L_\mathrm{b} & 0 \\
 & & & \frac{140I_{\mathrm{b},0}}{A_\mathrm{b}} & 0 & 0 & 0 & 0 & 0 & \frac{70I_{\mathrm{b},0}}{A_\mathrm{b}} & 0 & 0 \\
 & & & & 4L_\mathrm{b}^2 & 0 & 0 & 0 & -13L_\mathrm{b} & 0 & -3L_\mathrm{b}^2 & 0 \\
 & & & & & 4L_\mathrm{b}^2 & 0 & 13L_\mathrm{b} & 0 & 0 & 0 & -3L_\mathrm{b}^2 \\
 & & & & & & 140 & 0 & 0 & 0 & 0 & 0 \\
 & & & & & & & 156 & 0 & 0 & 0 & -22L_\mathrm{b} \\
 & & & \textit{Symm} & & & & & 156 & 0 & 22L_\mathrm{b} & 0 \\
 & & & & & & & & & \frac{140I_{\mathrm{b},0}}{A_\mathrm{b}} & 0 & 0 \\
 & & & & & & & & & & 4L_\mathrm{b}^2 & 0 \\
 & & & & & & & & & & & 4L_\mathrm{b}^2
\end{bmatrix} \tag{4.12}
$$

where ρ_b is mass density and $I_{\mathrm{b},0}$ is polar moment of inertia of the cross-sectional area A_b. The damping matrix $[\mathbf{C}_\mathrm{B}]$ for a 3-D beam element is determined by Rayleigh damping.

4.1.1 Transformation of coordinates

This section is based on Paz [11]. The beam element discussed in Section 4.1 is located along the x-axis. Elements may have any orientation in space. The stiffness matrix and mass matrix given by Equation 4.11 and Equation 4.12, respectively, refer to local coordinates system (x, y, z directions) which are arbitrarily orientated in the global coordinates system (X, Y, Z directions). Elements which correspond to the same nodal coordinates should be added together. This is done in the same reference system, i.e. global coordinates system.

In Figure 4.2 the vector $\{\mathbf{A}\}$ can represent any force and displacement at the nodal coordinates of the joints of the structure. The vector $\{\mathbf{A}\} = \{\mathrm{X_c} \quad \mathrm{Y_c} \quad \mathrm{Z_c}\}$ has his components along the global system of coordinates (X, Y, Z). Components of the same vector along the local system of coordinates (x, y, z) are obtained by projections along that axis of vector $\{\mathbf{A}\}$ components.

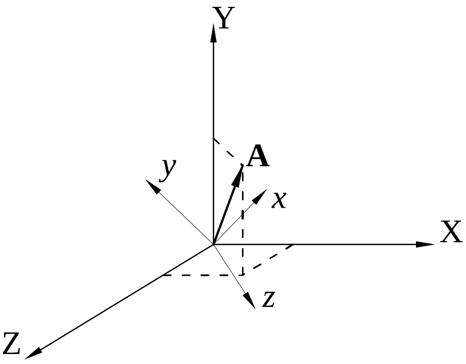

Figure 4.2: Components of a general vector $\{\mathbf{A}\}$ in local coordinates and global coordinates, [11]

In matrix notation the transformation is written as:

$$\begin{bmatrix} x_c \\ y_c \\ z_c \end{bmatrix} = \begin{bmatrix} \cos x\mathrm{X} & \cos x\mathrm{Y} & \cos x\mathrm{Z} \\ \cos y\mathrm{X} & \cos y\mathrm{Y} & \cos y\mathrm{Z} \\ \cos z\mathrm{X} & \cos z\mathrm{Y} & \cos z\mathrm{Z} \end{bmatrix} \begin{bmatrix} \mathrm{X_c} \\ \mathrm{Y_c} \\ \mathrm{Z_c} \end{bmatrix}, \tag{4.13}$$

where $\cos x\mathrm{Y}$ is defined as the angle between the local x-axis and the global Y-axis. The rest of the terms of the matrix are defined correspondingly. In order to calculate the direction cosines of the transformation matrix $[\mathbf{T}_1]$ it is sufficient to know the coordinates of the nodes of a beam element along the local x-axis and coordinates of a third point located in the x,y local plane (y is the principal axis of the cross-sectional area). From Equation 4.13 the transformation matrix is defined as:

$$[\mathbf{T}_1] = \begin{bmatrix} \cos x\mathrm{X} & \cos x\mathrm{Y} & \cos x\mathrm{Z} \\ \cos y\mathrm{X} & \cos y\mathrm{Y} & \cos y\mathrm{Z} \\ \cos z\mathrm{X} & \cos z\mathrm{Y} & \cos z\mathrm{Z} \end{bmatrix}. \tag{4.14}$$

For the 3-D beam element, the transformation of nodal displacement vectors involve the transformation of linear and angular displacement vectors at each joint of the segment. Therefore, for two joints there will be a transformation of a total of four displacements/rotations triplets.

The transformation matrix for 12 nodal degrees of freedom is given:

$$[\mathbf{T}] = \begin{bmatrix} [\mathbf{T}_1] & \mathbf{0} & \mathbf{0} & \mathbf{0} \\ \mathbf{0} & [\mathbf{T}_1] & \mathbf{0} & \mathbf{0} \\ \mathbf{0} & \mathbf{0} & [\mathbf{T}_1] & \mathbf{0} \\ \mathbf{0} & \mathbf{0} & \mathbf{0} & [\mathbf{T}_1] \end{bmatrix}. \tag{4.15}$$

The transformed stiffness matrix of the element $[\mathbf{K}_{\mathrm{BT}}]$ and the mass matrix $[\mathbf{M}_{\mathrm{BT}}]$ in reference to global coordinates are defined as follows:

$$[\mathbf{K}_{\mathrm{BT}}] = [\mathbf{T}]^T[\mathbf{K}_{\mathrm{B}}][\mathbf{T}], \tag{4.16a}$$
$$[\mathbf{M}_{\mathrm{BT}}] = [\mathbf{T}]^T[\mathbf{M}_{\mathrm{B}}][\mathbf{T}]. \tag{4.16b}$$

4.2 Description of computational model

Based on basic 3-D beam models described in Section 4.1 advanced computational model is implemented and described in paper “Numerical modelling of dynamic response of high-speed railway bridges considering vehicle–structure and structure–soil–structure interaction” presented in the Appendix A. A brief description of this model is given in this section.

The bridge structure is modelled in three dimensions using two-noded 3-D beam elements. The track structure is composed of three layers (rails, sleepers and deck components) connected by spring and dashpot systems (which model the rail-pads and ballast). The considered bridge has two railway tracks, but only one is modelled as a layered structure, while the second one is accounted for by point masses offset from the deck centre line. The bridge supports are modelled as 3-D two-noded beam elements with rigid surface footings, which rest on the subsoil. In order to model the dynamic soil behaviour, a semi-analytical approach is used, utilizing a solution for Green’s function in frequency wave-number domain, based on Andersen and Clausen [8]. Then coupled bridge–soil system is solved in frequency domain. The vehicle is modelled as a 2-D MDOF system, with two layers of spring-dashpot suspension system. The interaction between the wheels and the rail is modelled through non-linear Hertzian force. Due to this, an iterative time domain solution based on Newmark scheme is implemented. Since the bridge-soil system is solved in frequency domain and the vehicle in time domain, another iteration procedure is implemented for a simultaneous solution.

The geometry of the analysed bridge is shown in Figure 4.3. The bridge has a total length of 200m, which is subdivided into eight spans, each 25m long. Sleepers are spaced 0.6m apart. From each side of the bridge there is 25m of the track which is attached to a rigid surface. The bridge is supported by seven 6m tall pylons, each resting on a rigid surface footing. The material, cross-sectional and other properties can be found in Appendix A.

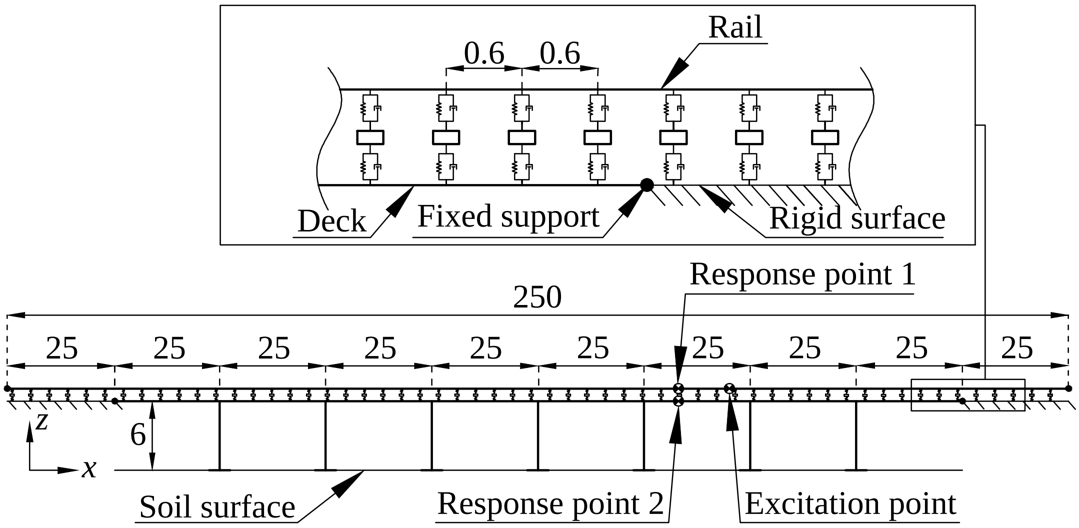

Figure 4.3: The bridge structure used in the computational model (measures in m)

4.3 Soil effects to the computational model

The results of the computational model are presented for four underlying soil cases as described bellow:

Case 0 : Bedrock, i.e. bridge supports are fixed,

Case 1 : Half-space of clay,

Case 2 : 5m of clay over half-space of sand,

Case 3 : 10m of clay over half-space of sand.

Properties for the underlying soil are presented in Appendix A. In this section only a brief review of the results is presented.

The excitation point is excited and the response of the structure is observed at response point 1 (on the rail) and response point 2 (on the deck directly under the rail) as shown in Figure 4.3. The frequency response functions (FRFs) for the four mentioned cases are compared and the effects of the soil to the dynamic behaviour of the structure is illustrated.

The results are presented in Figure 4.4. It can be seen that introducing soil body instead of fixed supports, greatly reduces the first eigenfrequency, as well as changes the shape of the first eigenmode. It can be seen that the width of the peaks increases, while magnitudes decrease. This is caused by more inertia and damping, which are introduced to the system in Cases 1, 2, 3. This illustrates that the soil changes the dynamic structural behaviour of the system completely. The lower values of the first eigenfrequency makes the critical speeds, of the travelling vehicle, easier to achieve.

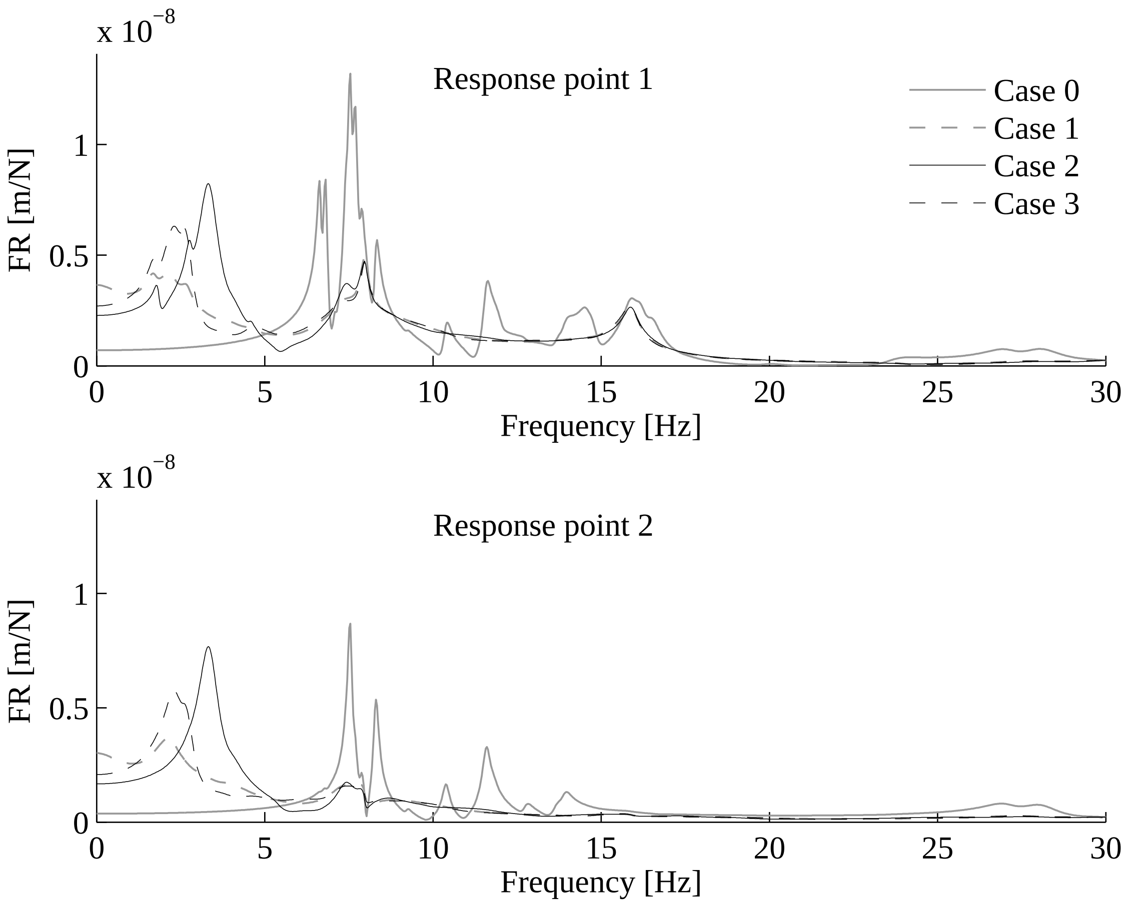

Figure 4.4: FRFs for four different soil stratifications: Response at Response point 1 (top) and Response point 2 (bottom)

4.4 Effects of including the vehicle in the model

The effects of the vehicle to the dynamic behaviour of the structure are analysed. The results are compared between a model that includes the MDOF vehicle model together with track unevenness and a model where the vehicle is introduced just as constant moving forces. The results are investigated for three different speeds for soil stratification Case 1.

In Figure 4.5 it is seen that for the MDOF vehicle model with increasing speed, the high-frequency vibrations become more pronounced. On the other hand, the constant force model underestimates these vibrations. The difference between these two models increases with increasing speed. With the analysed underlying soil case, the inertia and damping added to the system, reduces the high–frequency vibrations, but calculations done for stiffer soil cases show that with increasing stiffness of the soil high–frequency vibrations increase. Therefore, proper vehicle model is an important aspect for modelling the dynamic behaviour of the whole system.

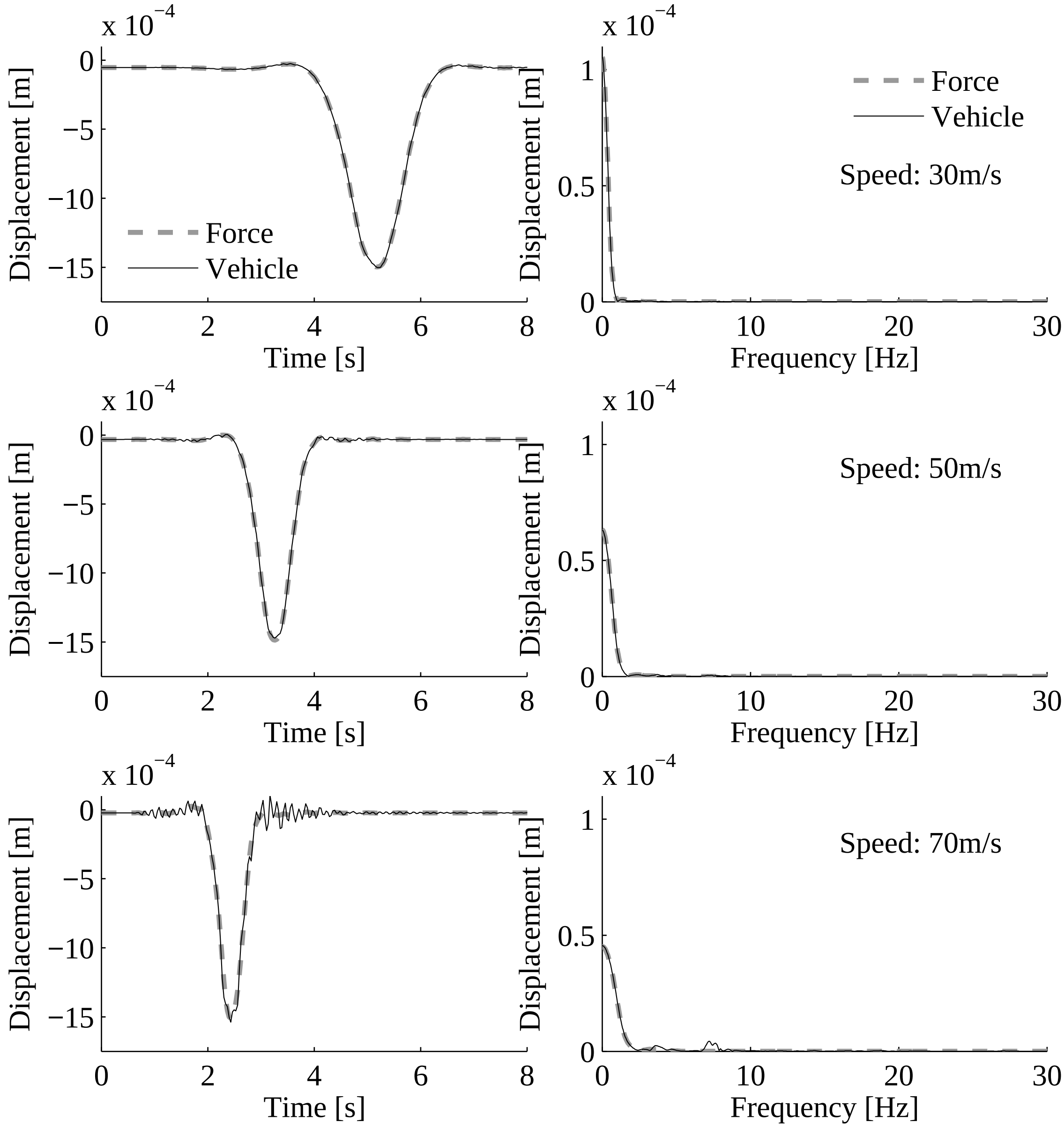

Figure 4.5: Time (left) and frequencies (right) series of the displacements of the model excited by a passing vehicle for the soil stratification Case 1

4.5 Structure–soil and structure–soil–structure interaction

Due to limited time some results are not presented in the paper in Appendix A, thus analysis of the coupling between structure and soil is presented here. In previously described computational model that includes the soil body, the structure–soil–structure interaction (SSSI) is taken into account. Thus, waves can travel through soil from one foundation to the others, affecting their behaviour.

This effect can be observed in Figure 4.6 where the the maximum displacement of a footing for different vehicle speeds is investigated. A more detailed description is given in Appendix A. It can be seen that for Case 1 (half-space of clay) the maximum displacements are obtained around the speed 56m/s, which is Rayleigh wave speed in clay. While the other two cases of soil do not indicate any significant SSSI.

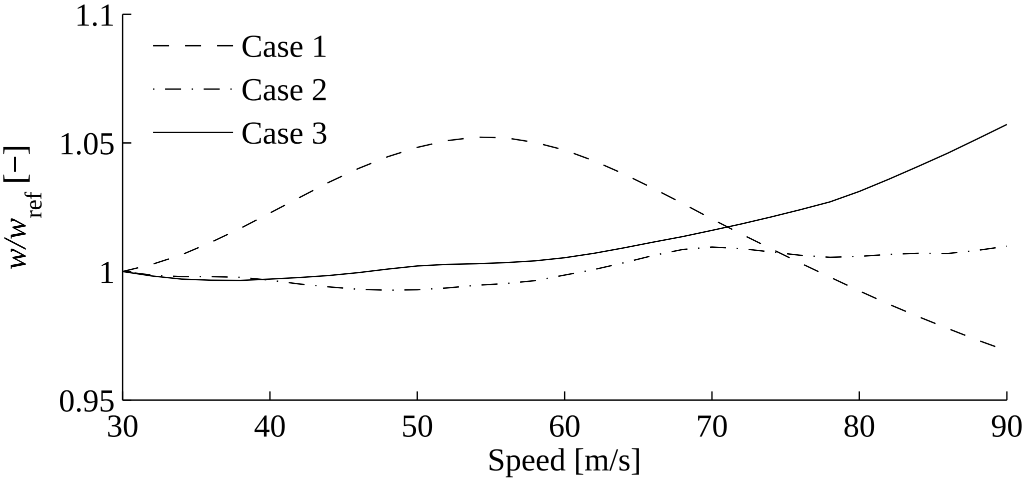

Figure 4.6: Maximum displacement dependency on speed, SSSI

Another way of modelling the soil is by including just structure–soil interaction (SSI). In this way, the effects from one footing displacement are not coupled with other footings. The advantage of modelling just SSI, is reduced computational time, as the impedance matrix only needs to be found for one footing and then be applied to all others, if all the footings have the same shape. Once again the effects of different speeds are investigated using this model, the results are presented in Figure 4.7. It can be seen that the critical speed seen for Case 1 disappears, while the behaviour for other cases stays very similar.

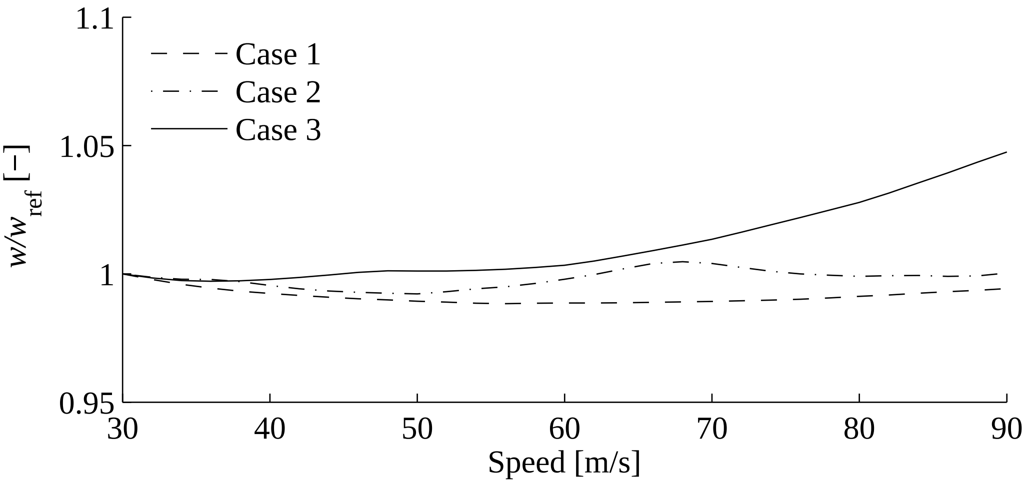

Figure 4.7: Maximum displacement dependency on speed, SSI

It can be concluded that SSSI can be a factor in the overall structure behaviour, but it is limited to homogeneous half-space for soil body, and even then the effects are not high. For layered half-space the SSI should be sufficient to obtain reliable results, at least for the investigated cases.

Chapter 5
Experimental tests on a small-scale model

In this chapter, experimental testing of a small-scale bridge model is presented. The tests are performed in order to validate the computational model, described in previous chapter. A detailed description of the experiment is in “Experimental validation of a numerical model for three-dimensional railway bridge analysis by comparison with a small–scale model” given in Appendix B. Here only a short introduction with some results is presented. Firstly, a brief description of the experimental model is given in Section 5.1. Later in Section 5.2 the computational model is presented. Measuring equipment and cases for tests are described in Section 5.3. Finally, validation of the computational model is given in Section 5.4 and results obtained from both models are compared in Section 5.5.

5.1 Overall description of experimental small–scale model

A dynamic analysis is performed of a multi-span bridge structure placed on subsoil, thus imitating structure–soil–structure interaction, as shown in Figure 5.1. The bridge model consists of deck, columns and footings which are screwed together, therefore creating stiff joints.

Figure 5.1: Experimental small–scale model

The previously listed parts are made of Plexiglas. A railway track is made of separate LEGO® railway pieces which are interlocked between each other and bolted to the bridge deck. To recreate a realistic structural behaviour, a LEGO® vehicle, powered by electric motor, with four wheel sets is used to traverse the bridge. The whole structure is placed on a subsoil which is substituted by mattress foam material. To fix the boundaries the mattress is placed within a box of plywood. At either end of the bridge, ramps are built of concrete tiles to provide space for acceleration and deceleration tracks. Also the bridge ends are fixed using ramps as supports and additional weights to imitate clamps. At the end of the track a break is employed to stop a vehicle completely. More detailed description of the whole model and construction considerations of particular parts of the model are given in Appendix B.

5.2 Description of computational model

The computational model described in this section is based on the main computational model presented in Section 4.2, including few modifications.
The bridge structure is based on finite element analysis, while the subsoil is implemented by using a semi-analytical approach in the computational model. To model the bridge deck and columns three-dimensional beam elements are used. These elements have two nodes and six degrees of freedom at each node, three rotational and three translational. Bending of the element is describe by equation of motion based on Bernoulli-Euler beam theory, while torsion is considered as Saint-Venant torsion. The computational model accounts for added masses, such as accelerometers, wires, etc. Also elements with higher stiffness are introduced to properly recreate bolted railway track sections. Governing equations of motion, illustration of a 3-D beam element and exact properties used in the computational model are given in Appendix B.
The vehicle is modelled as a two-dimensional 10-degrees-of-freedom system with two layers of suspension implemented as spring–dashpot systems. The vertical dynamic interaction between wheel and rail is implemented as a non-linear Hertzian force. Also track irregularities, i.e. railway track joints in the experimental model, are accounted for in the computational by introducing periodically repeating bumps. The governing equations for vehicle, interaction forces and track irregularities, as well as parameters for the listed computational model parts are given in Appendix B.
To model the underlying soil the semi-analytical approach is employed, which utilizes the Green's function in frequency and wave-number domain. The solution is valid for homogeneous viscoelastic material with horizontal boundaries between layers. The structure-soil-structure interaction is implied by coupling bridge structure with the underlying soil through rigid footings simply placed on the subsoil. Therefore a complex dynamic stiffness matrix for the footings and an impedance matrix for the subsoil are computed, first individually and then added together. More detailed explanation of structure–soil–structure interaction can be found in Appendix B.

5.3 Testing cases and measuring equipment

Two different types of tests are performed to investigate dynamic behaviour of the structure. Firstly, tests by applying impulse forces to obtain frequency response functions are performed to validate the computational model. The impulse forces are induced by hitting the structure with an impact hammer at excitation points as shown in Figure 5.2.

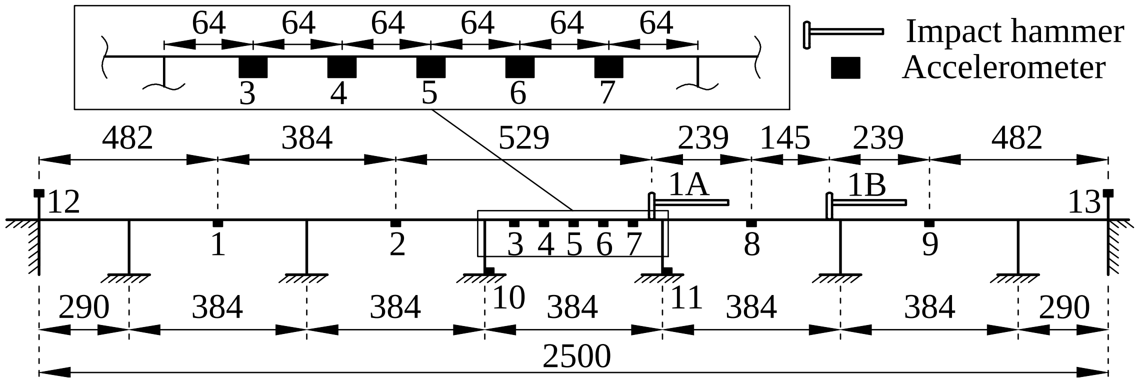

Figure 5.2: Accelerometers placing on the structure and excitation points (1 A and 1 B). Measures in milimeters

Later, tests using a traversing vehicle are done to analyse model response in frequency domain. These tests are performed with three different vehicle speeds: 0.53m/s, 0.97m/s and 1.31m/s. All experimental tests are done for five different cases:

- Case A: The bridge model is fixed on a solid surface (the laboratory floor) and no rail is present (this case is investigated just for tests with an impulse force),
- Case B: The bridge model is fixed on a solid surface (the laboratory floor) and the rail is bolted to the bridge deck,
- Case C: The whole structure is placed on one layer of dry mattress foam,
- Case D: The structure is placed on two layers of dry mattress foam,
- Case E: The structure is placed on one layer of soaked mattress foam.

More information about testing procedure itself and exact subsoil parameters used in the computational model, obtained after validation, are given in Appendix B. The Case E is not included in the paper due to limited time, thus the calibrated soaked mattress foam parameters are given: Young's modulus $E = 79000\text{N/m}^2$, shear modulus $G = 27200\text{N/m}^2$, mass density $\rho = 650\text{kg/m}$ and Poisson's ratio $\nu = 0.45$.

The equipment used for testing the small-scale model was manufactured by Brüel & Kjær, the following equipment is used:

- 1× Pulse front-end, type 3560 D,
- 1× Pulse front-end power supply,
- 1× PC with Pulse LabShop Fast Track Version 18.1.1.9.,
- 1× Ethernet crossover (LAN cable to connect front-end with PC),
- 1× Pulse dongle (USB flash drive with boot-able Pulse LabShop software license),
- 1× NEXUS conditioning amplifier, type 2692-C,
- 13× accelerometers, type 4507 Bx,

- 1× impact hammer, type 8202 (used just for tests with impulse force to obtain FRF).

A detailed description of the measuring equipment set-up with a sketch and information about tools listed above can be found in Appendix B.

5.4 Computational model validation

In this section, the results obtained from experimental and computational models, using an impulse force, are presented and compared between each other. Frequency response functions are given in Figure 5.3 and Figure 5.4, They are obtained at positions of accelerometers 5 and 7, as shown in Figure 5.2.

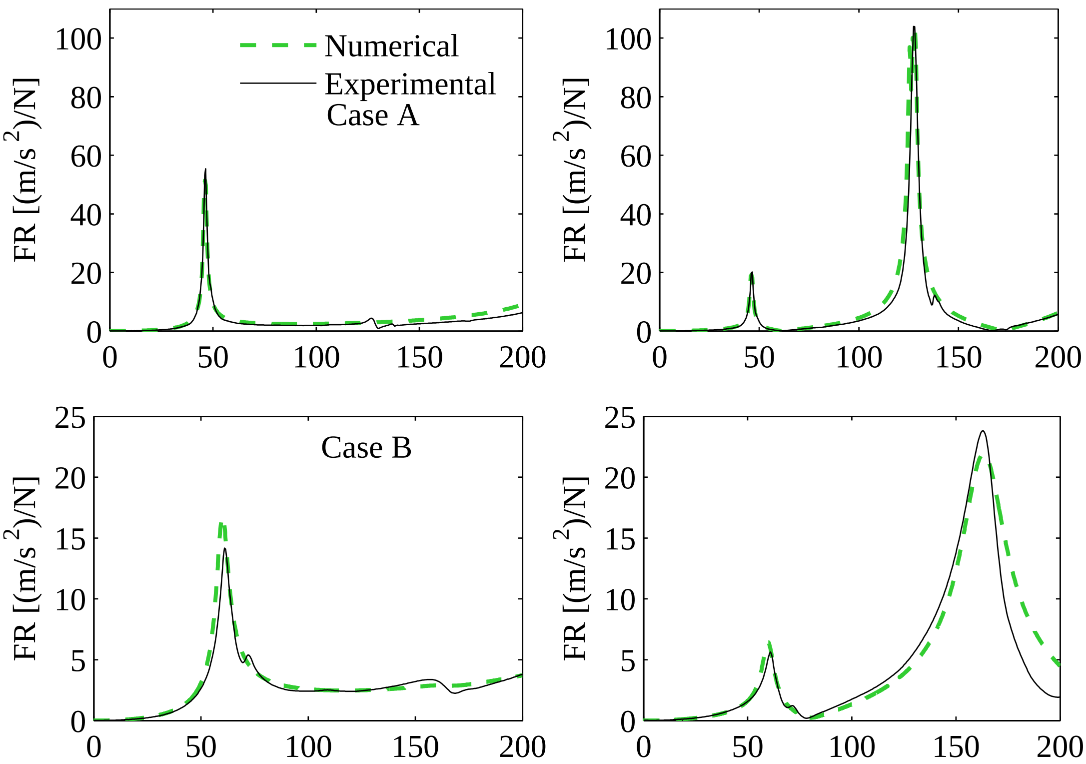

Figure 5.3: FRF comparison between experimental and numerical models for Case A (bridge without railway) and Case B (bridge with railway). Graphs on the left present data from accelerometer 5, while graphs on the right are from accelerometer 7

In Figure 5.3 can be seen that results obtained from experimental and computational models follow the same path and match quite well. When subsoil, i.e. mattress foam, is introduced, for Cases C, D and E, results start to differ, cf. Figure 5.4, but still show that computational model is able to predict real structure behaviour fairly well. The difference can appear because of boundaries which are present in the experimental model but not in the computational simulation. The main focus lies on first eigenfrequency since validation of the computational model is done according to it. In Figure 5.3 it can be seen that the highest value, of 61Hz, for the first eigenfrequency is obtained in Case B and a bit lower value, 46Hz, in Case A, thus telling that structural stiffness is increased by bolting the track to the bridge. Figure 5.4 shows the first eigenfrequency at 24Hz, 22Hz and 19Hz for Case C, Case D and Case E, respectively. According Figure 5.4 it can be seen that the overall system stiffness is decreased significantly by placing the structure on mattress foam, in this way enabling the structure movement downwards. It can be seen that the magnitude of the peaks decreases, this is due to lower eigenfrequencies. For soaked foam (Case E) the added mass increases the inertia in the system, thus reducing the magnitude of the peaks as well.

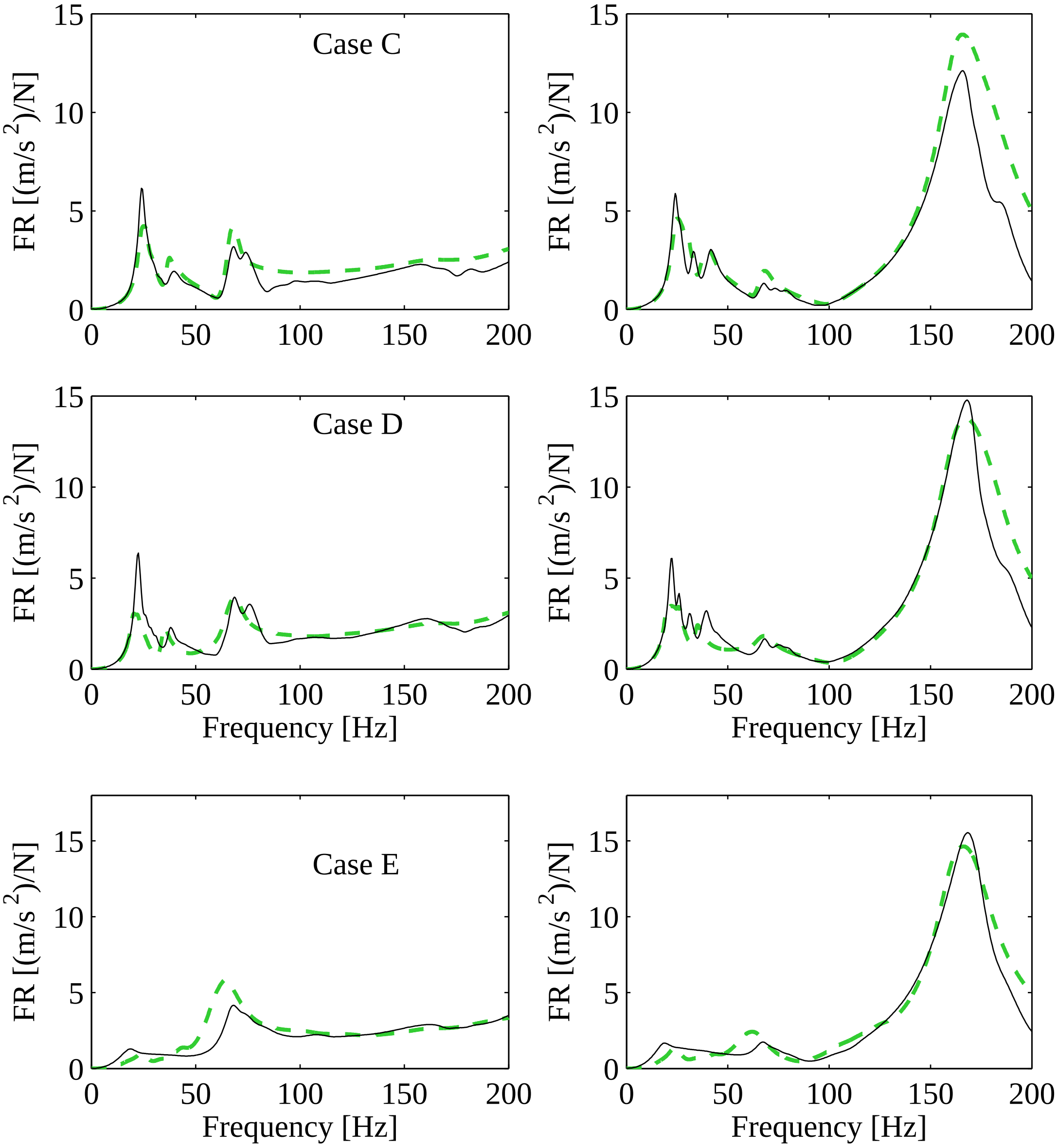

Figure 5.4: FRF comparison between experimental and numerical models for Case C (bridge on one layer of foam), Case D (bridge on two layers of foam) and Case E (bridge on one layer of soaked foam). Graphs on the left present data from accelerometer 5, while graphs on the right are from accelerometer 7

5.5 Results comparison

In this section, the results in frequency domain of the tests with a passing vehicle are presented for Cases B, C, D and E. Tests with a passing vehicle are not performed for Case A, since there is no railway track introduced and no vehicle can pass the bridge. The structural response is obtained from accelerometer 5, the position of which can be seen in Figure 5.2. The same speeds are analysed with calibrated computational models. The results are presented in Figure 5.5, Figure 5.6, Figure 5.7 and Figure 5.8 for Cases B, C, D and E, respectively. The methodology used for data analysis is explained in Appendix B.

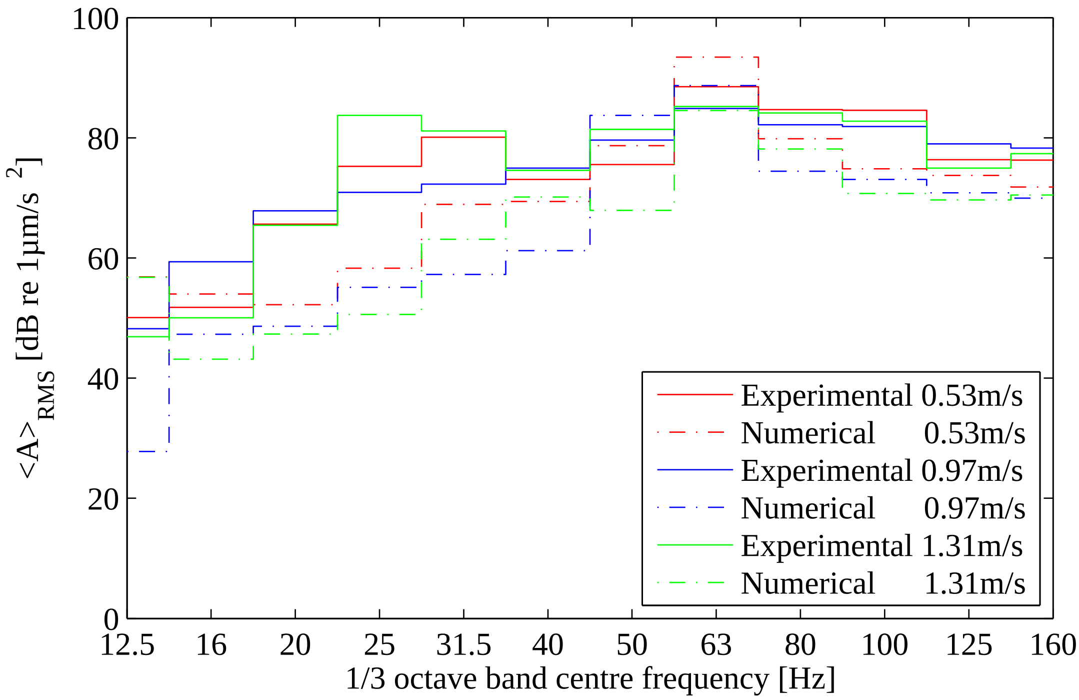

Figure 5.5: Accelerations in frequency domain; Case B (bridge with railway)

In Figure 5.5 it can be seen that the highest acceleration occurs in the 63Hz 1/3 octave band, thus the value is considered as the first eigenfrequency for Case B. Figure 5.6, Figure 5.7 and Figure 5.8 show that accelerations peak in the 80Hz 1/3 octave band for Cases C, D and E. The structural response for Case E, when the subsoil is substituted by soaked mattress foam, is more consistent than for Case C or Case D, using dry foam. It might be because of increased density of foam which introduced more inertia in the system and provided more linear response.
The results for all four cases show the same trend, lower accelerations at low-frequency and higher accelerations at high-frequency. Also acceleration response for a passing vehicle is constantly underestimated in computational model, however the results from both, computational as well as experimental model, follow the same path. Moreover, computed response from the computational model match better with experimental data at high-frequency. All these differences may arise from different implementation of the vehicle and the track in the computational and experimental models. It might be that the vehicle and the track in the computational model

do not recreate all the effects caused by the LEGO® vehicle on the real small-scale structure.

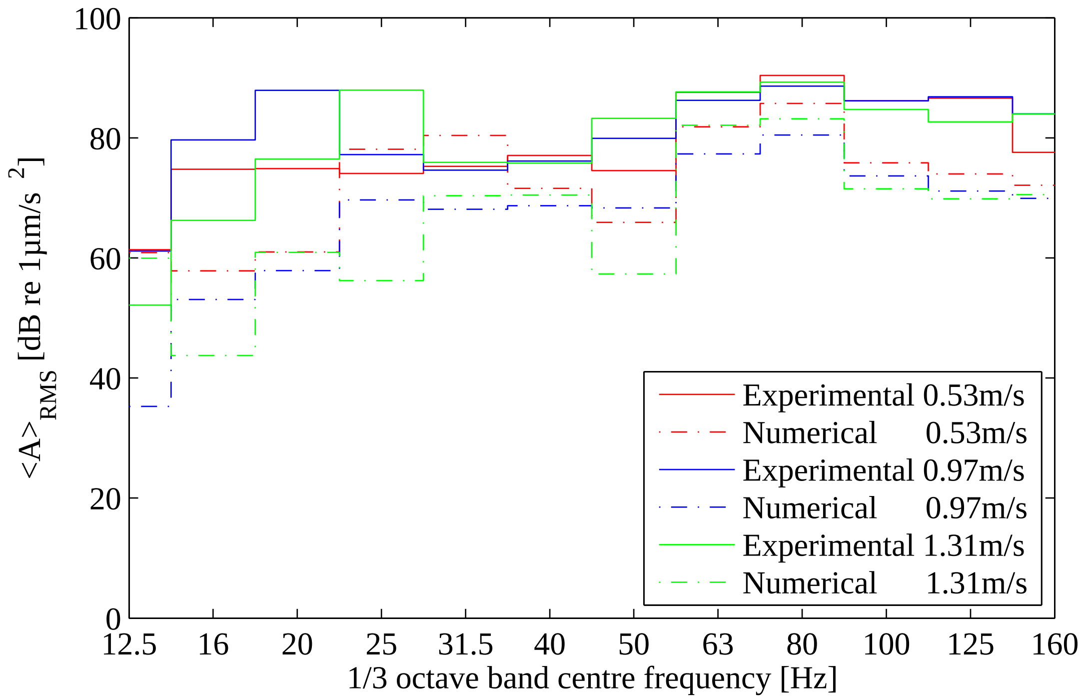

Figure 5.6: Accelerations in frequency domain; Case C (bridge with railway on one layer of dry foam)

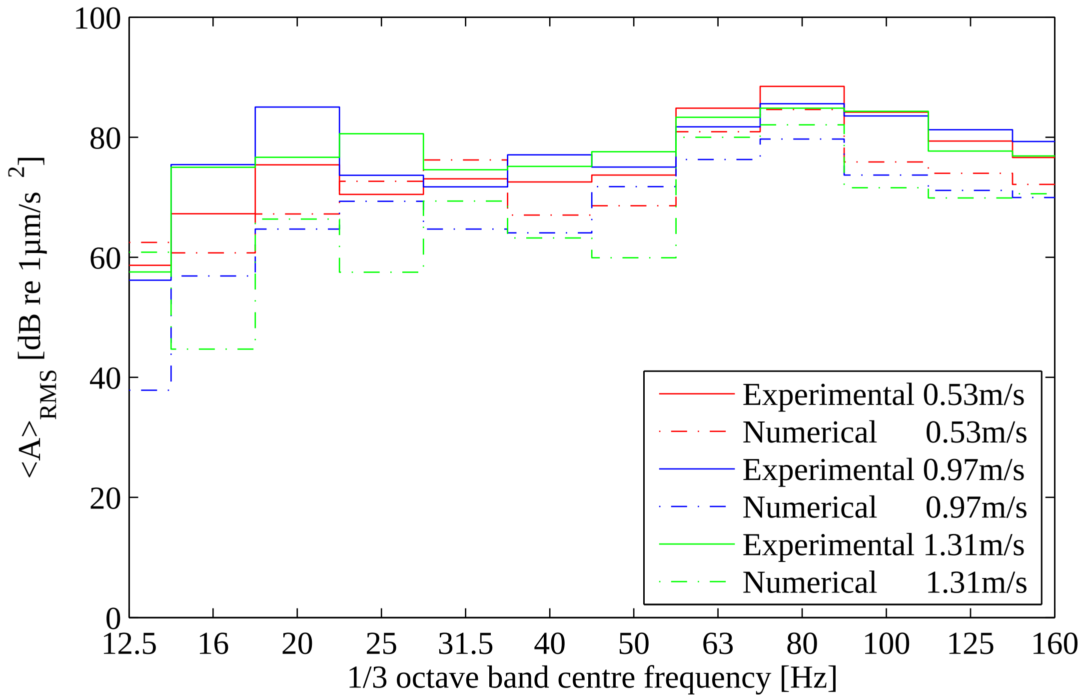

Figure 5.7: Accelerations in frequency domain; Case D (bridge with railway on two layers of dry foam)

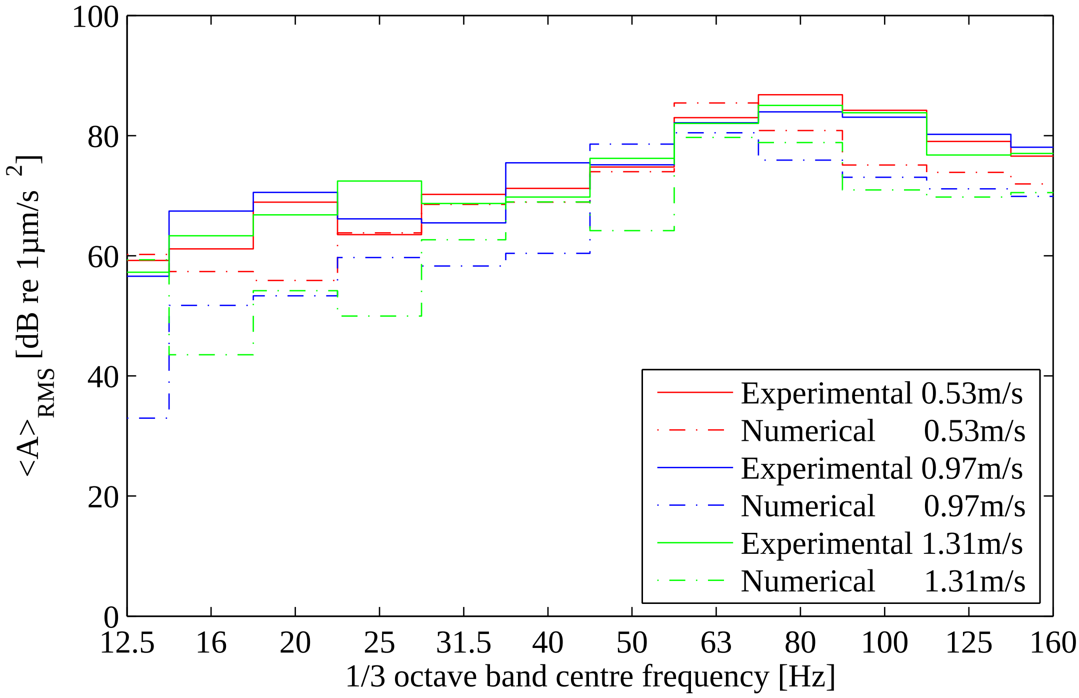

Figure 5.8: Accelerations in frequency domain; Case E (bridge with railway on one layer of soaked foam)

Chapter 6

Conclusions and discussion

In this chapter, the conclusions for the overall work done for the thesis, including the papers "Numerical modelling of dynamic response of high-speed railway bridges considering vehicle–structure and structure–soil–structure interaction" and "Experimental validation of a numerical model for three-dimensional railway bridge analysis by comparison with a small–scale model", are presented. The dynamic behaviour of a railway bridge structure excited by a high-speed train was studied. The effects from a number of different phenomena were investigated.

At the beginning the most simple cases were analysed, where the bridge was modelled as a 2-D simply supported beam and the vehicle as a moving constant force. It was done using both analytical and FEM based approaches. Thus, the FEM computational model was validated. Further, more advanced vehicle models were implemented, that are able to recreate the dynamic effects from the moving locomotive better. Finally, the MDOF vehicle model was chosen for further analysis, as it is able to include the effects from uneven track profile and thus, a non-linear wheel–rail interaction.

Further, a 3-D computational model was introduced, to better represent the analysed structure. A computational model for a multi-span bridge with seven pylons, placed on surface footings was created. The created model includes non-linear wheel–rail interaction, as well as structure–soil–structure interaction. It is determined that track irregularities have a significant effect on the structure behaviour, especially with increasing vehicle speeds. At a vehicle speed 70m/s (250km/h) this effect becomes the governing factor in the structural behaviour, if the underlying soil is stiff. Further, the effects from the underlying soil properties were analysed. Introducing the soil, instead of fixed supports, changes the behaviour of the system drastically: the first eigenfrequencies are reduced and the eigenmodes change.

Small–scale laboratory tests were performed, to validate the mentioned computational model. Experimental model of a multi-span bridge, with surface footings was constructed. The effects from a passing locomotive were reproduced by a small–scale vehicle, travelling on a plastic railway track. Soil was substituted by mattress foam, which was later soaked to reduce the wave travelling speed in the material. The compared FRFs show good agreement between numerical and experimental models, while the vehicle induced deck accelerations are underestimated in the computational model. A better defined experimental vehicle model would help to reduce the differences.

The work presented in this thesis offers an approach to model a complicated system involving a number of different phenomena, the results show a reasonably good agreement between experiments and calculations. Further, work could reduce the number of approximations used in the computational model, also more experiments could be carried out for a better calibration of the vehicle model.